Computational Study of Cellular Actin-Myosin Interactions Using Agent-based Models

SHIHANG DING

MARCH 2025

Computational Study of Cellular Actin-Myosin Interactions Using Agent-based Models

a dissertation submitted

to

The Graduate School of Engineering Science

Osaka University

in partial fulfillment of the requirements

for the degree of

Doctor of Philosophy

in

Engineering

by

Shihang Ding

March 2025

Abstract

Actin-myosin interactions play central roles in cellular force generation, which is intimately associated with multiple cell processes, including cell migration, morphogenesis, and cytokinesis. It has been widely reported that the conventional myosin II monomers can form thick filaments to achieve sustained force generation. However, this thick filament structure varies substantially depending on myosin isoforms and other conditions including ionic concentration and the pH value. The influence of thick filament structures on generating contractile force is still elusive. Meanwhile, unlike the striated muscle cells, myosin thick filaments in smooth muscle and non-muscle cells are more randomly distributed and their contributions to the cell mechanical adaptation still require a compelling explanation. In this study, an agent-based computational model, incorporating cytoskeletal elements is invoked to investigate the impacts of actin-myosin interactions on cellular force generation systematically and quantitatively. We first applied it to a general disorganized actomyosin structure and determined that the density of thick filaments and their spatial distribution have an inextricable influence on the contractile force. Additionally, we demonstrated that the increase of the total myosin monomers in a thick filament and the existence of a central bare zone are indispensable for enhancing cell force generation. Furthermore, our simulation has revealed that actin-myosin interactions are the linchpin of cell mechanical adaptation, which is consistent with our pre-conducted in vitro stretch experiment of the ventral stress fiber. The buckling of the actomyosin bundle after compression is mainly related to the unbinding events of myosin and ACPs. The following recovery can be ascribed to the actin-rebinding of myosin and its walking rate along the filamentous actin. Strikingly, the initial mechanical properties of actomyosin bundles such as the bending stiffness of F-actin and the bundle thickness cannot alter this mechanical adaptation significantly. Based on these findings, our study can provide insights into a comprehensive understanding of how myosin thick filament structure and its dynamic interactions with actin contribute to cell force generation and its mechanical adaptation.

Contents

Listing of figures

This thesis is dedicated to everyone and everything I have encountered and experienced.

Rigid,

the skeleton of habit alone

upholds the human frame.

Virginia Woolf, *Mrs. Dalloway*

1

Introduction

Actin-myosin interactions play essential roles in multiple cell processes. However, their underlying mechanism varies depending on the protein isoforms and the cell types. In this section, a systematic introduction was summarized from the molecular properties of myosin and its signaling pathways for the mechanochemical interactions with actin to their structural association that facilitating the capacity of mechanical adaptation. Three types of cell, including the striated muscle, the

smooth muscle, and the non-muscle cells, were incorporated. And the current knowledge of the major muscle modeling methods for the force generation was investigated as well, together with a review for the merits and demerits of each of them.

1.1 Myosin superfamily and its structural properties

As the widely known motor protein, isoforms of myosin have formed a superfamily and have been investigated for decades [163]. Depending on the molecular structures and cell types, myosin isoforms function as a force generator, mechanical sensor, and cargo transporter. More than thirty-five isoforms have been reported in nature, and they are indispensable for a myriad of cellular processes, including cytokinesis, migration, vesicle transport, and morphogenesis [98]. Although there are several distinctions among myosin isoforms (Fig. 1.1), their molecular structures can be described in a general form (Fig. 1.2). They all start with a motor domain, in which one or two myosin heads are involved [117]. This motor domain provides binding sites for the actin, ATP, and its hydrolysis products. The N-terminal domains of myosin heavy chains (MHCs) are the origin of these motor heads. In most myosin isoforms, they are composed of the two helically constructed MHCs. A neck region or the level arm part follows the motor domain. It mainly consists of the repeating IQ patterns whose number is dependent on the isoforms. This neck region plays essential roles in myosin activation and conformational change. It contains the associating spots for myosin light chains (MLCs) and other proteins including the calmodulin [20]. The following part is the coiled-coil tail region dimerized from MHCs. This tail domain is critical for interacting with other myosin monomers so that a thick filament can be formed for the conventional myosin II isoforms. For several isoforms including myosin V, a cargo-binding domain connects to the end of the tail domain and is the most C-terminal part of the molecule [190]. It will associate with targets including vesicles for the intracellular transportation. In this study, we mainly focus on the molecular basis for the force generation in cells, which is highly related to the tra-

ditional myosin II isoform. Therefore, without specification, the following discussions are typically associated with myosin II monomers.

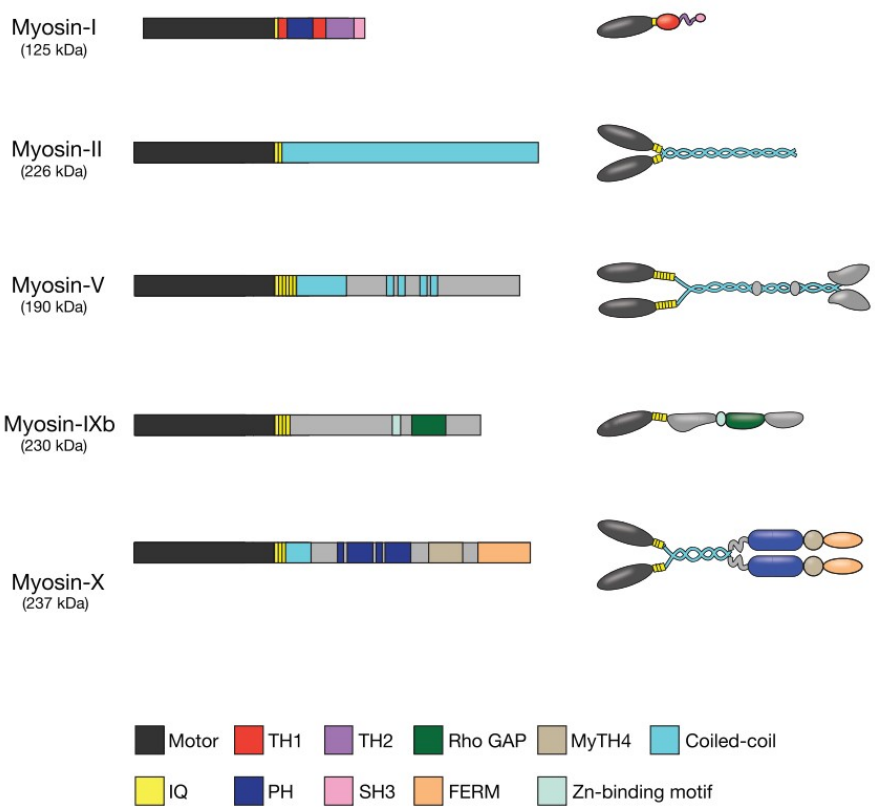

Figure 1.1: Myosin isoforms. Multiple myosin isoforms exist in nature. The number of motor heads varies depending on the isoform. For instance, Myosin I and Myosin IXb incorporate only one head, while Myosin II, Myosin V, and Myosin X include two motor heads per monomer. Isoforms like Myosin II, V, and X can include a coiled-coil motif or protein interaction motif in their tail domain to promote dimerization, membrane-binding, or cargo-binding ability[6].

1.2 Myosin signaling pathway for the activation

Myosin generates mechanical forces with actin filaments by consuming the chemical energy from the ATP hydrolysis[25]. This is the common method that exists in a wide range of cell types, especially muscle cells. However, the signaling pathway for myosin activation varies highly depending on the cell

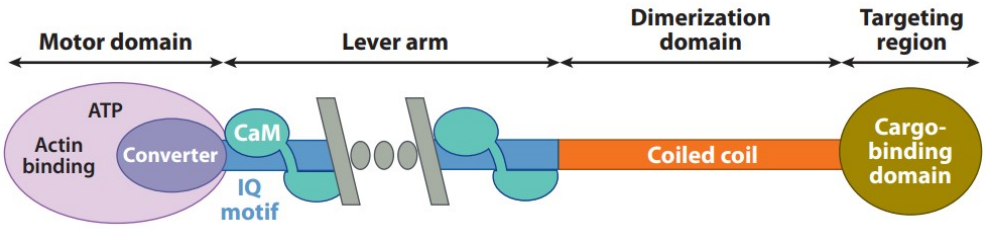

Figure 1.2: Myosin structure. A general structure of myosin molecule can be categorized into a motor domain, a lever arm, a dimerization domain, and a targeting region. Components in the motor domain are able to associate with ATP and actin monomers. The converter plays an important role in amplifying its conformational alteration and propagating it to the adjacent lever arm domain. This level arm part is composed of multiple IQ motifs in a helical manner, allowing the association of different proteins including calmodulin (CaM) and specialized light chains. The following dimerization domain can include a coiled-coil tail facilitating the protein interactions. At the most C-terminal regions can function as a cargo-binding domain. The structure of the dimerization domain and the targeting region are highly variable depending on the myosin isoforms [163].

types [89]. It is a complicated process including multiple electrochemical transitions from the tissular level to the molecular level. In this section, we summarize the current knowledge of myosin activation in striated muscle, smooth muscle, and non-muscle cells.

1.2.1 Myosin activation in striated muscles

Striated muscles, including the skeletal and cardiac muscles, are composed of multiple muscle fibers parallel to each other [41]. In each muscle fiber, myofibrils including myosin and other proteins are covered by the sarcolemma, a membrane-like structure that ensures the contraction directions of myofibrils are maintained identically. This sarcolemma is also in charge of the formation of neuromuscular junctions via the widely distributed neurotransmitter receptors on its motor end-plate area [77,89]. When motor neurons branch into multiple presynaptic terminals and close to this motor end-plate area, they will combine with the neurotransmitter receptors consequently. Once the somatic nervous system generates the neural impulse, this electric signal will propagate on the aforementioned pathway and will turn on the voltage-gated calcium channels on each synapse. A subsequent influx of calcium ions will be triggered and lead to the release of acetylcholine (ACh), a typical neurotransmitter [105].

On the sarcolemma, nicotinic acetylcholine receptors (nAChRs) bind to ACh upon its diffusion across the synaptic cleft[75]. This interaction mechanically opens the sodium channel, a ligand-gated ionotropic receptor, as it is directly coupled to the activated nAChRs. Consequently, the influx of sodium ions induces depolarization of sarcolemma and initiates an action potential[8]. Then, the generated action potential propagates along the membrane until it reaches the transverse tubules, specialized invaginations of the sarcolemma enriched with ion channels. Within these transverse tubules, L-type calcium channels, critical for excitation-contraction coupling in skeletal muscle, are activated by the action potential[89]. The conformational changes of these channels mechanically stimulate the ryanodine receptors (RyRs) located on the sarcoplasmic reticulum (SR). It should be noticed that RyRs exist in three isoforms—RyR1, RyR2, and RyR3—each associated with calcium release in specific cell types[38,49,189]. In skeletal muscle, RyR1 is the predominant isoform and is directly coupled to the L-type calcium channels. Upon activation, RyR1 facilitates the release of calcium from the SR, leading to an increase in cytosolic calcium concentration. This process, known as depolarization-induced calcium release (DICR), is central to myosin activation (Figs. 1.3 and 1.4).

As the cytosolic calcium concentration increases, the released calcium ions bind to troponin C (TnC), a calcium-binding subunit of the troponin complex, an integral component of the actin filament in striated muscles[45]. Besides the TnC, the complex comprises another two subunits, including troponin I (TnI) and troponin T (TnT). Considering their individual function, TnC serves as the calcium sensor, TnI inhibits actomyosin interactions under resting conditions, and TnT anchors the complex to the tropomyosin. Calcium binding to TnC induces a conformational change in the entire complex. This structural rearrangement displaces the tropomyosin, a regulatory protein, into the groove of the helical F-actin filament and uncovers the myosin binding spots along the actin filament[45,176]. As a result, the myosin-binding sites are exposed. This exposure enables subsequent interaction, facilitating the cyclical attachment, power stroke, and detachment of myosin heads. These events drive the sliding of myosin toward the barbed ends of actin filaments, generating the force neces-

sary for muscle contraction. It should be noticed that there are still several differences in the signaling between cardiac and skeletal muscles even though their basic mechanisms are similar. For example, the L-type calcium channels play more important roles in cardiac muscle cells, since the calcium influx via them can further trigger the calcium release from SR through the RyRs, which is known as the process named the calcium-induced calcium release (CICR)[89]. In addition, cardiac muscle can further regulate myosin activity through the phosphorylation of its regulatory light chains (RLCs), which mainly exist in smooth muscle and non-muscle cells and will be introduced in the following section. Such additional myosin regulation via RLCs in cardiac cells has been reported as a mechanism for enhancing the active force and improving its calcium sensitivity[69](Fig. 1.4).

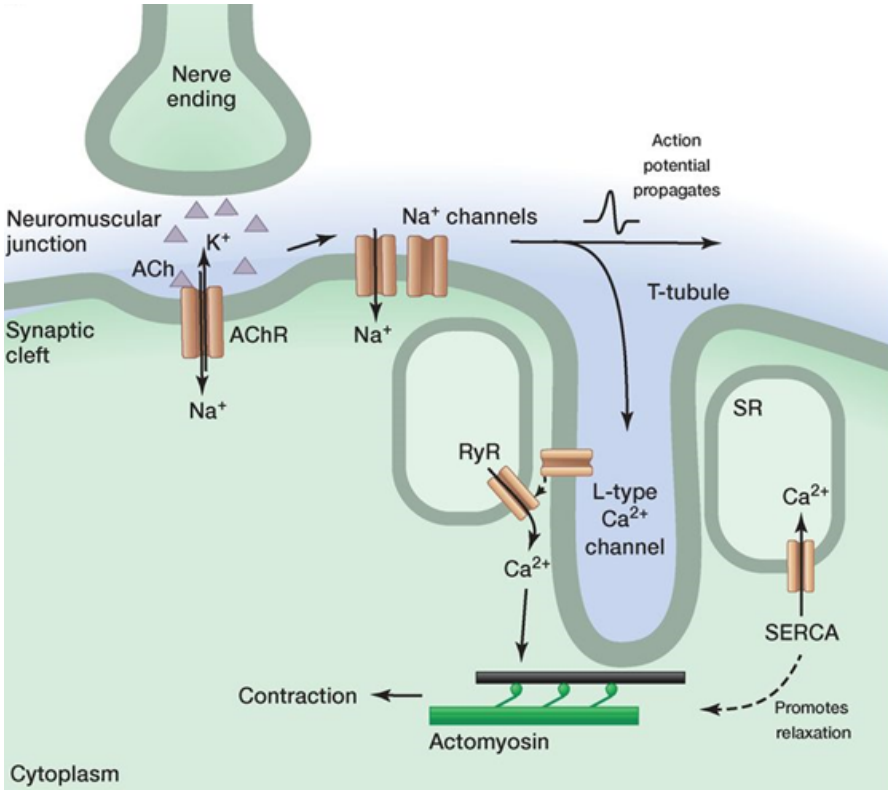

Figure 1.3: Myosin activation in striated muscles. The activation of striated muscle myosin II is a complicated process, including an electrochemical signaling transition between the neuron system and muscle cells, and the depolarization-induced calcium release (DICR)[89].

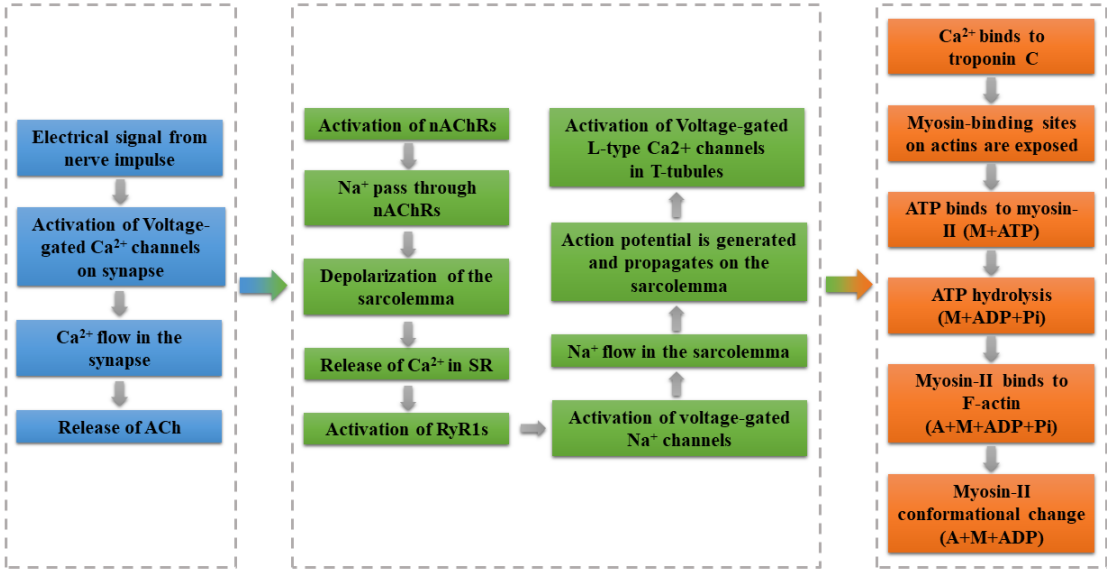

Figure 1.4: Summary of the myosin activation in striated muscles. Part in blue represents the electrochemical signaling; part in green denotes the process of DICR; part in orange indicates the force generation based on actin-myosin interactions [194].

1.2.2 Myosin activation in smooth muscle and non-muscle cells

Unlike striated muscles, smooth muscle and non-muscle cells do not contain the troponin complex. Instead, the activation of myosin heads primarily relies on the phosphorylation of their regulatory light chains (RLCs) [162,59]. Upon calcium influx, the calmodulin protein, which localizes on the myosin neck region, binds to calcium ions. This binding subsequently activates myosin light chain kinase (MLCK), an enzyme responsible for phosphorylating the RLCs. Phosphorylation triggers a conformational change in the myosin molecule, further increasing its ATPase activity. This MLCK-based regulation is the common mechanism underlying smooth muscle and non-muscle cell contraction, often referred to as calcium-calmodulin-dependent myosin light chain phosphorylation (Fig. 1.5). However, there are several differences between the two types of cells. For example, the MLCK isoforms in non-muscle cells are longer than those found in smooth muscle cells. Additionally, the phos-

phorylation rate of MLCK differs depending on the type of myosin. Studies have shown that MLCK phosphorylates smooth muscle myosin more quickly than non-muscle myosin, enabling the smooth muscle to contract rapidly in response to calcium influx [162].

Besides the MLCK, there is an additional protein called the Rho-associated protein kinase (ROCK) that can regulate the RLC phosphorylation and further facilitate myosin activation in smooth muscle and non-muscle cells [151,81,31]. Unlike the MLCK, ROCK triggers the actin-myosin interaction in a calcium-independent manner (Fig. 1.5). It is highly related to a small GTPase called RhoA, which can bind to GTP and initiate the ROCK. As a result, the activated ROCK can inhibit the myosin light chain phosphatase (MLCP), which can dephosphorylate the RLCs. Although it is not the predominant pathway, ROCK has been reported for its ability to phosphorylate myosin RLCs at serine and threonine residues, directly contributing to myosin activation [151]. Similar to the MLCK mechanism in cardiac muscle, ROCK in smooth muscle cells can enhance calcium sensitization as well, particularly when the intracellular calcium concentration is decreasing. In the non-muscle cells, ROCK mainly contributes to the contraction of stress fibers. It has been demonstrated that the RLC phosphorylation presents a spatial-based preference for MLCK and ROCK. Several studies have determined that RLC phosphorylation relies more on ROCK at the cell center, whereas the MLCK plays a predominant role at the cell periphery[7,61,170]. However, these two mechanisms can occur simultaneously for initiating the actin-myosin interaction by MLCK and maintaining the cell contractility based on ROCK[25].

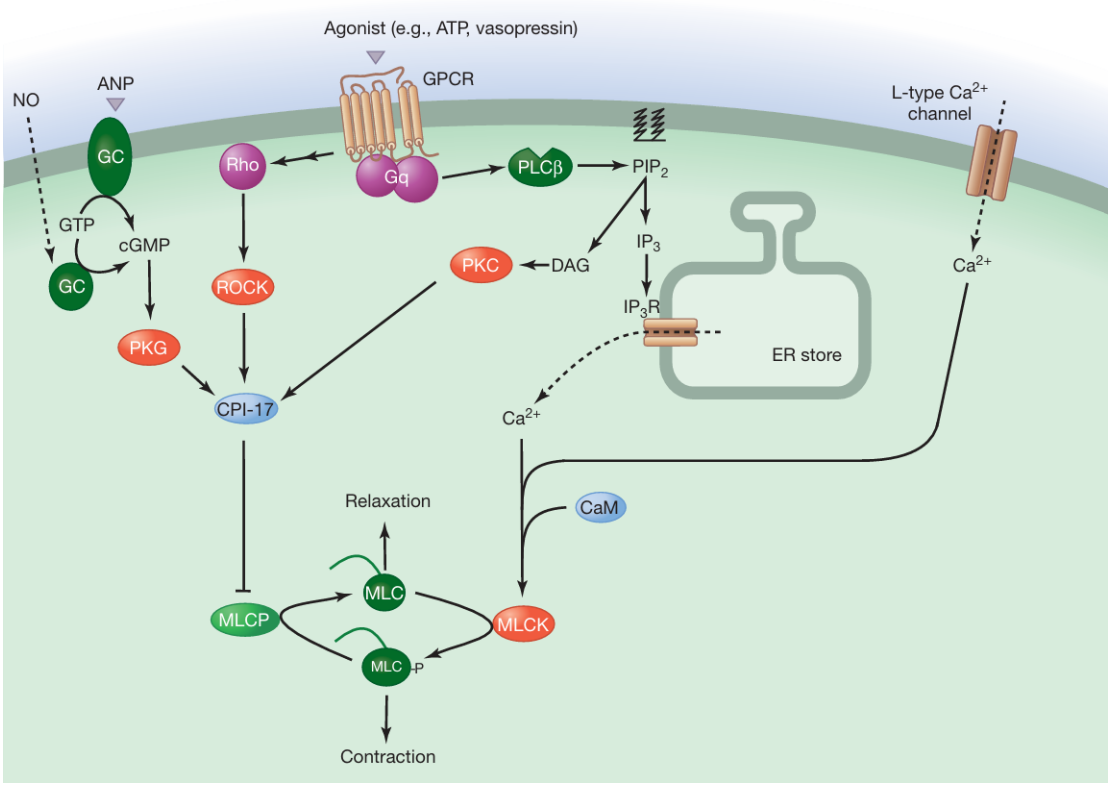

Figure 1.5: Myosin activation in smooth muscles. Myosin light chain (MLC) kinase can be triggered by the release of calcium ions from L-type calcium channels or IP3Rs. The phosphorylated MLC can facilitate the muscle contraction subsequently. The RhoA/ROCK pathway can contribute to calcium sensitization by shifting the phosphorylation state of the myosin light chain phosphatase (MLCP)[89].

1.3 Actin-Myosin interaction and myosin molecular dynamics

Although the signaling pathway for myosin activation varies depending on cell types, their mechanism for interacting with actin is conserved. An overview of the current knowledge of actin-myosin interaction is summarized in this section. In addition, experimental and theoretical explanations of myosin dynamics are included here as well.

1.3.1 Actin-myosin ATPase cycle

Based on the advancement of microscopy, the interaction process between myosin and actin has been investigated and described in detail[67,63]. After the displacement of tropomyosin, myosin II monomers can bind to F-actins by consuming ATP. The chemical energy from the ATP hydrolysis facilitates this myosin-binding event (Fig. 1.6). Meanwhile, its hydrolysis products, including the adenosine diphosphate (ADP) and phosphate (Pi), are associated with the motor head domain in myosin. This actin-myosin state is called the weakly bound state or the pre-powerstroke state since its labile connection is due to the higher thermal energy[163]. Following the weakly bound state, myosin will release the Pi and only the ADP remains on the myosin head. During this Pi release phase, a conformational change occurs in the neck region of myosin, altering the angle between the motor head and the following level arm[166] (Fig. 1.7). This structural shift is also the origin of force generation. Because it causes a relative displacement between actin and myosin, it can be considered muscle contraction from the macroscopic view, which is also the fundamental observation for supporting the sliding filament theory[141]. The ADP-associated myosin maintains this strongly bound ADP state until the subsequent ADP release leads to the strongly bound rigor state, which is the final actin-bound state of the actin-myosin ATPase cycle. It has been revealed that this ADP release process is highly force-dependent[163].

Therefore, the actomyosin machinery demonstrates significant mechanochemical features. Following this rigor state, a new ATP can attach to the myosin head again which results in the dissociation between actin and myosin. Due to this reattachment of ATP, a conformational change in the head domain is induced and alters its affinity for actin. Meanwhile, it is associated with a significant free energy change, making the reverse reaction (ATP unbinding from myosin without hydrolysis) highly unfavorable. Hence, the myosin unbinding event can be triggered, and it is an irreversible process. Following that, the unbound free myosin would be ready for another interaction cycle once the ATP hydrolysis occurs.

Together, this Actin-myosin ATPase cycle can be summarized and categorized into unbound, weakly bound, and strongly bound states. The ratio of the strongly bound time to the time consumption for one cycle is defined as the duty ratio of myosin. This interaction mechanism is highly conserved among myosin isoforms, however, the unbinding rates of Pi and ADP are distinct, which results in different transition rates for myosin isoforms. For example, the duty ratios of myosin V and VI are large enough for their heads to stay a relatively long time on F-actins [190,85]. During this period, another motor head in the myosin monomer can rebind on a new position on F-actin, which allows continuous walking along the thin filament [141]. This type of motor protein is termed the processive motor. On the other hand, the duty ratio for the conventional myosin II monomer is much lower than the processive ones. Therefore, these non-processive myosins usually form an ensemble to ensure continuous walking on F-actins [46]. It should be noticed that the two heads of non-processive myosin interact with actin independently according to the single-molecule experiments [173]. However, muscle stretching experiments have demonstrated a rapid attachment of the second motor in a myosin whose one head has already attached to actin [14]. Such force-induced fast attachment allows the two myosin heads can be considered as working simultaneously.

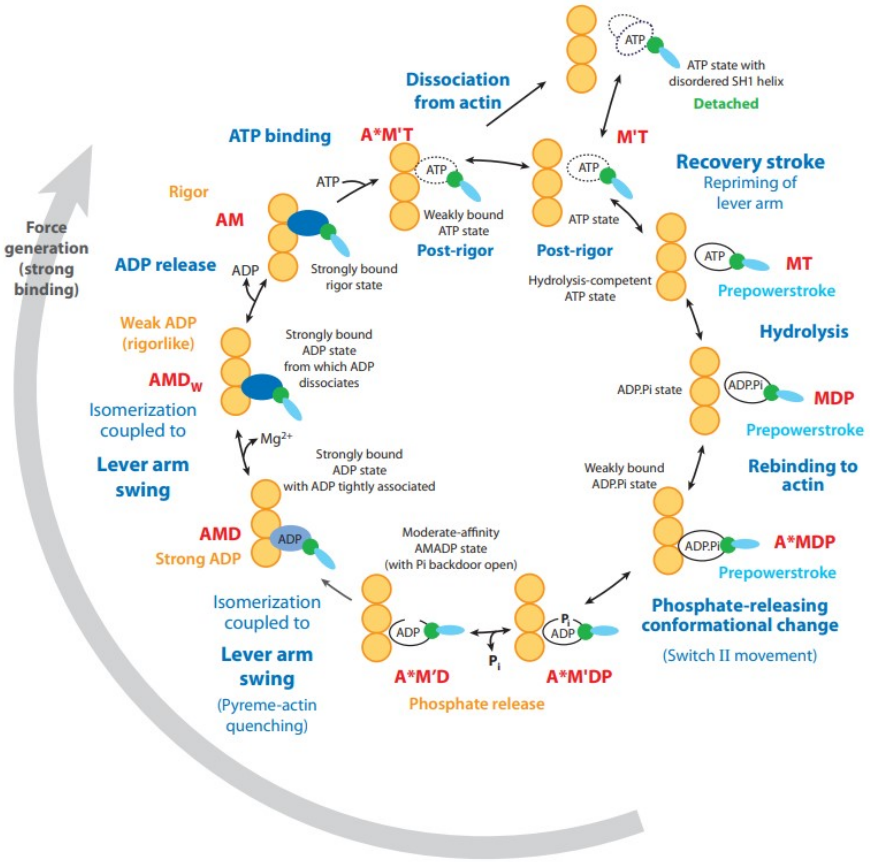

Figure 1.6: Actin-myosin ATPase cycle. The interactions between actin and myosin are the origin of force generation. Depending on the conditions, this interaction cycle can be categorized into three mechanochemical states including the unbound, weakly bound, and strongly bound states. The essence is the conformational change of the myosin level arm during the transition from the weakly bound to the strongly bound states. It is triggered by the phosphate release, one of the ATP hydrolysis products, thus bringing a displacement between actin and myosin. It should be noticed that the duty ratio or the lifetime of the myosin II monomer on actin is much shorter than processive myosin isoform like myosin V. Therefore, to achieve sustained force generation, myosin II usually forms a thick filament and works as an ensemble on F-actins [163].

1.3.2 Theoretical explanations for the level arm swinging

As mentioned earlier, the conformational change of the myosin neck region, particularly the swinging movement of the lever arm, is considered the essential origin of force generation (Fig. 1.7). However, the fundamental mechanism that could explain this structural alteration is still debatable. Currently, two major theories exist, corresponding to the power stroke and the Brownian ratchet mechanisms.

In the power stroke mechanism, a great downhill of the motor free energy resulted from the Pi release. Such energy is provided by the external source mainly the hydrolysis of ATP and stored as elastic energy in the motor[67,177]. The subsequent release of Pi is a local event that facilitates tension relaxation so that the relaxed motor can proceed with a following swinging. Although the molecular part in myosin monomer that can function as this elastic element is still elusive, this power stroke mechanism has been widely accepted and applied in a myriad of myosin modeling theories and explanations. However, single-molecule observations and theoretical predictions have demonstrated that the considerable strain for providing sufficient elastic energy of a level arm swinging is impractical due to the monomer size[111]. It implies that there should exist additional energy events for accomplishing the conformational change of the motor.

Another major theory, the Brownian ratchet mechanism, considers the myosin head continuously fluctuating forward and backward along the actin filament[177,179]. However, the potential distribution along the filament is periodically asymmetric and sawtooth-like because of the unidirectional arrangement of actin monomer, which is the origin of the filament polarities[29,114]. Subsequently, the external energy supplement (e.g. ATP hydrolysis) will improve the contained free energy in the motor head and a spatial bias downhill of it can be followed due to the asymmetric potential distribution. Therefore, the myosin movement on actin filament resembles a gear working on a ratchet which is unidirectional and irreversible.

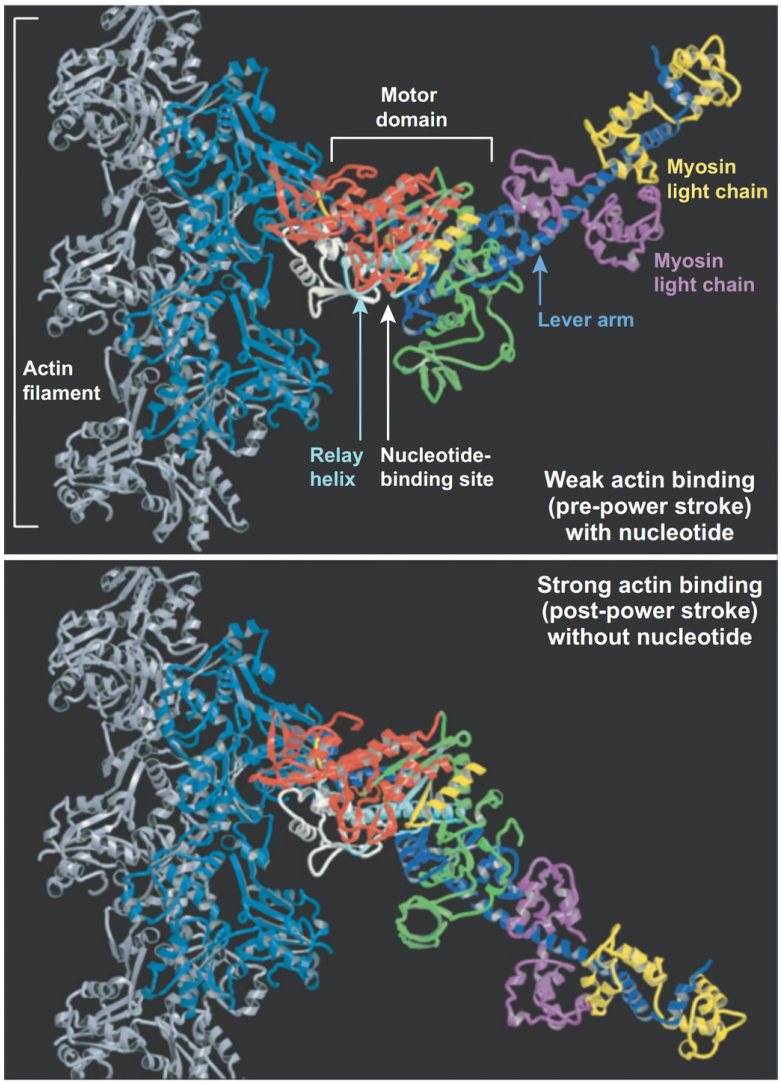

Figure 1.7: Swinging of the motor lever arm. The F-actin is shown on the left side. The myosin II motor domain is shown at the center binding to the F-actin. The connected myosin lever arm and its associated myosin light chains are presented on the right side. This swinging of the motor lever arm from the weakly bound (top) to the strongly bound (bottom) states is vital for generating the contractile forces [166].

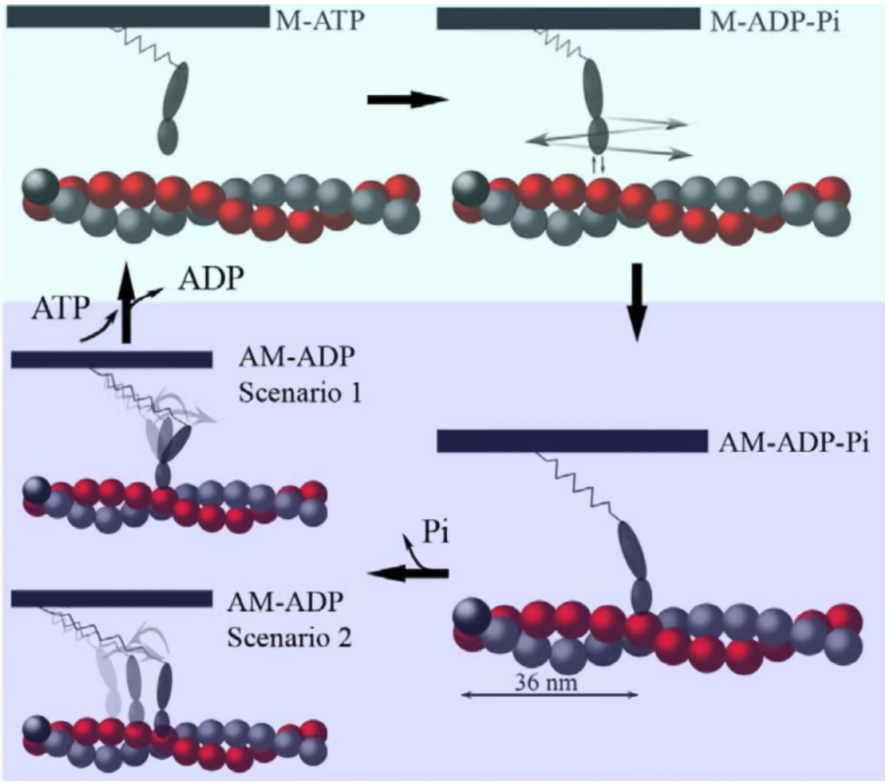

Figure 1.8: Two major theoretical mechanisms for myosin II dynamics. Scenario 1 represents the power stroke mechanism, defined as the generation of a large free energy gradient over a distance comparable to the myosin step size. Therefore, the transition to the forward binding site occurs nearly irreversibly. Scenario 2 is the Brownian ratchet mechanism, in which the motor head visits previous and forward binding sites through thermal fluctuation, and stabilization in the forward binding site. It occurs by the conformational changes triggered by the fuel processing event[110].

However, it would be difficult to distinguish which theory is more accurate because they both capture the myosin dynamics from certain aspects, and they are both supported by several experimental results[179,177]. In addition, the downhill of free energy in the Brownian ratchet can be regarded as a power stroke with a small swinging length. In fact, a hybrid model has been proposed that the myosin level arm is triggered to have a conformational swinging first and reach the adjacent binding site through a biased thermal fluctuation[44]. The accuracy of the two is highly dependent on the context, scale, and specific conditions of the system being studied. For instance, the power stroke mechanism has been well-accepted for the explanation of highly organized actomyosin structures, like skeletal and cardiac muscles. On the other hand, the Brownian ratchet mechanism has been more frequently applied to determining the myosin dynamics in non-muscle cells or at the single-molecule level where thermal fluctuations and stochastic events dominate. Nevertheless, these two mechanisms are highly likely to contribute to the actin-myosin interactions simultaneously and it is unnecessary to strictly distinguish them.

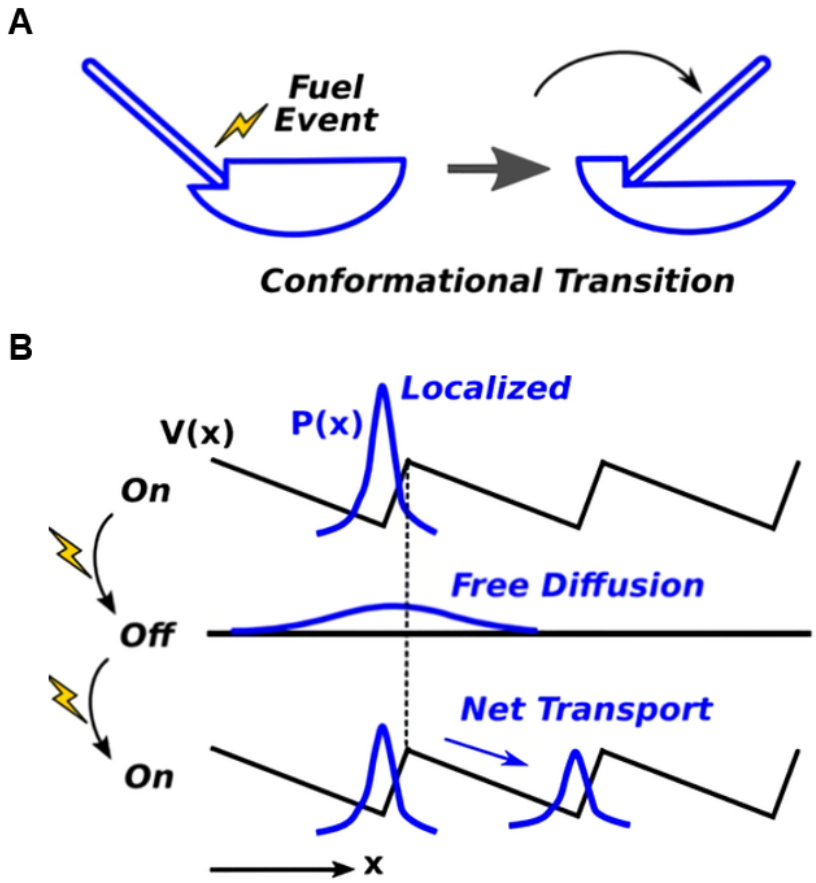

Figure 1.9: Explanations of the power stroke and Brownian ratchet mechanisms. (A) The explanation for the power stroke mechanism. A fuel event represents the binding of ATP or the release of an ATP hydrolysis product. It causes the conformational change of the motor head domain (converter) and subsequently alters the equilibrium position of the mechanical element (lever arm). (B) The explanation for the Brownian ratchet mechanism. V(x) denotes the potential on position x, which is asymmetric. P(x) represents the probability distribution. Free diffusion is allowed for the motor heads when V(x) is off. Once V(x) is turned on, motors undergo biased diffusion to the low potential position on the right[67].

1.4 Assembly and variations of myosin II filament

As introduced above, there are three isoforms of myosin II, including the striated muscle, smooth muscle, and non-muscle myosins. Myosin isoforms assemble into filamentous structures that exhibit considerable diversity in both size and morphology, with lengths ranging from approximately 0.3 μm to 1.5 μm and encompassing between around 56 and 800 myosin heads[171,25,134,156,127,173,147,62]. The structural arrangement of these filaments varies by myosin type and functional context. For example, smooth muscle myosin predominantly forms side-polar filaments, which are structurally distinct from the bipolar filaments formed by non-muscle and skeletal muscle myosins. Bipolar filaments are characterized by two clusters of myosin heads situated at either end of the filament and a central bare zone devoid of myosin heads, typically measuring around 160 nm in length (Fig. 1.10). This central bare zone plays a critical role in the filament's mechanical and functional properties.

The number of myosin II molecules within a filament is not fixed but is instead influenced by various physiological conditions, including pH levels and ionic concentrations[74,139,144,71]. Such environmental factors modulate filament assembly and stability, thereby tailoring the myosin filament's functional properties to specific cellular or experimental conditions.

A defining feature of individual myosin II heads is their relatively low duty ratio, which refers to the fraction of their enzymatic cycle spent in a strong actin-binding state. Unlike processive motor proteins, such as myosin V or kinesin, which exhibit high duty ratios and can continuously translocate along actin filaments, myosin II heads are bound to actin for only a small proportion of their operational cycle[80]. Consequently, a single myosin II head cannot sustain continuous movement along an actin filament on its own.

To overcome this limitation, myosin II molecules aggregate to form filamentous assemblies with multiple motorheads. This collective organization ensures that, at any given time, a sufficient number of myosin heads within the filament are engaged with actin filaments. This cooperative binding

mechanism enables the myosin II filament to maintain proximity to F-actin, facilitating efficient force generation and mechanical stability during cellular processes. The multivalent nature of the filament thus compensates for the low duty ratio of individual myosin II heads, ensuring robust interaction with the actin cytoskeleton under diverse physiological and experimental conditions.

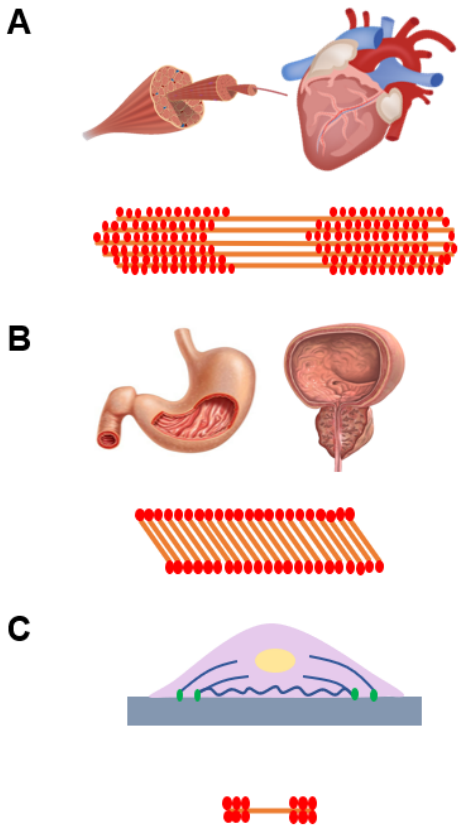

Figure 1.10: Variations of myosin II filaments. Depending on the cell type and other conditions like pH and ionic concentration, the structure of myosin II thick filament varies a lot, including the length, number of monomers, and if a center bare zone exists. (A) The thick filament in striated muscles is usually longer (around $1,600$ nm) and with many myosin monomers (around 300). A center bare zone exists, and the filaments are well arranged to generate forces in a certain direction. (B) For the thick filament in smooth muscle cells, there is no bare zone and its length (300 - $1,500$ nm) and monomer number (100 - 400) change depending on the tissue. (C) Thick filaments in non-muscle cells are bipolar structures with a bare zone. Their length (around 300 nm) and monomer number (around 30) are shorter and less than other cases [25,102,74].

1.5 Theoretical studies of force generation of myosin thick filaments

Myosin II filaments play a critical role in generating mechanical forces within actomyosin structures by interacting with filamentous actin (F-actin). The bipolar nature of myosin II filaments allows their heads, oriented with opposite polarities, to pull F-actins in opposite directions by walking toward the barbed ends of the filaments. This bidirectional pulling generates both tensile and compressive forces, particularly in disorganized actomyosin structures that differ significantly from the organized sarcomeres found in muscle cells [125].

Theoretical and computational studies have shown that F-actin is highly susceptible to buckling under compressive forces. As a result, disorganized actomyosin bundles or networks predominantly experience net tensile forces, which are key to mediating diverse contractile behaviors [95,96,133]. To understand these processes, various reconstituted actomyosin systems have been utilized. These systems have provided valuable insights into how contraction and force generation emerge from the interplay between F-actins, myosin II filaments, and actin cross-linking proteins (ACPs) [126,10,157,121,86,101]. Despite these advances, the influence of specific structural properties of myosin II filaments on contraction and force generation in disorganized actomyosin structures remains poorly understood.

Several computational models have been employed to study actomyosin contractility [2,3,4,22,161,183,94]. However, many of these models suffer from significant limitations. For instance, some models represent myosin II filaments as simplified structures, such as points [94,51], rods with only two binding sites [22,17,40], or force dipoles [146]. These abstractions fail to capture the complex architecture of myosin II filaments, which can significantly impact their functional behavior.

1.6 Sarcomeres in organized actomyosin structures

For striated muscles in most mammals incorporating the skeletal and cardiac muscles, their complex structures were initially understood through anatomical studies, revealing parallel fibers termed muscle fibers [52,159,113,182]. Further microscopic advancements revealed myofibrils within these fibers, delineated by periodically distributed sarcomeres, the fundamental unit of force generation [52,159]. These sarcomeres are mainly composed of proteins of myosin-II, F-actins, and ACPs like the α-actinin [113,182]. Along the myofibril, two dim lines termed Z-lines delimit a single sarcomere. In each of them, it is bisected by a central M-line which is covered by a symmetrical area with a deep color. This area is named the anisotropic band (A-band) because it demonstrates the overlap between the thin F-actins and the myosin thick filament. Similarly, the area with a shallow color that is adjacent to each Z-line is termed the isotropic band (I-band) due to its single component of the F-actin. In this contractile unit, barbed ends of F-actins are clamped symmetrically to the Z-lines, predominantly composed of ACPs, and are the boundaries of adjacent sarcomeres. A thick filament formed by myosin II proteins is centralized in the sarcomere by myomesin proteins in the M-line and the giant protein titin as well. This rigorous arrangement leads to a hierarchical structure that facilitates effective force development (Fig. 1.11). In addition, sequentially connected sarcomeres ensure rapid force generation on a macroscopic scale when the muscle is activated—such a stereotypical architecture results in a stable response to external forces.

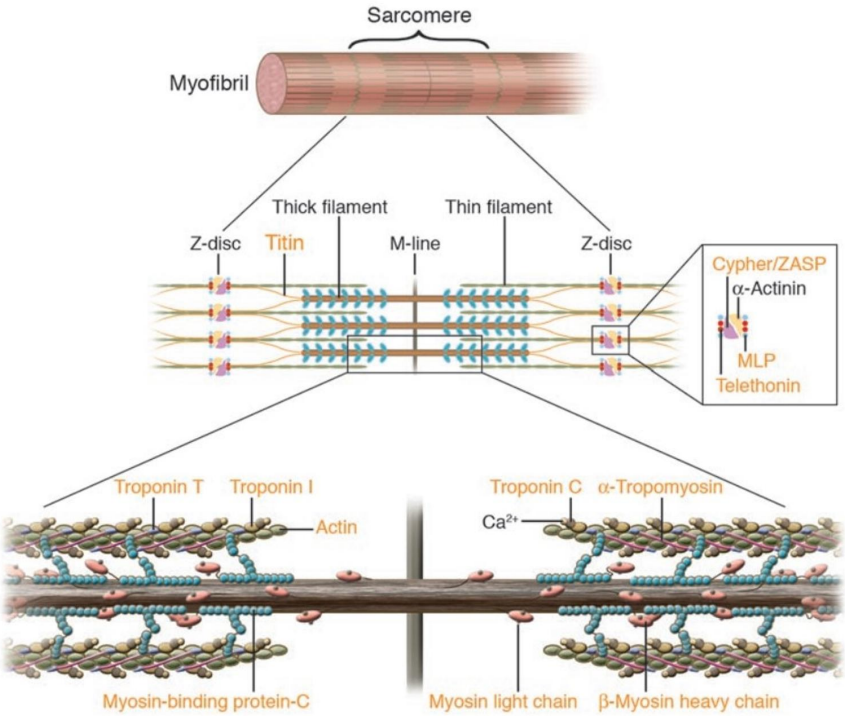

Figure 1.11: Sarcomere structure in striated muscle cells. Sarcomere thin filament proteins comprise actin, tropomyosin isoforms, and troponins C, T, and I. The bipolar myosin II thick filament is centralized by myosin-binding protein-C, and titin from the Z-line to the M-line. The sarcomere is anchored through titin and actin interactions with Z disc proteins including the α-actinin, where the barbed ends of the F-actins were clamped and the pointed ends were left free [124].

1.6.1 Current muscle modeling methods

Muscle modeling, which is used to analyze and predict force generation quantitatively, has become another important field that has attracted the attention of researchers, along with anatomy. Early muscle modeling efforts, notably A. V. Hill's pioneering work in 1938 [57], conceptualized muscles as elastic and contractile elements based on his observations of the in-vitro frog sartorius contractions, framing subsequent Hill-based models (Fig. 1.12). Their efficient recapitulation of the force-velocity relationship has lent credence to the idea that several mechanical elements can represent the muscle. Therefore, more Hill-based muscle models were reported by introducing different mechanical elements and arrangements in them, which resulted in more complicated descriptions of the muscle function [13,97,104,153,188]. However, it should be noted that the Hill model was built on a phenomenological study, which implies the components in it cannot be related to realistic structures in muscle directly. Therefore, to provide a compelling explanation for muscle contraction, the mechanism needs to be extrapolated from the molecular aspect.

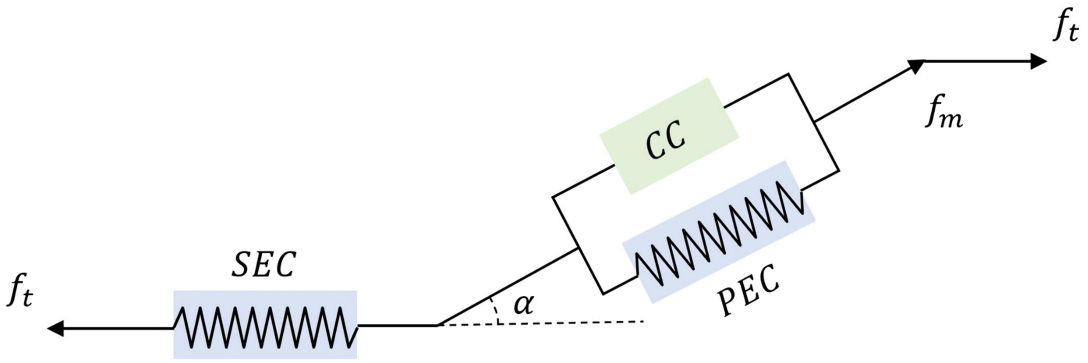

Figure 1.12: Diagram of Hill-based muscle model. *CC*, *PEC*, and *SEC* represent the contractile component, the parallel elastic component, and the series elastic component, respectively. f_t and f_m denote the muscle-tendon force and the muscle fiber force, respectively. α indicates the pennation angle between the longitudinal direction of muscle fiber and the acting direction of the muscle force. [194].

With the enhancement of protein understanding, the famous sliding filament theory was proposed based on precise experimental detections in 1954[65,63,66,64]. It explains that the mechanism of force generation in skeletal muscle results from the sliding interactions between the F-actins and the myosin thick filaments. According to its description, during muscle contraction, the A-band in each sarcomere is enlarged while the I-bands are narrowed down because of the two approaching Z-lines. Consequently, each sarcomere shrinks, and thus the whole muscle contracts. In the sliding filament theory, this phenomenon is induced by the active pulling on F-actins from the myosin. Moreover, associated with the sliding filament theory, the cross-bridge model was developed subsequently in 1957[63], which describes muscle contraction from a molecular perspective and has been a milestone in the field of muscle modeling. In this theory, actin and myosin are considered the main components for generating force. When the muscle is activated by the increase of calcium concentration, the myosin heads undergo an association with the binding sites on actins, forming connections termed cross-bridges with the F-actin as introduced in previous chapters.

Most of the molecular models based on thermodynamics detail muscle contraction by illustrating the actomyosin interactions. While widely accepted, they faced skepticism regarding their predictive accuracy. These models' inability to account for structural and energetic stability discrepancies in muscles raised significant doubts[128,54]. For instance, according to the cross-bridge-based models, the binding dynamics of the myosin ensemble should be determined stochastically. Hence, there should be a possibility that the number of bound myosin heads in two halves of a sarcomere exhibits a salient discrepancy. This theoretical situation would result in different contraction rates in a single sarcomere and would break its symmetry. However, on the contrary, experimental results present no evidence for such a prediction[54,58,122]. Although the sarcomere number in single myofibril varies to a reasonable extent, structural stability is maintained well during any physiological phase of muscle. Moreover, the passive stretch (stretch without the myosin activation) should lead to a fast slippage between the thin and thick filaments in accordance with the cross-bridge theory, because the myosin heads cannot bind

to F-actins in the low calcium condition to form the cross-bridges. In contrast, the in-vitro passive stretch of the muscle fiber still exhibits a certain resistance to the external tension, which indicates additional connections between the thin and thick filaments[99].

Furthermore, the cross-bridge model barely provides compelling explanations for the time-dependent properties of muscle regarding mechanical adaptation, especially the phenomena during the post-activation phase. Residual force enhancement (rFE) has been extensively studied in the field of muscle physiology[32,54,143,70]. It refers to a subsequent increase in the isometric force when a previously activated muscle is stretched beyond its rest length, compared to the output in the purely isometric shortening of an active muscle without prior eccentric contraction. However, according to the cross-bridge model, force generation should be identical with the same level of sarcomere length (SL) because of the actomyosin consideration. On the other hand, it lacks credibility in explaining the residual force depression (rFD) as well, which is the reduction in muscle force observed when a previously activated muscle is shortened compared to its isometric force after prior activation[1,130]. These discrepancies between predictions and observations demonstrate that the cross-bridge model is a simplified representation of the complex mechanics of muscles. It focuses on the interactions between myosin and actin, neglecting other potential mechanisms and factors that might contribute to the time-dependent properties of muscle. These phenomena of rFE and rFD can obtain an adequate explanation by postulating that an elastic element connects F-actins and the myosin thick filament and demonstrates an activation-dependent mechanical property.

1.6.2 Potential protein stabilizer for mechanical adaptation

Although the proteins including MyB-C and myomesin, can be associated with myosin thick filament and stabilize it at the center of each sarcomere, its contribution to the rFE and rFD is still unclear[55]. To elucidate muscle stability and its time-dependent properties for mechanical adaptation, researchers at-

tempted to ascertain potential mechanisms or factors that can complement the deficiencies of existing cross-bridge-based models. Decades after the cross-bridge model was proposed, researchers observed some extremely thin filaments can connect the A- and I-bands in striated muscle by using the electron microscope. However, the appearance of this new monomer was not depicted in detail at that time. It did not attract enough attention until Maruyama detected the existence of this giant protein with elastic properties and named it connectin initially 1976 [115]. Today, it is well known as the giant protein titin which is currently the largest protein in nature. With a mass of around 4.2 MDa, titin exhibits a length of half sarcomere, connecting the thin and thick filaments directly [172]. Additionally, the evidence of titin elasticity sheds light on a more precise muscle modeling, which can overcome the limitations of the pre-existing cross-bridge model. Since the advent of titin, a multitude of models has attempted to describe and simulate muscle mechanisms by including this giant protein.

Considering its molecular structure, as the largest known protein, single titin arranges from the Z-line to the M-line in vertebrate striated muscles, which is the half length of the sarcomere (Fig. 1.13). In such a long structure, titin monomer can be mainly divided into four segments based on their corresponding positions in the sarcomere. It includes the Z-line, I-band, I-band/A-band transition, and A-band segments connected in tandem [172,30]. Among them, the Z-line segment interacts with α -actinin and anchors to single F-actin through its amino terminus at the boundary between adjacent sarcomeres, while the A-band segment associates with the backbone of the myosin thick filament and binds to the M-line via its carboxyl terminus.

As a molecular clutch for muscle contraction, the I-band segment in titin exhibits tunable stiffness and plays predominant functions in force generation. It can be considered a composite elastic element that incorporates sub-segments with different mechanical properties. According to the components, the I-band segment consists of the proximal immunoglobulin (Ig) sub-segment near the Z-line segment, the N2 region, the PEVK sub-segment composed of proline (P), glutamate (E), valine (V), and lysine (K) residues, and the distal Ig sub-segment connecting to the A-band segment (Fig. 1.13).

Depending on the striated muscle types, these domains vary into different isoforms. For the highly extensible skeletal muscle like the soleus, the proximal Ig sub-segment is followed by an additional repeat of Ig domains and the N2 region exhibits a specific isoform termed N2A [172]. Meanwhile, its PEVK domains tend to repeat more than other isoforms. These variations induce the titin monomer in the skeletal muscle demonstrating the longest isoform, which facilitates muscle extensibility further. On the other hand, the titin isoforms in the cardiac muscle exhibit a shorter and thus stiffer I-band segment with different N2 regions including N2B and N2BA. For the spatial distribution, one myosin thick filament is connected by six titin monomers in each half of the sarcomere. These titin monomers associate in their distal Ig sub-segment and work in concert to stabilize the thick filament. Based on this structure, titin monomers in each half sarcomere can centralize the thick filament in both the longitudinal and the transverse directions.

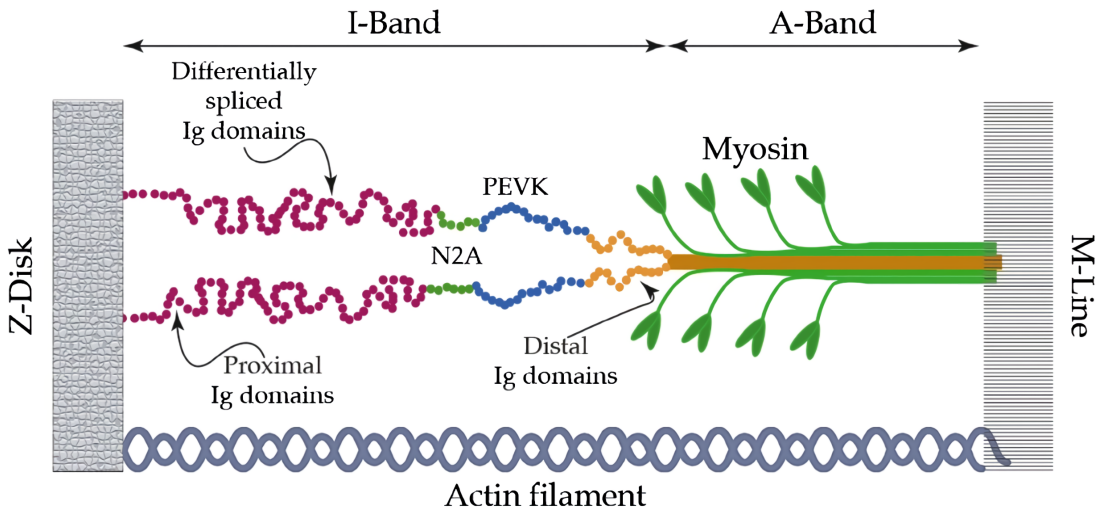

Figure 1.13: Diagram of titin monomers in half sarcomere. Titin is a giant protein that ranges from the Z-line to the M-line in each sarcomere, composed of multiple domains with distinct stiffnesses, including the proximal Ig domains, differentially spliced Ig domains, the N2 domain, the PEVK domain, and the distal Ig domains [33].

Due to the composite I-band segment, reactions of titin under the passive stretch express mechanical diversity, which predominantly depends on the extent of tension. According to the single-molecule experiments, the short linkers between proximal Ig domains in the titin express the lowest stiffness [172,128]. It indicates that the proximal Ig sub-segment will be straightened first during the passive stretch. Compared to that, the PEVK domains exhibit a higher stiffness and will be extended with further elongation. Different from these two regions, the distal Ig sub-segment presents the highest stiffness in this I-band segment because it associates with that in the other five titin monomers. This distal configuration forms a rigid-like end segment in the I-band/A-band transition segment, which enables a strong connection between titin and the myosin thick filament. It would be extended only when the SL exceeds the physiological range under high tension. However, in the straightened proximal Ig sub-segment, the polypeptides keep unfolding and refolding, which actively releases the tension on it. Further extension will unfold the PEVK regions subsequently. Therefore, during the single-molecule stretch, a saw-tooth-like force relaxation can be observed after a drastic passive stretch.

Although titin contributes to the sarcomere integrity significantly under passive tension, it can regulate the SL in a more reasonable and physiological range by conformational change. During the initial state of the muscle activation, the N2A region will bind to the F-actin which is triggered by the increase of calcium concentration. With this structural alteration, the proximal Ig sub-segment remains in a relaxed phase that prevents its extension and unfolding. Therefore, the stiffer PEVK domain and the distal Ig domain will undertake the tension from the slippage between the thin and thick filaments, which further shortens the rest length of the titin monomer and thus enhances its molecular stiffness significantly. During this initial phase, the elastic energy is stored in the activated titin temporarily, which prevents the sarcomere disintegration from the rapid eccentric contraction [54]. However, with the increase of calcium concentration, the cross-bridges between the thin and thick filaments will be formed. These additional connections will share the tension and enhance the structural stability as well. Consequently, the straightened titin will refold itself to release the tension and the stored elastic

energy. With this dynamic mechanism, titin monomer functions as a molecular clutch or a battery of elastic energy that can modulate the structural and energetic stabilities during active muscle contraction, facilitating muscle mechanical adaptation [128].

1.6.3 Theoretical muscle modeling for mechanical adaptation

Currently, building mathematical descriptions of titin based on experimental observations is one of the major approaches. In these theoretical models, the biological properties of titin are usually simplified by original assumptions. This type of modeling method can provide intuitional explanations for observations. For instance, in the "sticky-spring" model proposed by Rode et al. [145], an intriguing mechanism of titin was introduced, which can elucidate the rFE and rFD effectively and reasonably.

In this "sticky-spring" theory, the force generated by activated muscle was bisected into the active and passive parts. The active force is generated by the conventional actin-myosin interactions, while the passive force is attributed to the titin behaviors. The actin-binding events of the titin PEVK domains were described as a contender for the myosin-binding sites on the F-actin. In addition, the PEVK-actin attachment was assumed as a mechanosensitive association. It maintains a strong connection when the distal Ig sub-segment propagates a stretch toward the M-line. In contrast, this PEVK-actin attachment exhibits a higher unbinding rate if the pulling is toward the Z-line (Fig. 1.14). Furthermore, once the extensional force from the eccentric contraction exceeds its stall value, the distal PEVK part (near the distal Ig sub-segment) would unbind from the actin and then reattach to an adjacent binding site. Therefore, during the activated-stretch phase, the length of the PEVK-associated actin region gradually elongates, which results in the additional force bearing. By releasing this large storage of elasticity, the generated force in a subsequent isometric contraction can be enhanced significantly. This assumed sticky titin explained the rFE and defined the nomenclature of their theory as well. Moreover, since the PEVK domains compete with the binding sites with myosin, the

bound PEVK domains block a fraction of the cross-bridge formation during the activated compression, which further reduces the active force generated by actin-myosin interactions. This inhibition will be removed until the PEVK-actin attachment is pulled in the unpreferred direction. Therefore, the rFD can be explained by this "sticky-spring" titin as well.

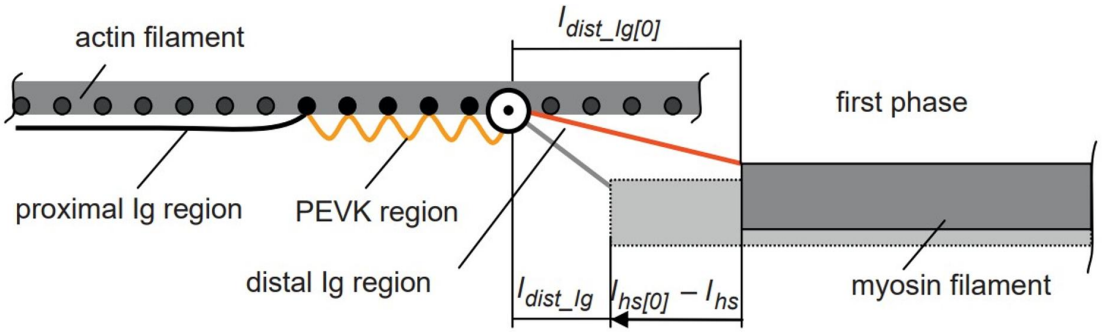

Figure 1.14: Diagram of the "Sticky-spring" model. The actin-binding events of the titin PEVK domains were described as a contender for the myosin-binding sites on the F-actin. In addition, the PEVK-actin attachment was assumed as a mechanosensitive association. It maintains a strong connection when the distal Ig sub-segment propagates a stretch toward the M-line. In contrast, this PEVK-actin attachment exhibits a higher unbinding rate if the pulling is toward the Z-line.[145].

However, this theory encounters significant skepticism when facing the following considerations. First, whether PEVK domains can compete with myosin for the binding sites is still controversial. In addition, recent evidence demonstrated that the N2A region of titin exhibits the actin-binding property as well[128]. Considering the vicinity of the N2A and PEVK domains, the interaction between the PEVK domains and the F-actin can be a consequence of the N2A-actin binding event. Nevertheless, this "sticky-spring" theory focused on the modeling of passive force, the Hill-based model was still adopted for the active part, which is well-known as a phenomenological model. Although this "sticky-spring" model represented the potential of titin for extrapolating the muscle time-dependent properties, its application is still debatable due to the unverified assumptions.

Differing from proposing a sticky performance of the PEVK sub-segment, Nishikawa et al.[131] focused on the binding dynamics of the N2A region and a subsequent winding of the PEVK part. Dur-

ing the muscle activation, the increase of calcium concentration leads to the N2A-actin binding interactions, which consequently shortens the rest length of the I-band segment. According to in-vitro experiments, a right-handed rotation of F-actin is induced by its interaction with myosin [123]. Based on this, Nishikawa et al. assumed that the cross-bridges formed in activated muscle would not only pull F-actins to the sarcomere center but also exert a right-handed torque on them. And because of the previous association of the N2A region, the tension-bearing PEVK sub-segment would be winded upon the rotating F-actin and further increase its effective stiffness (Fig. 1.15). The torque resulting from the cross-bridges will be balanced by PEVK and the orientation changes of α-actinins in the Z-line. Since this winding assumption is based on the actomyosin interactions, it highly depends on the shortening force and the energy stored in titin. For instance, when the sarcomere is under an isometric contraction, elastic energy stored in titin will be released. Meanwhile, the continuous actomyosin interactions keep winding the free PEVK which increases its energy storage. These two mechanisms are competing with each other during the contraction process. Therefore, when the contractile force from cross-bridges decreases with fast contraction, PEVK will unwind from the F-actin, which results in the energy release in titin. On the contrary, titin exhibits an increasing energy storage if the cross-bridges force increases with slow contraction. Based on this, a kinematic model was developed, in which parameters including the winding angle and filament rotation angle are related to SL and shortening velocity. In addition, the elastic potential energy in the PEVK sub-segment can transfer into the kinetic energy related to the shortening velocity. In this winding-filament model, PEVK kinematics are governed by a non-linear ordinary differential equation. With this setup, simulations regarding the force generation after an active stretch were conducted with different initial SLs. According to the results, significant force enhancements were obtained on the descending limb of the force-length relationship, which implies the model's feasibility for explaining the rFE. Additionally, energy transition from the force-bearing PEVK to kinetic energy during active compression brings relatively small cross-bridge force and subsequent unwinding of PEVK. Therefore, cross-bridges dur-

ing a later steady-state contraction need to rewind the titin, which leads to a depression of the overall force generation (rFD).

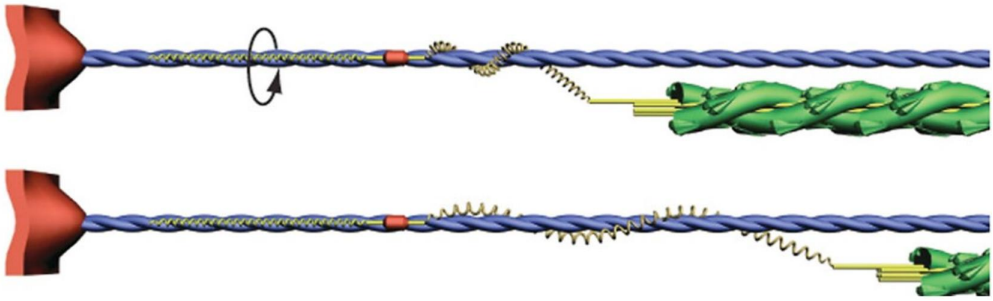

Figure 1.15: Diagram of the "Winding-filament" model. The cross-bridges formed in activated muscle would not only pull F-actins to the sarcomere center but also exert a right-handed torque on them. And because of the previous association of the N2A region, the tension-bearing PEVK sub-segment would be winded upon the rotating F-actin and further increase its effective stiffness.[131].

Although the winding filament model proposed a novel and reasonable hypothesis of titin based on real actomyosin observations, the N2A-actin interaction still requires more evidence. Alterations of the F-actin pitch were observed in activated muscle, which implies the filament rotation resulting from the actomyosin interactions[123]. However, direct evidence for the winding consequence of the PEVK sub-segment still awaits supplements.

Instead of proposing hypotheses of titin property, Herzog and his colleagues tried to adopt theories in polymer physics to describe the mechanics of this giant protein[152]. By considering the interactions among titin, F-actin, and myosin thick filament, they built a novel three-filament model (Fig. 1.16). As the essential theoretical part of their model, the worm-like chain (WLC) theory[112], which is mainly applied to fit the stretch experiments of DNA, was utilized to reproduce the mechanical response of the proximal Ig sub-segment. Based on single-molecule experiments, the number and individual length of residues in each titin segment were investigated, which can be calculated for the monomer contour length. Mechanical parameters including the persistence length of the Ig domain in different states and the elastic modulus of the PEVK domain can be obtained by fitting the passive stretch

test of single myofibrils. With these data, the relationship between the end-to-end length of one Ig domain and the force it requires to unravel can be determined according to the WLC model. This force-length relationship describes the unfolding dynamics of the proximal Ig sub-segment. Besides that, an extensible variation of the WLC model was adopted in this three-filament model for the most of PEVK domains that bear high tension during the active elongation. In this extensible WLC model, an additional elastic modulus of the PEVK domain was involved for the enthalpic compliance. Due to the sequential connections between those titin sub-segments and their spatial arrangement from the Z-line to the M-line, the force-elongation relationship of a half sarcomere can be calculated by assuming the total number of residues and a variable number of unfolding Ig domains. This three-filament model was first applied to verify the elastic contribution of titin in passive and active stretched half sarcomeres. The model demonstrated a significant force production with the passive condition. The force-SL relationship remained linear even in the sarcomere that exceeded its actomyosin overlap, which is consistent with the stretching experiments of myofibrils. With the active condition, a subsequent force increase can be produced by the model. It reflected the tunable stiffness of titin triggered by the high calcium concentration. This model further determined the influence of activation with different SLs. According to their simulation, the activation of a relatively long sarcomere (3.4μm) led to less force production in the subsequent extension compared to which activated in the optimal length (2.4μm). It was attributed to the passive extension of the proximal Ig domains before SL reached 3.4μm, which resulted in a shorter force-bearing PEVK sub-segment upon activation. This assumption facilitated the model to explain the time-dependent properties of titin as well. Regarding the rFE, a previous active stretch brings a longer PEVK sub-segment that already stored a certain extent of energy. This straightened stiff part will contribute to a larger contractile force compared to the isometric contraction activated in the same SL. Similarly, a previous active shortening leads to a shorter PEVK with stored potential energy, which resists further compression and results in a force depression compared to the isometric condition with the same SL (rFD).

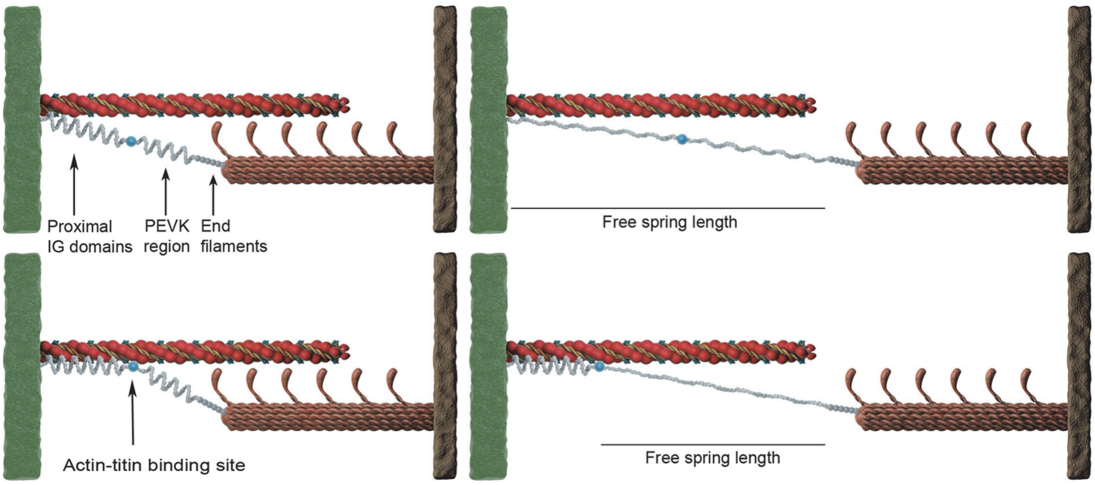

Figure 1.16: Diagram of the "Three-filament" model. Activation timing and the corresponding sarcomere length can alter the binding poison of the titin N2 region on the F-actin, which demonstrates distinct persistence length of the force-bearing PEVK domains. The upper row represents the passive stretch of a half sarcomere, whereas the bottom row denotes the active stretch of it.[152].

To demonstrate the advantages, hysteresis force production was simulated by using the three-filament model and the regular cross-bridge model, respectively. The predicted force was normalized to the isometric result with the same SLs. By using the conventional cross-bridge model, the predicted force was identical to the isometric contraction, while the three-filament model showed the enhancement and depression of force based on the active pre-extension or -compression, respectively. However, the discrepancies between the results from these models were not as significant as those have been revealed by experiments. In this three-filament model, only the most proximal part of the PEVK domains can associate with actin upon activation. It can be related to the N2A-actin interactions supported by the latest evidence[128]. However, the mechanochemical association between actin and the most of PEVK domains cannot be neglected, which would shorten the free I-band segment and increase the titin stiffness consequently. In addition, this three-filament model is limited to predicting force generated with the optimal and eccentric SLs. For the ascending limb of the force-length relationship, this three-filament model would face the challenges of the titin arrangement.

1.6.4 Mechanical element muscle modeling for adaptation

Different from theoretical models based on molecule observations, some researchers used mechanical elements to represent the components in sarcomere, including linear or non-linear spring, damper, and pulley. Similar to Hill-based muscle models, mechanical element models summarized here demonstrate high efficiency for generating force. The mechanical elements involved in these models are mostly related to real proteins and their mechanical properties, contrasting to the difficulty of the Hill-based model for linking the real muscle structure.

One efficient attempt is the spatially explicit model proposed by Powers and colleagues[142] (Fig. 1.17A). In their model, the components in a half sarcomere were all replaced by springs but with different mechanical properties, including F-actins, the backbone of myosin thick filaments, the cross bridges composed of chemically activated myosin, and titin monomers. The thick filament and the F-actin were represented by multiple serially linked springs with linear elasticity obtained from previous studies. Regarding the cross bridges, each of them followed the pre-established two-spring theory[185,186,187]. In this theory, each myosin monomer was defined by two linear springs representing the extensional and bending stiffnesses, respectively. Therefore, the myosin cycle described in the conventional cross-bridge model can be calculated in a more accurate manner by considering the distribution of the elastic and thermal energy and the effects of ATP concentration. For the titin monomer, a non-linear spring was utilized that connected the end of the myosin thick filament to the computational boundary. This non-linear titin exhibited an exponential force-length relationship governed by two tunable parameters, which were initially obtained by curve fitting (Eq. 1[142]). In this study, four myosin thick filaments, eight F-actins, and thirteen titin monomers were involved to form a three-dimensional half-sarcomere model, imitating the double-hexagonal lattice in real muscle (Fig. 1.17B). With this setup, the researchers investigated the influence of titin mechanical properties on structural and energetic maintenance during force generation. According to their simulations, higher titin stiff-

ness contributes to the increase of the actin-myosin overlapping during the descending limb of the active force-SL relationship. In addition, stiffer titin facilitates the rearrangement of myosin binding sites on F-actins. However, in contrast to the structural contributions, the higher stiffness of titin can reduce the capacity of force generation, according to their definition of contraction efficiency, which is the ratio between the contractile force and the ATP consumption. Researchers attributed this inverse relationship between titin stiffness and the contraction efficiency to the tension propagation from cross bridges to the M-line, which significantly diminishes with a less flexible thick filament.

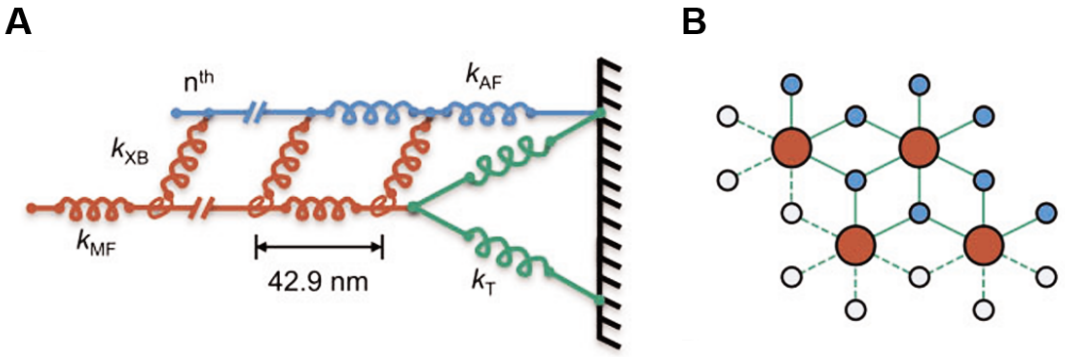

Figure 1.17: Diagram of the "Spatially explicit" model. (A) All the elements in a half sarcomere are simplified springs with different stiffnesses. The blue color represents the F-actin, the red color indicates the thick filament backbone and the formed cross-bridges, and the green color indicates the titin monomers. (B) Four myosin thick filaments, eight F-actins, and thirteen titin monomers were involved to form a three-dimensional half-sarcomere model, imitating the double-hexagonal lattice in real muscle.[142].

The enhancement of titin stiffness described in this analysis can be related to the decrease of the rest length in I-band titin, which is triggered by actin-titin interaction and the presence of calcium ions. However, the passive force generated by titin in this model simply increases with the elongation exponentially. There is no interaction between titin and other sarcomeric components. Additionally, despite a three-dimensional half-sarcomere with spatial considerations established in this study, titin contributions on the transverse distance among filaments were simplified constant during the contraction, which has been reported as a dynamic process in other investigations[56].

Instead of accumulating the mechanical effects of each myosin, some researchers decided to re-

gard all the cross bridges as an elastic array composed of parallel linear springs. Fusi and colleagues investigated the mechanical compliance of single myofibril and half sarcomere by applying the 4 kHz sinusoidal longitudinal oscillations and recording the force and length changes during the isometric contraction[43]. To fit the data of half sarcomere compliance, researchers first considered it as a summation of the cross-bridge array and filament compliances in their initial model. However, they noticed that a force-independent elastic element in parallel with the cross-bridge array was indispensable for recapturing the half sarcomere compliance during the early development of contraction. This parallel element demonstrates around 20 times higher compliance compared to the cross-bridge array. The authors ascribed it to weakly bound myosin and the myosin-binding protein C. However, there was still a discrepancy between the compliance values of half sarcomere and the myofibril. To overcome this problem, Fusi and co-workers incorporated an additional elastic element in series with the cross-bridge array. They defined this element with constant mechanical compliance and assumed it as a contribution from the tendon. However, a theoretical limitation occurs when explaining muscle compliance with a long SL. In a highly extended sarcomere, the cross-bridge array will be extremely shortened or absent. Based on this model, the compliance of the half sarcomere with a long SL will reach an infinite value. Pertici and colleagues noticed this issue and the potential of titin. They further developed this half-sarcomere model later by incorporating the mechanical contribution from titin[136]. In their updated model, the defined compliances of cross-bridge array and filaments remained. The most important assumption for involving titin in their model is that the strain of titin is equal to the summation of the F-actin strain in the I-band and the strain of the cross-bridge array at the end of the thick filament. Based on this, titin compliance can be obtained by calculating the alterations of force and SL. Accompanied by this titin-like elastic element in the I-band, Pertici and co-workers' model successfully prevented the half-sarcomere compliance from rising to an infinite level with a lower active force. According to their simulation, during the development phase of isometric contraction, this titin-like element exhibited a similar function as the parallel spring in the A-band which

was attributed to weakly bound myosin and the myosin-binding protein C. They both enhanced the compliance of the half sarcomere with the increase of SL during the ascending limb [136]. Powers and colleagues, who established the spatially explicit model, noticed that this mechanical element model demonstrated advantages in the longitudinal stability of the myofibril. They further developed Pertici's titin-incorporated model by involving the A-band parallel spring, which was initially determined in Fusi's study [140]. By comparing the difference between these two models, researchers determined that the A-band parallel spring predominantly resulted from the weakly bound myosin instead of the myosin-binding protein C due to the increase of its compliance only in ascending limb. According to their simulation, the mechanical contribution of the titin-like element started when the force was rising to the isometric plateau and its compliance was approximately maintained constant during the eccentric contraction. It implied that titin functions as a tunable elastic element during the descending limb, which fits the experimental observations of the continuous folding and unfolding processes of the proximal Ig sub-segment [100]. Most importantly, this computational work revealed titin's potential for preventing SL inhomogeneity. When serially connected sarcomeres exhibit diverse contractility, titin monomers as tunable elastic elements play an essential role in balancing force development, thus maintaining most sarcomeres in their physiological SL [158]. However, this mechanical element model was still lacking the description of actin-titin interactions. In addition, all the parameters were set with a saturating level of the calcium ion, which implies the stiffness enhancement of titin based on muscle activation was neglected in this model.

To incorporate the actin-titin interactions, Tahir and co-workers [164] decided to adopt Nishikawa's winding filament theory [131] in their mechanical element model, which is introduced in the section of the theoretical model. Inspired by the conventional Hill-based muscle model, the cross-bridge was represented by a contractile element (CE). The force-velocity relationship of myosin (C_{ce}) was replaced by a damper in parallel with the CE, which has two different sets of parameters for calculating muscle elongation and shortening. Titin monomer was described as a linear spring (k_{ts}) connected to CE

and C_{ce} through a pulley in a non-slip configuration. When the muscle is activated, the contraction of CE will rotate the pulley in a counterclockwise direction, which pulls the titin spring and winds it on the pulley. The generated elastic force will resist further winding, which recaptures the force and energy description in the winding filament theory. Once the muscle was deactivated, the titin spring would release the elastic potential and roll the pulley in a clockwise direction. Another linear spring (k_{ss}) representing other elastic components in muscle including the tendon, extracellular matrix, and aponeurosis, was in series with the system by linking the center of the pulley. It would not be affected by the rotation of the pulley but by its displacement. Based on this model structure, researchers developed their winding filament hypothesis (WFH) based control algorithm and applied it to a robotic foot-ankle prosthesis. According to their case study, this WFH algorithm can govern the prosthesis movement transitions smoothly between the stair ascent and level walking. Compared to a commercial controller, the WFH-based controller could provide a wider range of ankle plantarflexion angles, implying the feasibility of applying the molecular muscle models for adaptive prosthesis control. Further refinement of this WFH model was conducted by Nishikawa and Huck by adding a damper in parallel to the titin-like spring to represent its non-linear stiffness [129]. By treating the muscle as a tunable material, this WFH-based muscle model demonstrated an instructive attempt to utilize the muscle properties from the molecular level directly to the development of the artificial muscle in tissular level. However, only two subjects were applied in their algorithm establishment. Further experiments should be conducted to verify the common feasibility of incorporating titin properties in control theories. In addition, investigations about the parameter sensitivity are still required to develop a robust control system.

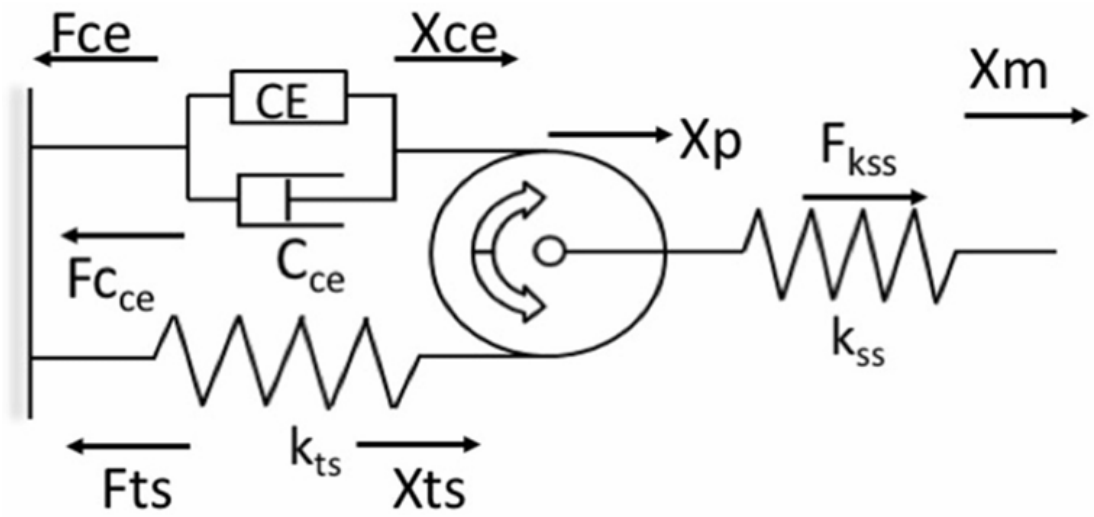

Figure 1.18: Diagram of the "Multiple-element" model. The cross-bridge was represented by a contractile element (CE). The force-velocity relationship of myosin (C_{ce}) was replaced by a damper in parallel with the CE, which has two different sets of parameters for calculating muscle elongation and shortening. Titin monomer was described as a linear spring (k_{ts}) connected to CE and C_{ce} through a pulley in a non-slip configuration. Another linear spring (k_{ss}) representing other elastic components in muscle including the tendon, extracellular matrix, and aponeurosis, was in series with the system by linking the center of the pulley.[164].

1.7 Sarcomeres in disorganized actomyosin structures

Considering non-muscle cells, however, their intracellular architectures are more disorganized compared to striated muscles. Stress fibers (SFs), which are regarded as the source of contractile force, are the main component of cytoskeleton that maintains the cell structure during its biological processes[39,5]. According to their intracellular position, SFs can be divided into four categories including the ventral stress fibers, dorsal stress fibers, transverse arcs, and the perinuclear actin cap fibers[135]. Among them, the ventral stress fibers are indispensable for the morphology maintenance by connecting two focal adhesions (FAs) during their force generation[168] and localize at the basal part of the cell. Strikingly, sarcometric patterns have been observed in the ventral SFs as well, in which immunostaining α-actinin-rich domains present a regular distribution, and the fluorescent myosin light chains (MLCs) has been detected between two adjacent ACPs domains that indicates myosin-II proteins reside in the central position[50,16] (Fig. 1.19). Such experimental results lead to the hypothesis that sarcomeres in non-muscle cells have a similar mechanism to that of in striated muscles, and bipolar thick filaments are formed by myosin-II monomers which are usually considered as the origin of contractile force and SFs elasticity[15,93,184]. Considering the transverse arcs, they were predominantly observed at the cell apical part. They maintain a certein contractility becasue of the incorporation of myosin thick filaments, but the components distribution are further disordered and there is no sarcomeric structures. Dorsal stress fibers localize at the cell dorsal area and connect to FAs at one end of them, another end usually associates to the transverse arc or is left free. Different from other SFs, the perinuclear actin cap fibers extend a long distance over the cell and associated with the cell nucleus on top via the LINC complexes[108].

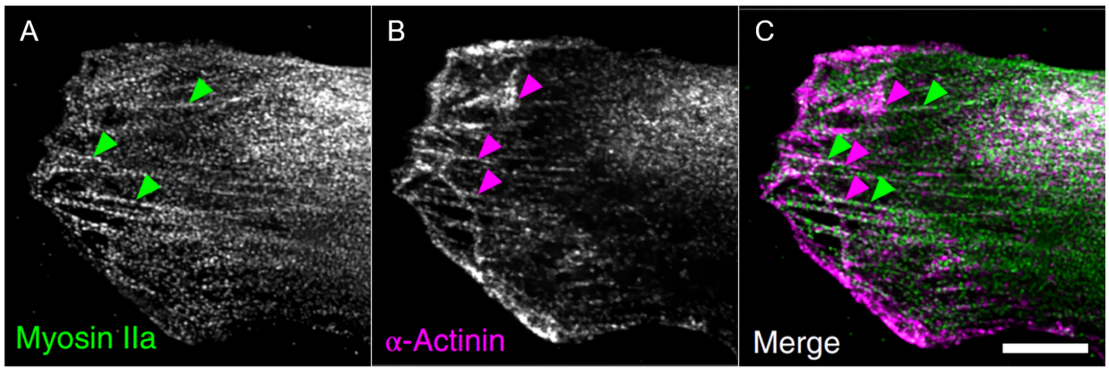

Figure 1.19: Periodic distribution of sarcomeres in stress fibers. (A) The green color denotes the myosin distribution; (B) α-actinin-rich domains are shown in the magenta color; (C) Merge of the distributions of the two protein types. Periodic patterns can be observed and defined as the sarcomeres in stress fibers, resembling the sarcomeres in striated muscles. [16].

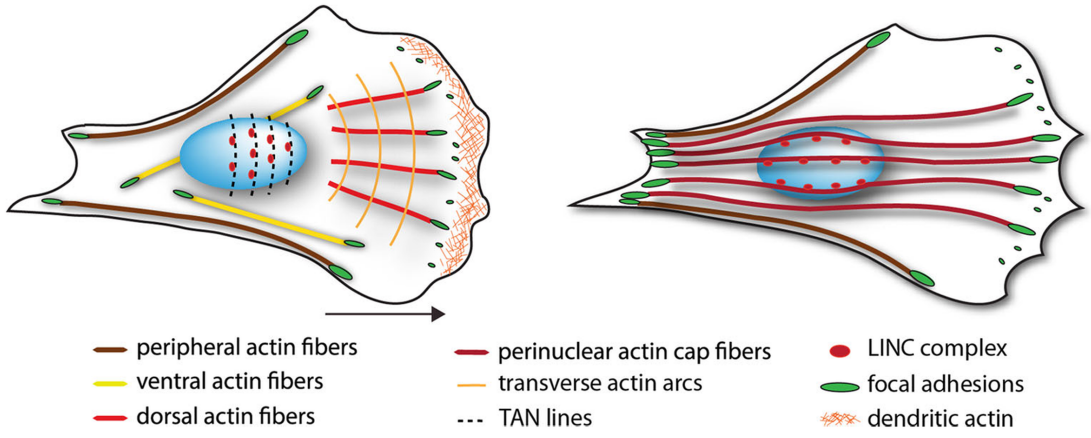

Figure 1.20: Different types of stress fibers. [108]

1.7.1 Formation of the sarcomere

Unlike the stereotypical striated muscle, there is no regulator like titin to contribute the bundle assembly in non-muscle and smooth muscle cells. Many researchers attempted to explore the underlining mechanism and buildup compelling theories. For instance, Herrera and et al have reported a observation of the "dense body (DB)" in smooth muscle fibers[53] (Fig. 1.21). They proposed that these DBs can function as the "Z-line" and clamp the side-polar myosin thick filaments at the center. Therefore, the DB-thick filament-DB unit was consider a single sarcomere. A DB-based model was designed subsequently and applied for the force simulations with different arrangements of the sarcomeres. Meanwhile, the stretch experiments in this study demonstrated the smooth muscle adaptation to changes in cell length. The muscle fiber can adjust and optimize its overlapping level between the thin filaments to maintain the ability for generating the maximal force, depending on a different cell lengths. A numerical simulations based on their DB theory was conducted as well, and the results could fit the force-SL relationship observed in the experiment, supporting the theory's capability. However, as shown in the observation from the longitudinal view (Fig. 1.21 (C-E)), multiple thick filaments localized in serial between two DBs, which is different from the model configurations. Nevertheless, the exact biological components in the DBs were not investigated and their distribution in the longitudinal direction did not be obsered in a periodic pattern.

Considering the disorganized contractile actomyosin bundles, including the transverse arcs and the contractile rings, there are not detectable sarcomeric structure as that in the ventral stress fibers. Lenz and the coworkers proposed a theoretical model accounting for the micro-buckling between myosin thick filaments[95]. By observing the buckling and recovery of F-actins in actomyosin bundles, researchers assumed the actin-myosin interactions play vital roles in these processes. Motor walking speeds in their model varies depending on the stochastic binding condition and the local tension following their catch-bond properties[166]. Based on the distinct walking speed, the combination of a fast

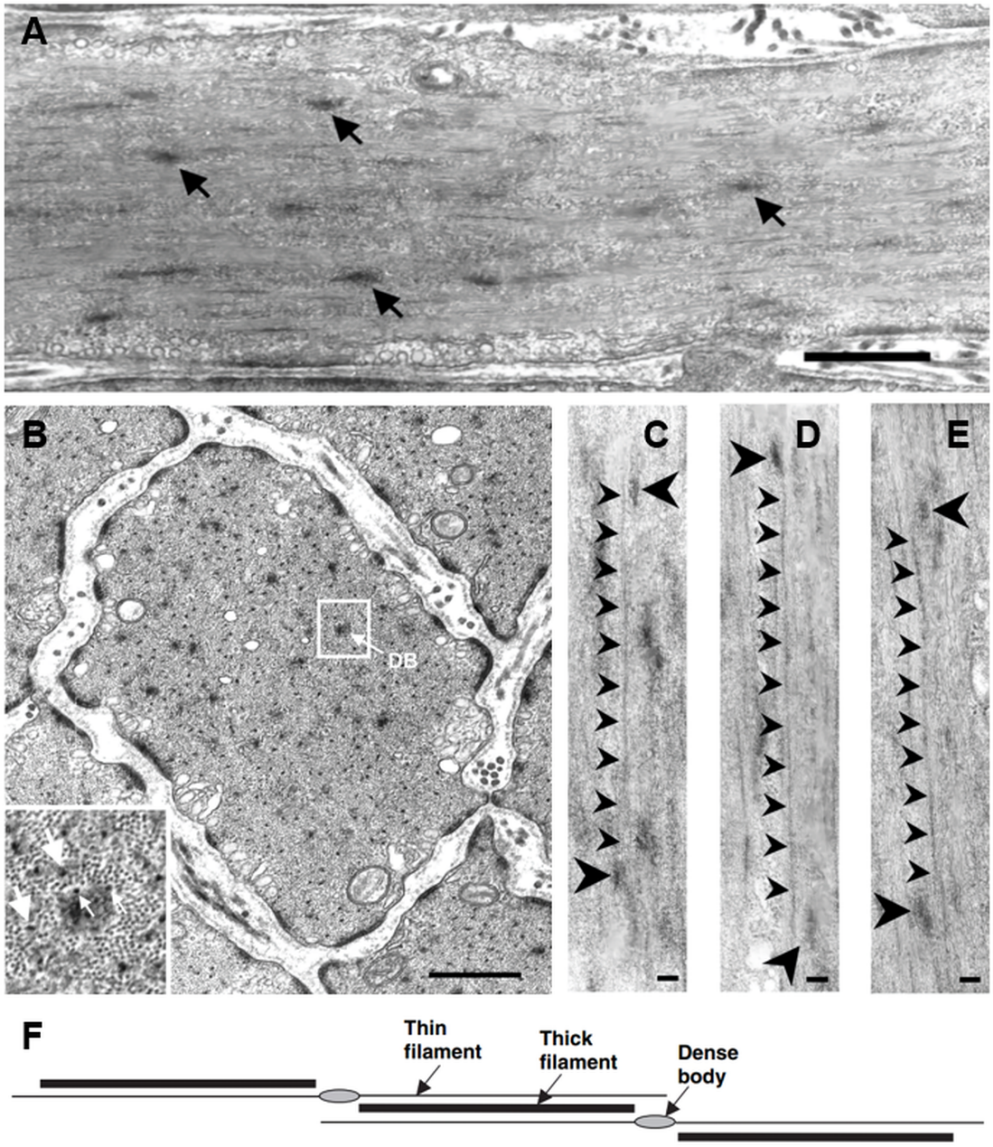

Figure 1.21: "Sarcomeres" formed by the dense bodies in smooth muscle fibers. (A) Longitudinal view of the dense bodies (DBs) observed in smooth muscle fibers. The black arrows denote the DBs; (B) Cross-sectional view of the smooth muscle fiber showing the existence of DBs. The magnified portion demonstrates multiple thin filaments surrounding the DB. The small and large arrrows in this section indicate the intermidiate filaments and the thick filaments, respectively; (C-E) Relative distributions between DBs and myosin thick filaments. The large arrows are the DBs, and the small arrows represent the locations of thick filaments. (F) The Dense body model, in which DBs function as the Z-lines clamp each myosin thick filaments and form the sarcomeres in the smooth muscle fibers.[53].

and a slow motor will result in a micro-buckling of one F-actin they associate with and another F-actin will be stretched. The repetition of this combination can lead to a periodic distribution of the buckled parts. They defined the bundle part between two micro-buckles as one contractile unit. The continue actin-myosin interaction can remove these micro-buckles. At the same time, the unbinding of motors once they reach to their stall force value will release the tension on the F-actins. Based on these setup, their one-dimensional model can predict the size of contractile units and the required motor density for contraction in agreement with the magnitude of experiments, suggesting the micro-buckles of the F-actins and the myosin dynamics contribute to the mechanical adaption in the non-sarcomeric actomyosin bundles. However, they did not incorporate any ACPs in their theory, which has been already investigated to function as a force-balancer in a certain extent and enhance the bundle connectivity as well. With the connections from ACPs, F-actins can be separated with each other and be bended easier, which is not consistent with the real actomyosin bundle and would overestimate the effects from motors.

One compelling theory related to the sarcomere formation in ventral stress fibers was proposed by Hotulainen and Lappalainen in 2006[60]. They revealed that the ventral stress fibers are formed by the growing dorsal stress fibers and transverse arcs. In addition, two distinct mechanisms were observed for the assembly of dorsal stress fibers and transverse arcs, which is related to the actin nucleators of mDia1 and Arp2/3, respectively. According to their experiments, the growing dorsal stress fibers continue elongating until they reach a transverse arc at the cell apical part. These associated dorsal stress fibers and transverse arcs will gradually settle down to the cell basal part and become a ventral stress fiber. This theory has been widely discussed but facing a major skepticism regarding how the periodic sarcomeres in ventral stress fibers are rearranged from the non-contractile dorsal stress fibers (without myosin) and the disorganized transverse arcs (random polarities of F-actins). Therefore, to overcome this limitation, the team focused on the myosin-regulation function of tropomyosin isoforms[169,168]. They observed that myosin light chains (MLCs) were always co-localized with the tropomyosin iso-

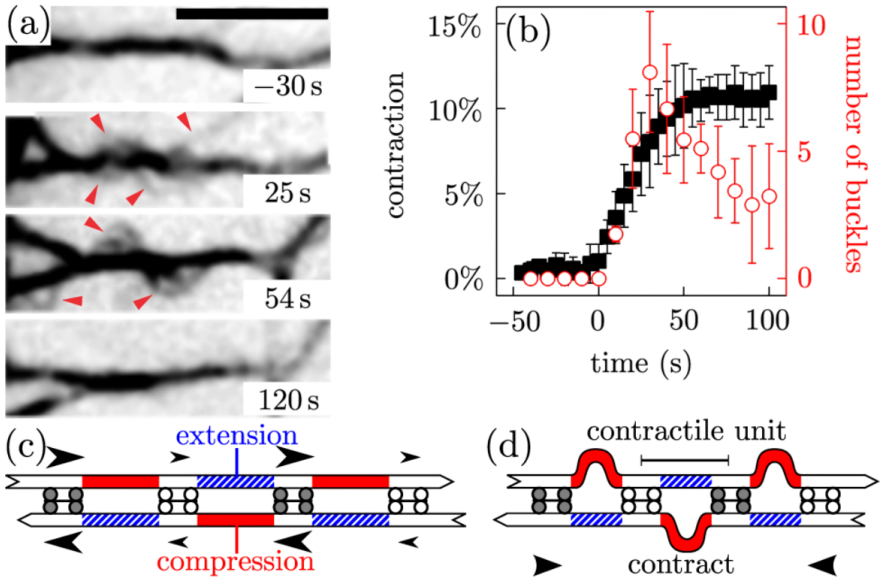

Figure 1.22: Micro-buckling in the non-sarcomeric contractile actomyosin bundles. (A) Time-lapse images showing the micro-buckling of F-actins in a non-sarcomeric actomyosin bundle and its subsequent recovery. The red arrows denote the buckling filaments. (B) The bundle force (solid squares) and the number of buckles (red circles). (C) Potential extension and compression parts along the bundle based on motors with different walking speeds. (D) Micro-buckles occur between a fast motor and a slow motor. Large and small arrows denote the large and small contractile forces, respectively. Motor with a gray color represents a fast one, whereas the white motor indicates the slow motor.[95].

form 4.2 (Tpm 4.2). Considering the function of tropomyosin in non-muscle cells, it resembles that in striated muscle sarcomeres for associating with F-actins and covering the actin-binding sites on it when the muscle is not activated[47,154]. As for the actin, tropomyosin prefers binding to a relatively long F-actin that can be generated by mDia2. Unlike mDia2, the actin nucleator of Arp2/3 tends to assemble shorter actin filament from a pre-existed F-actin, thus it usually results in branch structures in cytoskeleton[48]. Therefore, ACPs can only associate with the short F-actins from Arp2/3 because most of the long F-actins would be occupied by tropomyosin which blocks the actin-binding sites. Following this, myosin thick filaments can associate with the tropomyosin-decorated F-actins once they are activated and the binding sites are exposed. With the polarity sorting ability of myosin[160,93], a periodic pattern with two α-actinin-rich domains clamping the thick filament incorporating domain can be formed in a ventral stress fiber (Fig. 1.23).

However, there is no architecture like the M-line in striated muscles that can localize the myosin thick filaments near the center of sarcomeres. Furthermore, some evidence showed the non-muscle sarcomeres are not uniform and their amount in a single SF alters depending on the local tension[18]. Based on these uncertainties, SFs exhibit diverse responses when the mechanical environment shifts. For instance, with a small shortening strain (16%) *in vivo*, sarcomeres in different regions of the SF are not compressed equally, which implies their mechanical adaptation[137]. However, significant buckling of SFs was observed under a larger compression (40%) according to our previous *in vivo* studies[26]. In addition, the high extensibility of SFs was determined by previous experiments *in vitro*, which implies their inherent viscoelasticity[119]. Such a mechanical property has been proved and quantitatively detected by calculating the retraction distance after the ablation of SFs[88,165,76]. Furthermore, non-muscle SFs are highly dynamic when the mechanical environment changes rapidly. If the SFs are compressed at a high rate, they will disrupt and reassemble themselves after the loading[23,62]. Interestingly, under the condition of cyclic stretch, SFs will reorganize and reorient to the direction that is perpendicular to the loading[180,79,90]. Nevertheless, by changing the rate of cyclic stretch, recent exper-

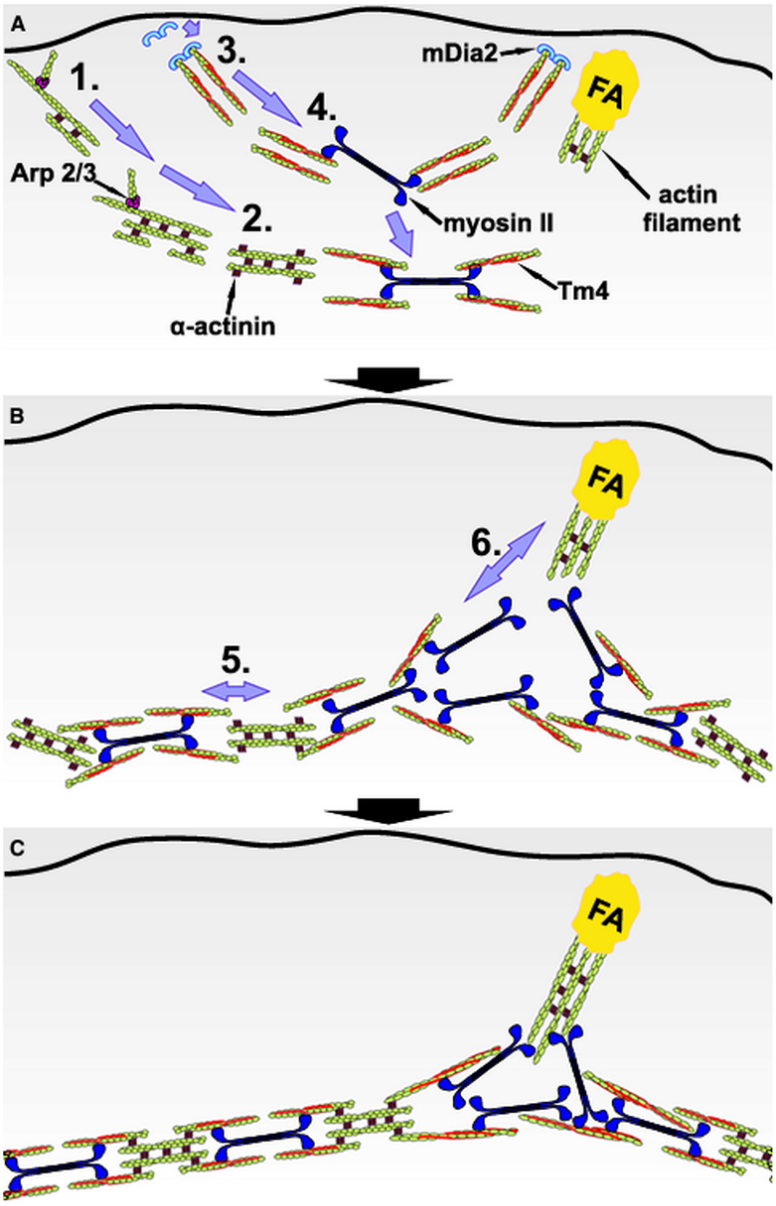

Figure 1.23: Formation of the sarcomeres in ventral stress fibers. α-actinins can only associate with the short F-actins from Arp$2/3$ because the long F-actins from mDia2 would be occupied by tropomyosin (Tm4) which blocks the actin-binding sites. Following this, myosin thick filaments can associate with the tropomyosin-decorated F-actins once they are activated and the binding sites are exposed. With the polarity sorting ability of myosin, a periodic pattern with two α-actinin-rich domains clamping the thick filament incorporating domain can be formed in a ventral stress fiber[169].

imental studies confirmed that SFs tend to disrupt under a fast compression rather than the stretch and a slow compression, in which the myosin thick filaments play an important role in this unbundling and the subsequent remodeling [116,62]. These phenomena can be explained as that SFs can bear more extension load while they are more sensitive to the compression force.

As introduced above, SFs are composed of not only actins and myosin but also ACPs that contribute to bundle connectivity. In addition, considering a single myosin ensemble in the sarcomere only cannot provide elucidations for the overall mechanical properties of SFs, in which a myriad of them works simultaneously. In this regard, some researchers attempted to model the SFs from the continuum perspective. For instance, sarcomeres are simplified as a combination of elements including spring, damper, and contractile force generator [11,132]. SFs in several studies are simplified as elastic elements and this consideration has been extended to the cellular scale for applying the finite element method (FEM) [138,148,149]. These continuum-based models provide a simple approach that can recapitulate the basic mechanical properties of SFs. However, regarding the individual function of different protein types and their synergistic effects, continuum-based modeling usually encounters skepticism. Hence, to overcome those limitations and provide cogent elucidations for the bundle mechanical response, we applied our compelling agent-based model with realistic structures of SFs proteins and their dynamic properties and combined with an in vitro single-fiber experiment to comprehend the molecular contributions to the mechanical adaptation of actomyosin bundles.

1.8 Aim of this study

As mentioned before, many myosin-related models oversimplified the structure properties of the thick filament. In this study, we address these limitations by employing our well-established agent-based model. This model incorporates detailed representations of myosin bipolar filaments, including their number, length, bare zone size, and spatial distribution [96,12,106,73,82,193]. Using this comprehensive

approach, we aim to elucidate how these structural features of myosin filaments influence force generation within disorganized actomyosin bundles and networks. Meanwhile, how the sarcomeric structure in SFs contribute to the mechanical adaptation in non-muscle cells is another question aimed to be answered in this study. Unlike the stereotypical structure in striated muscles, the highly labile actomyosin architecture provides a flexibility for the contraction depending on the mechanical environment. By applying our agent-based model and an in vitro single-fiber experiment, our study aims to investigate the fundamental mechanism of the SFs mechanical adaptation based on the actin-myosin interactions. By bridging the gap between structural properties of myosin thick filament and functional outcomes, our work provides a deeper understanding of the mechanical principles underlying actomyosin contractility.

I can see the sun,

but even if I cannot see the sun,

I know that it exists.

And to know that the sun is there -

that is living.

Fyodor Dostoevsky, *The Brothers Karamazov*

2

Impacts of Structural Properties of Myosin II Filaments on Force Generation

As the widely known motor protein, isoforms of myosin have formed a superfamily and have been investigated for decades [163]. Depending on the molecular structures and cell types, myosin isoforms function as a force generator, mechanical sensor, and cargo transporter. More than thirty-five

isoforms have been reported in nature, and they are indispensable for a myriad of cellular processes, including cytokinesis, migration, vesicle transport, and morphogenesis[98].

2.1 Model overview

The details of our computational model, along with all parameters used, are comprehensively described in the Appendix Text and Appendix Tables. Our model focuses on three essential cytoskeletal components—F-actin, motors, and actin cross-linking proteins (ACPs)—simplified from the more than 100 proteins typically found in cellular actomyosin structures[103] (Fig. 2.1A). These components are represented as cylindrical segments (Fig. 1A). Specifically, F-actin is modeled as serially connected segments, each 140 nm in length. ACPs are depicted as having two arms, each 23.5 nm in length, connected at a central point. To replicate the structure of bipolar filaments, each motor comprises a backbone made of serially linked segments and two arms at each end of the backbone. These arms represent eight myosin heads (N_h = 8). The reference length of each backbone segment (L_{MB}) is 42 nm.

The displacements of all cylindrical segments at each simulation time step are calculated using the Langevin equation in combination with the forward Euler integration scheme. Deterministic forces in the Langevin equation account for extensional and bending forces, which maintain the equilibrium lengths of segments and equilibrium angles formed by the segments, respectively. Additionally, a repulsive force is applied to overlapping actin segments to account for volume-exclusion effects.

Using this model, we simulate three distinct systems: two filaments, bundles, and networks (Figs. 2.1and 2.2). In the two-filament simulations, a pair of anti-parallel F-actins, each 19 μm in length, is placed within a rectangular computational domain measuring 5 × 5 × 20 μm (Fig. 2.1B). Periodic boundary conditions (PBC) are applied in the x and y directions, while a repulsive boundary condition is imposed in the z direction. The barbed ends of the F-actins are clamped to finite boundaries normal

to the z direction.

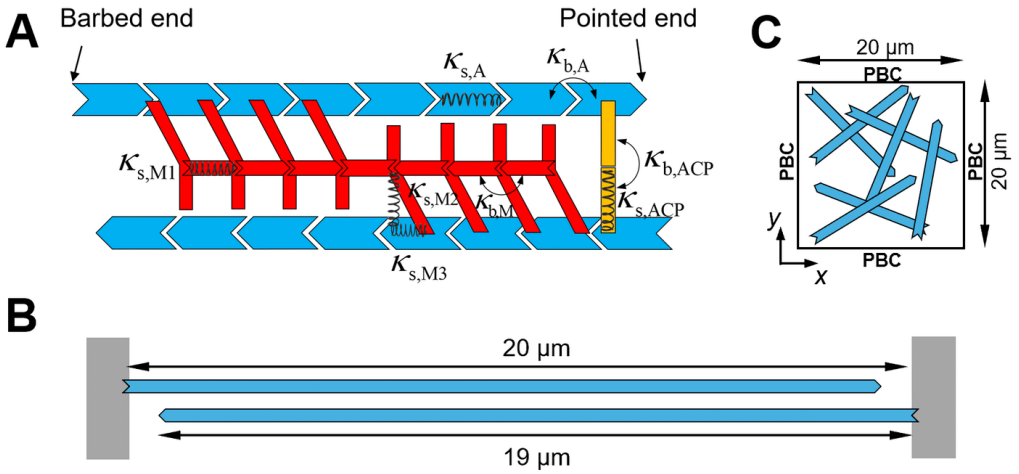

Figure 2.1: Cylindrical elements and structures of the two-filament and the network models. (A) In the model, F-actin (blue), actin cross-linking protein (ACP), and motor (red) are simplified by cylindrical segments. F-actin has polarity defined by barbed and pointed ends. Motors consist of a backbone with motor arms that can bind to and walk along F-actin. ACPs comprise two segments connected at the center point. κ_s and κ_b represent extensional and bending stiffness, respectively. (B) The two-filament system consists of two F-actins whose barbed ends are clamped to rigid boundaries (gray). (C) The two-dimensional network system consists of F-actins with random positions and orientations with the periodic boundary condition (PBC) in x and y directions.

For bundle simulations, the same rectangular domain is used, with PBCs applied in all directions (Fig. 2.2A). Following our previous work[82], F-actins are positioned at specific x and y coordinates. The number of possible positions in the x or y direction is determined by N_F, and the spacing between adjacent coordinates is set to 27 nm. At each x-y coordinate pair, two F-actins, each 9 μm in length, are positioned randomly along the z-axis with random polarity. Consequently, the total number of F-actins in the bundle is given by $2N_F^2$ (Fig. 2.2B).

In network simulations, a thin rectangular computational domain measuring 20 × 20 × 0.1 μm is employed with PBCs in the x and y directions and a repulsive boundary condition in the z direction (Fig. 2.1C). Within this domain, F-actins, each 10 μm in length, are randomly distributed with respect to their positions and orientations. At the start of all simulations, while the F-actins remain

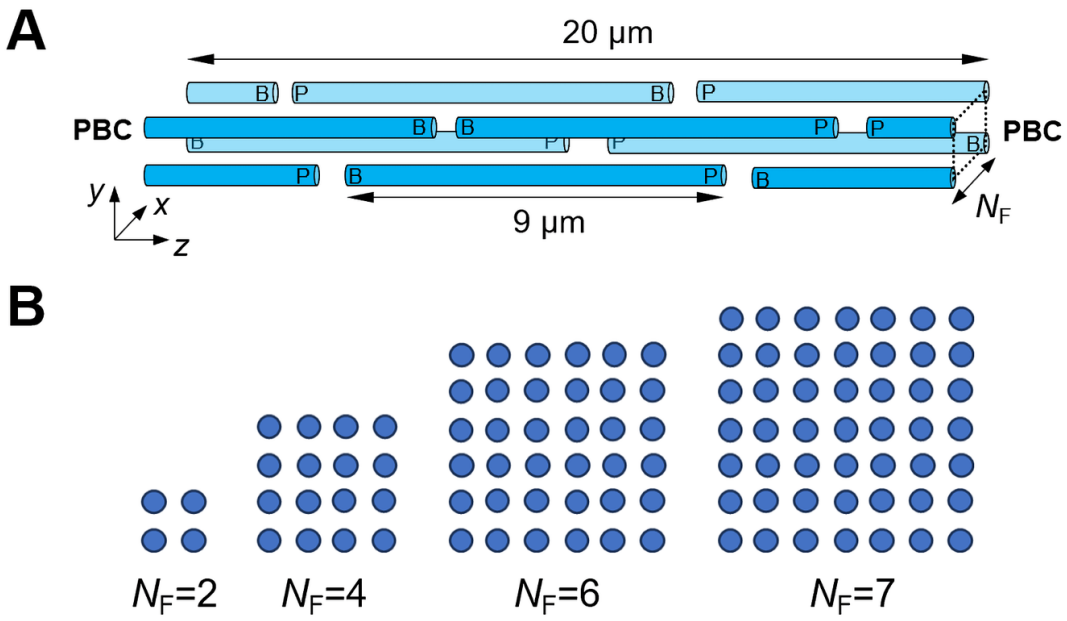

Figure 2.2: Model structure of the disorganized bundle. (A) The disorganized bundle system with $2N_F^2$ F-actins randomly located and oriented in the presence of the periodic boundary condition (PBC) in the z direction, where N_F is a parameter defining the bundle thickness. (B) In this study, the values of N_F were 2, 4, 6, and 7, corresponding to the F-actin numbers of 8, 32, 72, and 98.

stationary, ACPs bind to F-actins to form permanent cross-linking points. Simultaneously, the motor arms, which self-assemble from backbone segments, attach to F-actins. After this initial setup, F-actins are allowed to move freely, and the motor arms commence their walking and unbinding processes at force-dependent rates.

2.2 Variations in motor structures

In this study, we systematically investigate the impact of three key structural properties of motor proteins: the number of arms per motor (N_a), the length of the bare zone (L_{bz}), and the spacing between motor arms (L_{sp}). To explore how motor size influences force generation and dynamics, we modify these properties using three distinct approaches.

In the first approach, the number of arms per motor (N_a) is increased by connecting additional segments with arms to the motor's backbone. In this configuration, the length of the bare zone (L_{bz}) and the spacing between motor arms (L_{sp}) are kept equal to the reference length of the backbone segment (L_{MB}) (Fig. 2.3, i). This method allows us to isolate the effect of arm number on motor function while maintaining consistent spacing and bare zone length.

In the second approach, the length of the bare zone (L_{bz}) is extended by adding additional segments without arms to the central bare zone of the motor. Here, the number of arms per motor (N_a) remains unchanged, and the spacing between motor arms (L_{sp}) is kept equal to L_{MB} (Fig. 2.3, ii). This configuration enables us to study how variations in bare zone length influence motor interactions with actin filaments.

In the third approach, both the spacing between motor arms (L_{sp}) and the length of the bare zone (L_{bz}) are increased by enlarging the reference length of the backbone segment (L_{MB}). In this case, the number of arms per motor (N_a) is held constant (Fig. 2.3, iii). This strategy facilitates an understanding of how changes in spacing and bare zone dimensions collectively impact motor behavior and

actomyosin contractility.

By systematically varying these structural parameters, we aim to elucidate the specific roles of motor size and configuration in the mechanics of disorganized actomyosin networks and bundles.

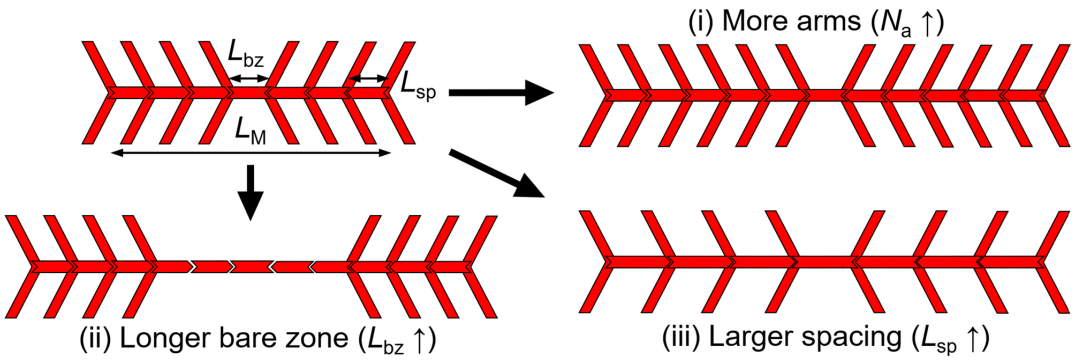

Figure 2.3: Variations in motor structures. A variation in the motor structure in three different ways: (i) increasing the number of motor arms (N_a), (ii) increasing the bare zone length (L_{bz}), and (iii) increasing the spacing between motor arms (L_{sp}).

2.3 Force measurement

To measure the tensile forces generated in the two-filament and bundle simulations, we adopt the following procedure. First, all cylindrical segments crossing the computational domain's cross-sections, positioned at 200 nm intervals along the z-axis, are identified. These segments can belong to F-actin, motor arms, motor backbones, or ACP arms. The z-components of spring forces acting on these segments are then summed. This process results in four distinct force curves as a function of the z position, representing the contributions of different segment types to tensile loads at each cross-section.

Notably, at equilibrium, the total sum of these four forces remains nearly constant across all z positions, indicating that a significant portion of the forces generated by motors are spring forces rather than bending forces. The average of these summed forces across all cross-sections at steady state is

defined as the total tensile force acting on the system, denoted as F_{tot}.

For network simulations, tensile forces are measured using a similar approach. In this case, 20 evenly spaced cross-sections are established along both the x and y directions within the computational domain. The x- or y-components of tensile forces acting on all segments crossing each cross-section are summed at steady state. The average of these summed forces across the 40 total cross-sections is used to determine F_{tot}. This systematic measurement approach provides insights into the distribution and magnitude of tensile forces within various actomyosin configurations.

2.4 The distribution of motors and ACPs plays a key role in force generation

A previous in vitro study observed that the tension generated in thin actomyosin bundles was almost directly proportional to the number of myosin heads per motor, rather than the number of motors [167]. This finding was interesting because their experimental setup did not include actin cross-linking proteins (ACPs). The theoretical framework they proposed was based on the assumption that these bundles consist of serially connected contractile units, similar to sarcomeres in muscle cells [167]. However, they acknowledged that these contractile units lack direct structural analogs within the disordered actomyosin bundles they investigated.

To verify their hypothesis, we first used a simple minimal model composed of two anti-parallel F-actins, two motors, and 16 ACPs (Figs. 2.1B and 2.4). The number of arms per motor was set to N_a = 24. We ran 20 simulations with random z positions of motors and ACPs and found that the total force generated by the system, F_{tot}, fell into the following range (Fig. 2.4A):

$$0.5F_M^{max} \leq F_{tot} \leq F_M^{max} \tag{2.1}$$

where $F_{\mathrm{M}}^{\max}$ is the maximal force that all motors can generate in the system:

$$F_{\mathrm{M}}^{\max} = \frac{1}{2} \sum_{i}^{N_{\mathrm{M}}} F_{\mathrm{M},z}^{i} \tag{2.2}$$

where $F_{\mathrm{M},z}^{i}$ is the z component of spring forces exerted by the ith motor at a steady state, and N_{M} is the number of motors. In this specific example, the number of motors (N_{M}) was set to 2. Notably, only a quarter of the motor arms (N_{a} / 4) were capable of binding to a single F-actin due to two constraints imposed on motor arm binding: first, the motor arms had to align correctly with the polarity of the F-actin; second, two arms connected to the same point on a motor backbone could not bind to the same F-actin. With two antiparallel F-actins, up to half of the motor arms could remain in the bound state. Consequently, the force generated by a motor bound to two antiparallel F-actins at steady state approximated $F_{\mathrm{st}} N_{\mathrm{h}} N_{\mathrm{a}}/2$, where F_{st} represents the stall force of a single myosin head, and N_{h} is the number of myosin heads represented by each motor arm.

We observed that differences in total force (F_{tot}) were influenced by the relative positions of motors and ACPs. When two motors were positioned in nearly identical locations with substantial overlap, F_{tot} approached $F_{\mathrm{M}}^{\max}$. However, when the motors were spatially separated without overlapping, F_{tot} varied depending on the presence of ACPs between them. Without intervening ACPs, forces generated by the two motors' arms could summate, resulting in larger tensile forces on F-actins (Figs. 2.4B, E). Conversely, when ACPs were situated between the two motors, the forces led to the buckling of F-actin between the ACPs and motor arms on one side, counterbalancing the tension from motor arms on the other side (Figs. 2.4C, F). This situation caused F-actins to experience tension equivalent to the force generated by a single motor.

The presence of ACPs between motors effectively divided the bundle into serially connected contractile units, as proposed by the theoretical framework from earlier studies [167,24]. ACPs directly counterbalanced the significant tension generated by motors, resulting in these ACPs experiencing larger

tensile forces compared to others in the system (Fig. 2.4G). Interestingly, intermediate levels of bundle tension between $0.5F_{\mathrm{M}}^{\mathrm{max}}$ and $F_{\mathrm{M}}^{\mathrm{max}}$ were also observed in some cases (Fig. 2.4A). These instances involved motors with partial overlap and ACPs located within the spatial range spanned by one of the motors. Due to the partial overlap with ACPs, forces generated by the two motors partially summed, producing intermediate tension levels (Fig. 2.4D).

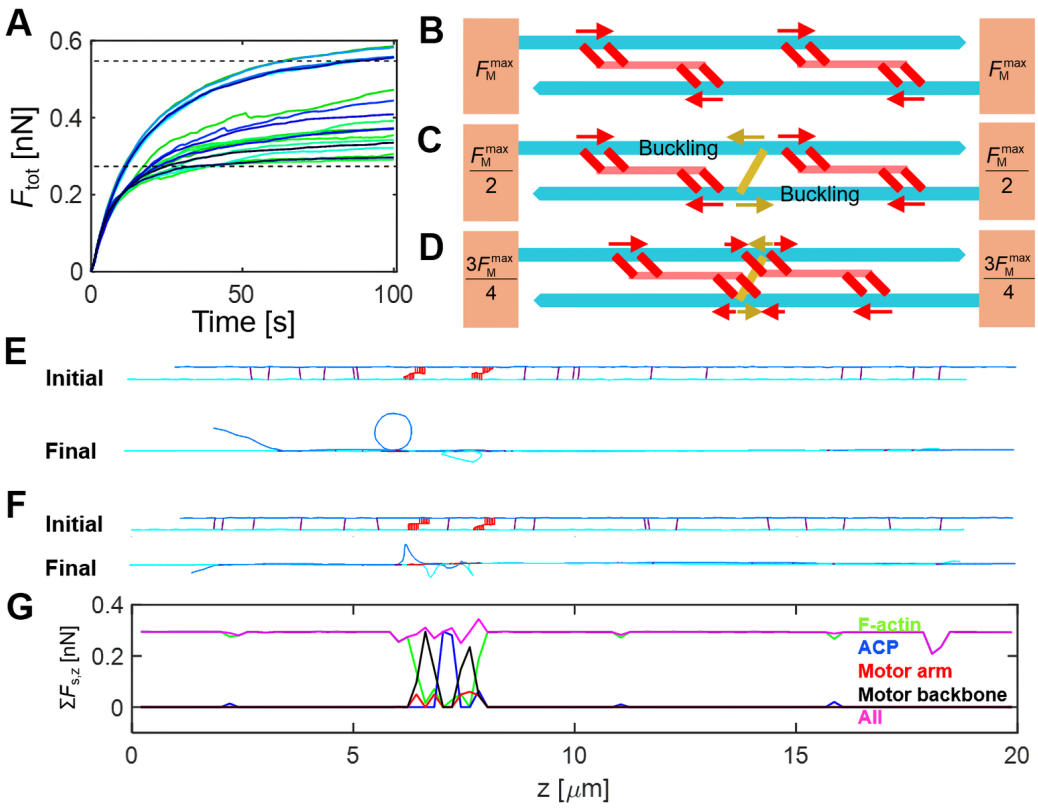

Figure 2.4: Interactions between motors and ACPs. (A) Time evolution of the force generated by two motors in the two-filament system. The upper and lower dashed lines indicate the ideal upper and lower limits of a force that two motors can generate, respectively. (B) Without any ACP between two motors, they can generate a force close to the upper limit which is two-fold larger than a force that one motor can generate ($= F_{\mathrm{M}}^{max}$). (C) With ACP(s) between two motors, ACPs counterbalance a force generated by one of the motors. Thus, they can generate a force close to the lower limit which is equal to the force that one motor can generate ($= F_{\mathrm{M}}^{max}/2$). Part of F-actins is buckled due to two forces with opposite directions. (D) If two motors are close to each other, ACP can counterbalance a fraction of the force generated by one motor. Then, two motors can generate a force between the upper and lower limits. (E, F) Initial and final configurations (E) without or (F) with ACPs between two motors. The vertical dimension is increased 10 times to show the configurations clearly. (G) Measurement of tensile forces acting on F-actins (green), ACPs (blue), motor arms (red), motor backbones (black), or all (magenta) in z direction.

2.5 Force generation in disorganized bundles is also regulated by the same mechanism

To examine the physiological relevance of spatial distributions of motor proteins and actin cross-linking proteins (ACPs) in force generation, we conducted simulations using disorganized actomyosin bundles of varying sizes. The bundle sizes were controlled by adjusting the number of filament allocation positions, N_{F}, which ranged from 2 (corresponding to 8 filaments) to 7 (corresponding to 98 filaments) (Figs. 2.2B and 2.5A). The densities of motors and ACPs were maintained at fixed values of $R_{\mathrm{M}} = 0.005$ and $R_{\mathrm{ACP}} = 0.04$, respectively, ensuring consistent motor and ACP concentrations across simulations. This approach resulted in the total number of motors (N_{M}) varying between 4 and 52 as the bundle thickness increased. For all cases examined, each motor was configured to possess 24 arms ($N_{\mathrm{a}} = 24$), enabling a consistent exploration of the effects of bundle size on force generation.

Simulation results revealed that the total tensile force exerted on the bundles denoted as F_{tot}, increased as the bundle thickness grew with higher N_{F} values (Fig. 2.5B). This increase was attributed to the proportional rise in the number of motors as bundle thickness expanded under a fixed motor density. For the thickest bundle configuration ($N_{\mathrm{F}} = 7$), the actin filament concentration was 12.25 times higher than that in the thinnest bundle ($N_{\mathrm{F}} = 2$). This increase in filament density corresponded to approximately a 13-fold increase in the number of motors, leading to a substantial amplification F_{tot}.

The efficiency of force generation was defined as follows:

$$\eta = \frac{F_{\mathrm{tot}}}{F_{\mathrm{M}}^{\mathrm{max}}} \tag{2.3}$$

For these actomyosin bundles, $F_{\mathrm{M}}^{\mathrm{max}}$ was still defined by Eq.2.2, but $F_{\mathrm{M},z}^{i}$ was close to $F_{\mathrm{st}} N_{\mathrm{h}} N_{\mathrm{a}}$ be-

cause there were more than one F-actin to bind for each polarity. Interestingly, the efficiency factor (η) displayed a notable consistency across simulations involving bundles with N_F=4, 6, and 7 (Fig. 2.5C). In contrast, the bundle with N_F=2 exhibited a significantly higher η compared to the other cases. This observation prompted further investigation into why motors in the thinnest bundle could generate forces in a more efficient manner than those in thicker bundles.

In the case of N_F=2, the bundle contained only four motors. Each motor, equipped with 24 arms, spanned a length of 462 nm, calculated as 42nm×11, where 42 nm represents the spacing between motor arms. Consequently, the combined length of all four motors amounted to approximately 1.848 μm, which is only 9% of the total bundle length of 20 μm. This relatively small proportion of motor length to bundle length significantly reduced the likelihood of substantial overlap between motors. Instead, the motors were spatially distributed with varying distances between them.

Given the high density of actin cross-linking proteins (ACPs) in the system, multiple ACPs were positioned between adjacent motors. This configuration effectively separated the motors into distinct contractile units, preventing their forces from adding constructively. As a result, the total tensile force (F_{tot}) in the thinnest bundle was approximately equivalent to the force generated by a single motor. This led to η being inversely proportional to the number of motors (N_M) in the bundle. In the case of N_F=2, where N_M=4, η was approximately $1/N_M$, or 0.25, corroborating this rationale.

If motors behaved similarly in thicker bundles (N_F>2), η would be expected to decrease further, as N_M increases in proportion to N_F^2 due to the fixed motor density. Indeed, η in thicker bundles was observed to be smaller than 0.25, aligning with this expectation. However, a closer examination revealed that η remained relatively consistent at around 0.12 across all bundles with N_F>2, which was notably larger than the theoretical prediction of $1/N_M$.

This discrepancy can be attributed to the higher likelihood of motor overlap and proximity in thicker bundles. As N_F increased, the number of motors (N_M) rose proportionally, leading to a greater probability of motors being positioned close to or overlapping with one another. In cases

where neighboring motors were not separated by ACPs, their forces could partially add constructively, a phenomenon previously described as cooperative motor behavior. Such cooperative interactions contributed to a F_{tot} that exceeds the maximal force generated by a single motor. Importantly, F_{tot} in these thicker bundles was determined by the largest force generated by any individual contractile unit, which could include multiple cooperative motors.

As N_{M} increased with higher N_{F}, the number of cooperative motors within the bundle also tended to rise. This led to an overall increase in both F_{tot} and $F_{\text{M}}^{\text{max}}$, resulting in a value of η that was higher than $1/N_{\text{M}}$ and relatively insensitive to further increases in N_{F} when N_{F} was not small. This finding underscores the role of motor spatial distribution and cooperative behavior in shaping the mechanical efficiency of actomyosin bundles as their size and motor density increase.

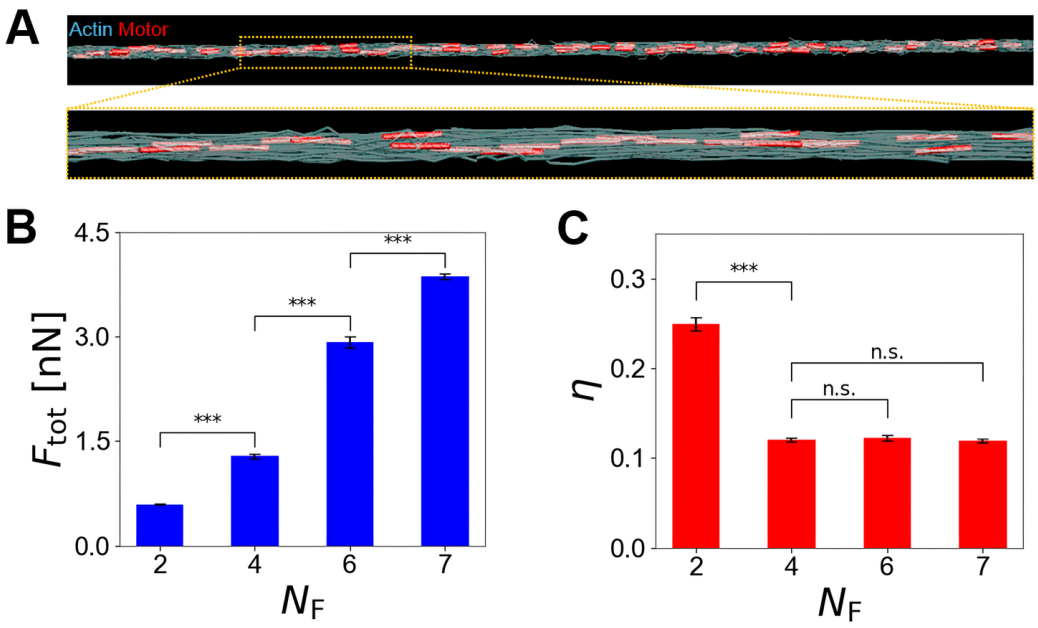

Figure 2.5: Thicker bundles generate larger force but less efficient. (A) An example of disorganized bundles with $N_{\text{F}} = 7$ visualized at the beginning of the simulation, where N_{F} is a parameter defining bundle thickness. F-actins are visualized as transparent elements to show the positions of motors. (B) Bundle-level force and (C) the efficiency of force generation measured at a steady state with different N_{F}. In thicker bundles ($N_{\text{F}} > 2$), larger forces were generated, but the efficiency was lower than that in the thinnest bundle ($N_{\text{F}} = 2$). *** represents $p \leq 0.001$, and n.s. represents $p > 0.05$.

2.6 Bundles with more, localized motors generate larger forces

Previous observations have demonstrated that the degree of overlap between motor proteins significantly influences the force-generation process in the actomyosin bundles. When the bundle length is fixed, the extent of motor overlaps is primarily determined by the number of motors (N_{M}) available within the system. To systematically investigate how N_{M} influences force generation in bundles, we conducted a series of computational simulations across a wide range of N_{M} values. These simulations utilized the thickest bundle configuration ($N_{\mathrm{F}} = 7$) while maintaining a constant ratio of active cross-bridge probability ($R_{\mathrm{ACP}} = 0.04$) and a fixed number of actin filaments ($N_{\mathrm{a}} = 24$).

The total bundle tension displayed a clear increasing trend with the rising N_{M}. In contrast, the contractile efficiency exhibited an inverse relationship with N_{M} (Fig. 2.7A). For bundles with a low N_{M}, the total tension, was relatively insensitive to incremental increases in N_{M}. This behavior is attributed to the limited ability of additional motors to align in positions that effectively add up the forces produced by other motors within the bundle. Instead, the addition of motors primarily increased the total number of contractile units. However, many of these units contained only a single motor, leading to diminished contributions to the overall tension. Consequently, as described by Eq. 2.3, η was observed to approach $1/N_{\mathrm{M}}$ in simulations with low N_{M} values.

In contrast, at higher N_{M} values, F_{tot} became more sensitive to changes in N_{M}. This enhanced sensitivity arises because an increase in N_{M} contributes to a greater number of motors per contractile unit, thereby enhancing the force generation. When N_{M} reached sufficiently high levels, F_{tot} approached direct proportionality with N_{M}, with a slope near unity. Under these conditions, most of the bundle space was already occupied by motors, and the addition of more motors led to a substantial and proportional increase in the magnitude of F_{tot}.

Interestingly, the sensitivity of η to changes in N_{M} was markedly reduced at high N_{M} values. For instance, when N_{M} was increased from 10 to 1000, η decreased by only about half. This relative in-

sensitivity can be attributed to concurrent increases in both F_{tot} and the number of contractile units at elevated N_{M} levels. As a result, the efficiency loss associated with increasing N_{M} was mitigated by the corresponding enhancement in bundle force generation, as previously described. These findings highlight the important interplay between motor quantity, spatial distribution, and overall contractile performance in the actomyosin bundles.

To verify this rationale, we developed a way to estimate the maximum number of overlapping motors, Ξ, using our simulation data:

$$\Xi = \max_{\substack{i=1\ldots N_{\text{M}} \\ j=L \text{ or } R}} \left(1 + \sum_{\substack{k=1 \\ k\neq i}}^{N_{\text{M}}} \xi_{ik}^{j} \right) \tag{2.4}$$

where ξ_{ik}^{j} is:

$$\xi_{ik}^{j} = \begin{cases} 1 & \text{if } L_{\text{c}} \leq L_{\text{ov}} \leq L_{\text{M}}, \\ \frac{L_{\text{ov}}}{L_{\text{c}}} & \text{if } 0 < L_{\text{ov}} < L_{\text{c}}, \\ 0 & \text{if } L_{\text{ov}} = 0. \end{cases} \tag{2.5}$$

i and k are the indices of motors, j denotes the left or right side of a motor, and L_{ov} is an overlap distance between two motors. In addition, L_{c} is the critical length required for the cooperative overlap:

$$L_{\text{c}} = 2L_{\text{sp}} \left(\frac{N_{\text{a}}}{4} - 1 \right) \tag{2.6}$$

L_{c} is two-fold greater than the length occupied by motor arms on one side of a motor backbone. Two motors are considered a cooperative motor pair if L_{ov} is equal to or greater than L_{c} (Fig. 2.6). With this cooperative overlap, ACPs cannot counterbalance forces exerted by motor arms. If L_{ov} is shorter than L_{c} and but greater than zero, two motors are considered as a partially cooperative motor pair.

By comparing all the motor combinations, Ξ can be obtained. Ξ can range between 1 (no overlap between motors) and N_M (cooperative overlap between all motors). Using this Ξ, a force acting on the bundle can be estimated as F_{est}:

$$F_{est} = \frac{F_{st} N_h N_a \Xi}{2} \tag{2.7}$$

The sensitivity of F_{est} to an increase of N_M is high at large N_M with a slope close to 1 (Fig. 2.7B), which is consistent with our rationale described earlier. F_{est} was generally smaller than F_{tot} because this analysis does not account for actual bundle geometry consisting of multiple F-actins; if two motors are located far from each other in x or y direction, they may not counterbalance or add up forces. Nevertheless, we found that F_{est} captures the overall dependence of F_{tot} on parameters well.

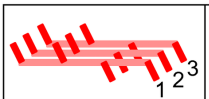		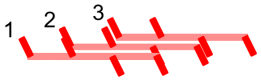	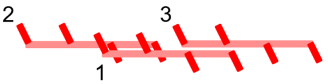
$\xi_{12}^{L}=1,\ \xi_{12}^{R}=1$	$\xi_{12}^{L}=1,\ \xi_{12}^{R}=1$	$\xi_{12}^{L}=1,\ \xi_{12}^{R}=1$	$\xi_{12}^{L}=L_{ov}/L_c,\ \xi_{12}^{R}=0$
$\xi_{13}^{L}=1,\ \xi_{13}^{R}=1$	$\xi_{13}^{L}=1,\ \xi_{13}^{R}=1$	$\xi_{13}^{L}=0,\ \xi_{13}^{R}=L_{ov}/L_c$	$\xi_{13}^{L}=0,\ \xi_{13}^{R}=L_{ov}/L_c$
$\xi_{23}^{L}=1,\ \xi_{23}^{R}=1$	$\xi_{23}^{L}=1,\ \xi_{23}^{R}=1$	$\xi_{23}^{L}=1,\ \xi_{23}^{R}=1$	$\xi_{23}^{L}=0,\ \xi_{23}^{R}=0$
$\Xi=3$	$\Xi=3$	$\Xi=3$	$\Xi=1+\max(\xi_{12}^{L},\ \xi_{13}^{R})$

Figure 2.6: Examples of calculating the maximal number of cooperatively overlapping motors. ξ indicates the extent of an overlap between two motors, and it is defined on the left (L) and right (R) sides of each motor. If two motors have a fully cooperative overlap, ξ is 1 on both sides of the two motors. If there is no overlap at all, ξ is 0 on both sides of the two motors. If two motors have a partially cooperative overlap, ξ is greater than 0 only on one side of the two motors, L_{ov}/L_c, where L_{ov} is an overlap distance between two motors, and L_c is the critical length required for the fully cooperative overlap. Ξ is the maximal number of cooperatively overlapping motors obtained by comparing all the combinations of motors in the system. Four examples are provided here for a better understanding of this analysis method.

In the preceding analysis, we assumed that motors could be randomly distributed across any region within the bundle. However, if motors are confined to a smaller, more localized region, the degree of overlap between motors (Ξ) can be significantly increased for the same N_M, thereby enhancing

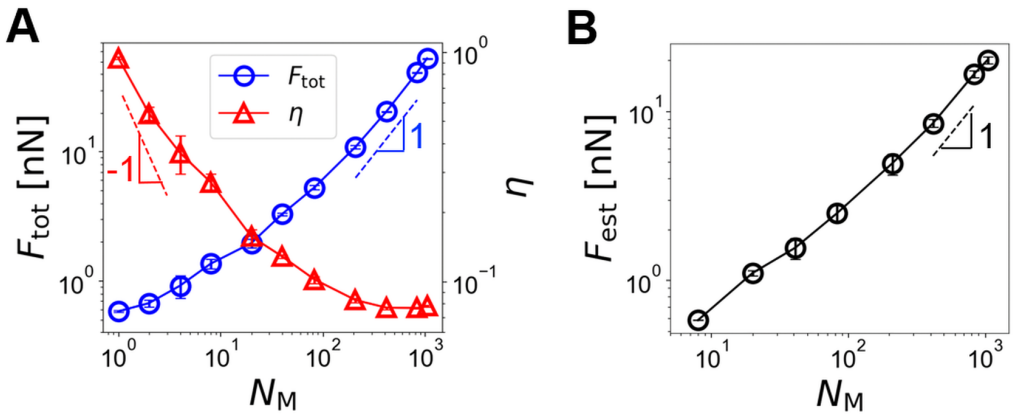

Figure 2.7: Effects of the motor number in disorganized bundles. The thickest bundle ($N_F = 7$) was used for all cases. (A) Bundle-level force (blue circles) and the efficiency of force generation (red triangles) with a wide range of N_M. With more motors, a larger force (F_{tot}) was generated, but the efficiency (η) was lower. (B) Prediction of a force using the positions of motors. To find the estimated force (F_{est}), Ξ is calculated first, and Eq.2.7 is used.

the force generation capability of the bundle. To systematically examine the effects of motor spatial distribution on force generation, we conducted simulations using a fixed set of parameters: $N_F = 7$, $R_{ACP} = 0.04$, $N_M = 52$, and $N_a = 24$. In these simulations, motors were constrained to occupy a specific portion of the bundle, defined by a fraction f, which varied between 0 and 1. Here, $f = 1$ represents the condition where motors are randomly distributed throughout the entire length of the bundle. The center of the region allocated for motor distribution was aligned with the center of the bundle.

The results indicated that the bundle produced the highest total tension (F_{tot}) and achieved the maximum contractile efficiency (η) when motors were localized near the center of the bundle, specifically at $f = 0.06$ (Fig. 2.8A). It is important to note that the term F_M^{max} in the denominator of Eq.2.3 remains constant across these scenarios, meaning that F_{tot} is directly proportional to η. When motors are concentrated in a relatively small, central region, they are more likely to overlap in a cooperative manner, satisfying the condition $L_c \leq L_{ov} \leq L_M$. This facilitates the formation of strong contractile units, allowing a large fraction of the motors to effectively contribute to force generation.

As the value of f increased, motors became more evenly distributed across the bundle, resulting in a sparser arrangement. In these cases, many motors exhibited only partial overlap or were entirely separated from one another. This spatial separation diminished the ability of motors to cooperate and align synergistically, leading to a decrease in both F_{tot} and η (Fig. 2.8A). Furthermore, the observed effects of f on force generation were consistent with predictions made by the theoretical model described earlier, confirming the validity of the model in reproducing the influence of motor distribution on bundle mechanics (Fig. 2.8B).

These findings underscore the critical role of motor spatial localization in optimizing the force-generating capacity of bundles. By concentrating motors in specific regions, particularly near the center of the bundle, the cooperative interactions between motors are maximized, enhancing both the total force generated and the efficiency of the contractile mechanism.

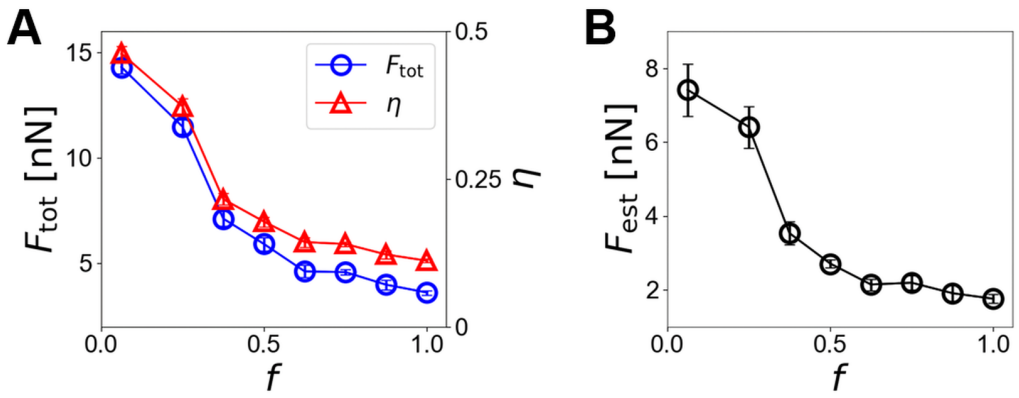

Figure 2.8: Motor distribution affects the force generation in disorganized bundles. We varied the relative size of a region where motors were initially located, f. $f = 1$ means that motors can be located at any part of the bundle. (A) Bundle-level force (F_{tot}) and efficiency (η) depending on f. As motors were localized more closely to the center (i.e., smaller f), the force and the efficiency were higher. (B) Prediction of the bundle-level force with different f.

2.7 The structure of motors influences force generation in bundles

We employed motors with 24 arms, each having a length of $L_M = 462$ nm, along with a bare zone length $L_{bz} = 42$ nm and a spacing between arms $L_{sp} = 42$ nm. As mentioned earlier, the structural characteristics of myosin thick filaments can vary significantly depending on the myosin isoform and experimental conditions. If motors are longer and possess more arms, they may generate greater bundle forces. To verify this hypothesis, we examined cases with varying N_a while maintaining the thickest bundle configuration ($N_F = 7$) and keeping the total number of arms in the system, $N_a N_M$, constant. With higher N_a, L_M increased, but N_M decreased (Fig. 2.3, i). When L_M increased due to higher N_a, F_{tot} also increased (Fig. 2.9A, red). Because these cases had the same total number of motor arms, F_M^{max} in Eq.2.3 was identical across all simulations. Consequently, η exhibited the same trend as F_{tot} (Fig. 2.9B); with longer motors, η was higher. A similar trend was observed for F_{est} (Fig. 2.9B, red). Longer motors with more arms enhance the strength of individual contractile units, leading to F_{tot} and η being directly proportional to L_M if there is no overlap between motors. However, these motors are less likely to overlap in a fully cooperative manner due to the larger L_c (Eqs. 2.5 and 2.6). Thus, Ξ was actually smaller with higher L_M (Fig. 2.9C, red). This explains why the dependence of F_{tot} on L_M was weaker at high L_M compared to low L_M (Fig. 2.9A).

There are two additional approaches to increase L_M without altering N_a and N_M: (1) increasing L_{bz} at the center of motors or (2) uniformly increasing L_{sp} between motor arms (Fig. 2.3, ii and iii). We performed simulations to investigate variations in either L_{sp} or L_{bz} using the thickest bundle ($N_F = 7$) with $N_a = 16$. These results were compared to simulations where N_a varied as described earlier. Interestingly, when L_M was similar, the F_{tot} obtained by changing L_{bz} closely matched that from varying N_a, despite differences in N_M (Fig. 2.9A, blue). In contrast, F_{tot} in cases with altered L_{sp} was notice-

ably lower (Fig. 2.9A, green). η followed the same trend as F_{tot} since F_M^{max} was identical in all cases (Fig. 2.9B). F_{est} also reproduced a similar pattern (Fig. 2.9D). For a fixed L_M, a longer bare zone positions motor arms closer to the two ends of the motor backbone. This increases the likelihood of force addition due to a smaller L_c (Eqs. 2.5 and 2.6). Consequently, Ξ was higher (Fig. 2.9C, blue), leading to increased F_{tot} and η despite a smaller N_a. Conversely, motors with uniformly larger spacings between arms require greater overlap to sum forces. The smaller Ξ and N_a resulted in lower F_{est} and η (Figs. 2.9C and D, green).

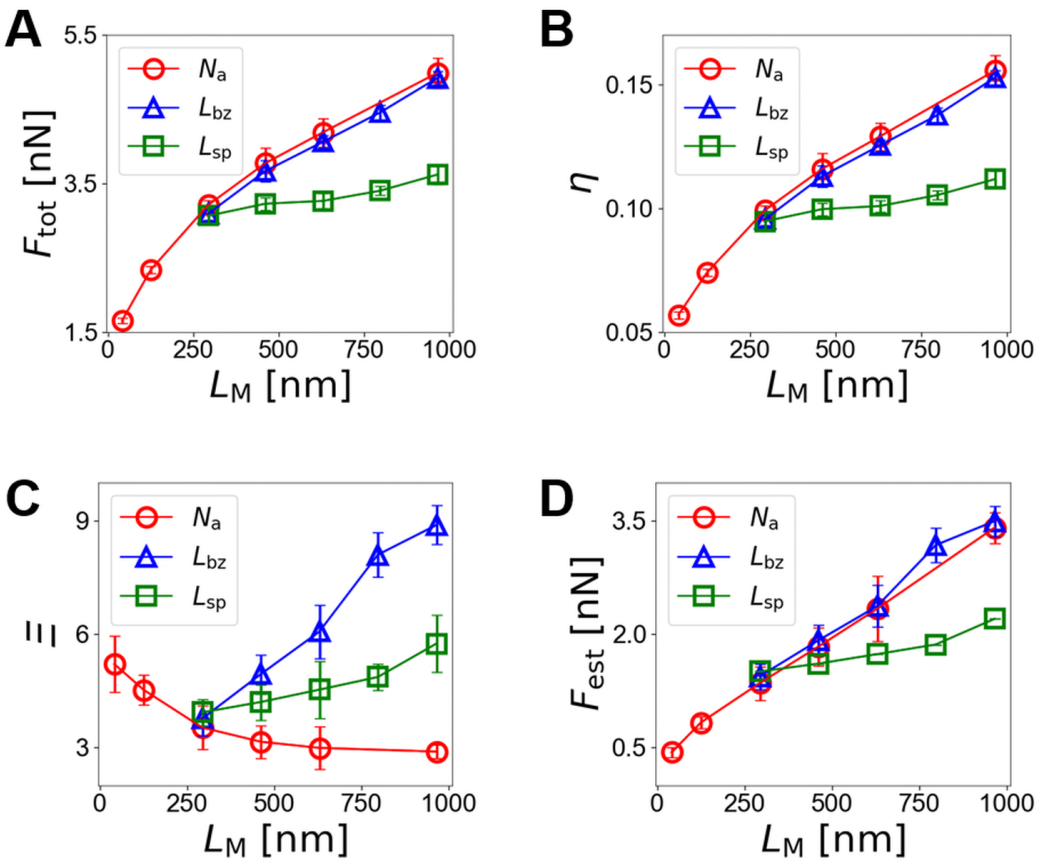

Figure 2.9: Motor architectures impact the force generation in disorganized bundles. (A) Bundle-level force (F_{tot}) depending on L_M. The motor length (L_M) is varied by changing either the number of motor arms (N_a, red circles), the bare zone length (L_{bz}, blue triangles), or the spacing between motor arms (L_{sp}, green squares). (B) The efficiency of force generation. (C) The maximum number of cooperatively overlapping motors. (D) Prediction of the bundle-level force using the positions of motors.

2.8 Force generation in actin networks is regulated by the same mechanism

To examine the generality of our findings, we conducted simulations using a two-dimensional network where F-actins and motors were randomly oriented without any directional bias, in contrast to the highly ordered structures found in filament bundles (Fig. 2.2A). In this 2D network, we systematically varied one parameter at a time, including the number of motors (N_M), the number of actin filaments (N_a), the bare zone length (L_{bz}), or the spacing between motor arms (L_{sp}), similar to the approach taken for bundle simulations (Fig. 2.10).

The total force generated by the 2D network (F_{tot}) was consistently smaller than the corresponding values measured in bundles under the same conditions. This reduction in force can be attributed to the random orientations of motors and actin filaments in the network, which limit the alignment of forces along a single direction (Figs. 2.11A, B). Interestingly, our results revealed that F_{tot} in the 2D network was proportional to $N_M^{0.65}$, which is close to $\sqrt{N_M}$. In the case of bundles, F_{tot} was directly proportional to N_M at large N_M (Fig. 2.7A). The weaker dependence of F_{tot} on N_M in the 2D network is consistent with expectations, given that motors are uniformly distributed and their orientations are random in this system.

The contractile efficiency (η) observed in the 2D network exhibited similar magnitudes to those measured in filament bundles under comparable conditions (Figs. 2.9D, B, and 2.11C). Notably, η was still calculated using Eq.2.3, but the effective F_M^{max} in the 2D network was determined by summing the x- or y-components of the forces exerted by all motors and then averaging them across the system:

$$F_M^{max} = \frac{1}{N_M} \sum_{i=1}^{N_M} \sqrt{F_{i,x}^2 + F_{i,y}^2}. \tag{2.8}$$

The dependences of F_{tot} and η on the examined parameters in the 2D network closely resembled those observed in filament bundles. This suggests that the fundamental mechanism of force generation, regulated by cooperative overlaps between motors, operates similarly in networks as it does in bundles. Although the forces exerted by motors in the network are not aligned along a common axis, they can still counterbalance or sum effectively depending on the relative positions and orientations of the motors. This behavior highlights the robustness of the cooperative mechanism of force generation across different structural organizations, from bundles to 2D networks.

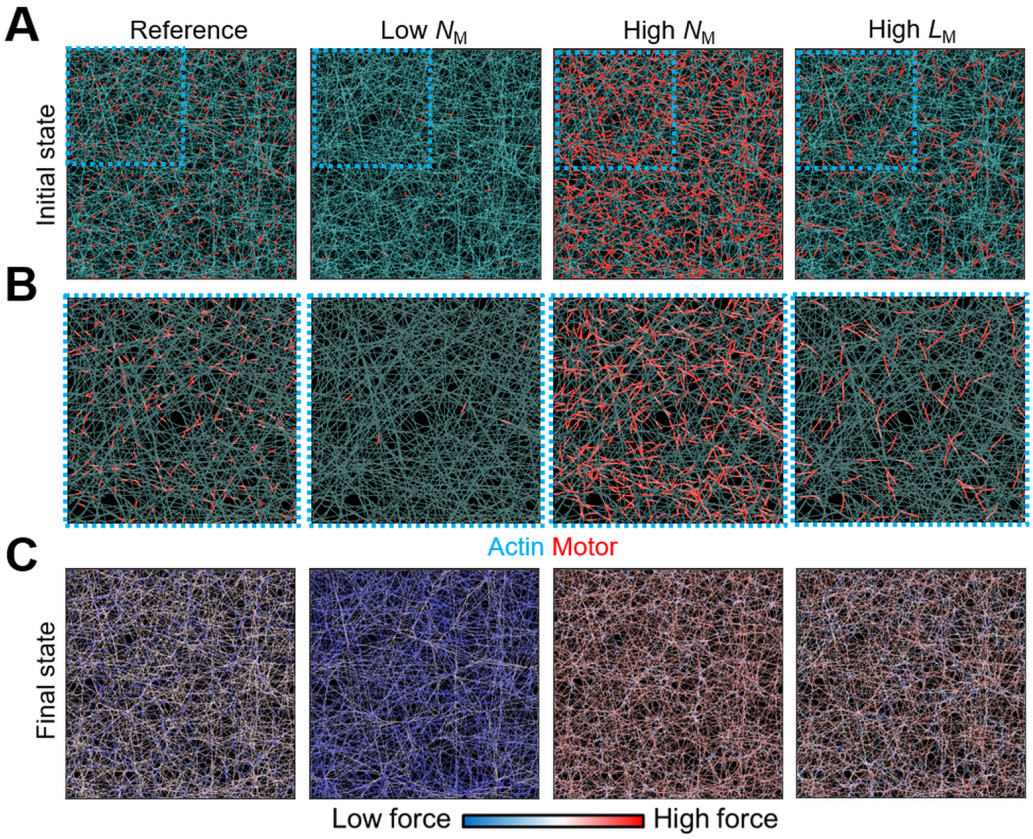

Figure 2.10: Configurations of the two-dimensional actomyosin network. (A) Examples of networks at the initial state under the reference condition, with a smaller or larger number of motors, and with longer motors. (B) Snapshots show only a quarter of networks in (A) to better visualize individual motors. (C) Examples of networks at the final state showing the local tension in blue for low force and red for high force.

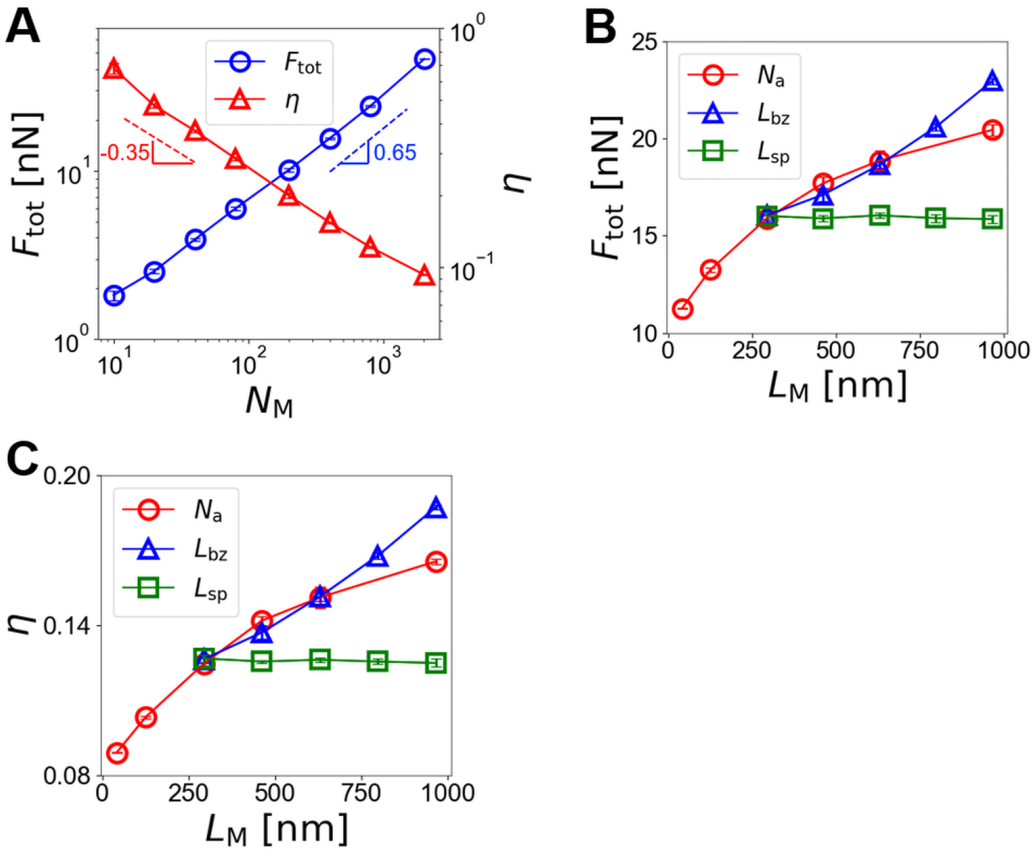

Figure 2.11: Force generation in the two-dimensional actomyosin networks. (A) Network-level tension (F_{tot}) and the efficiency of force generation (η) with a different number of motors. (B) F_{tot} depending on motor length varied by changing either of the number of motor arms (N_{a}, red circles), the bare zone length (L_{bz}, blue triangles), or the spacing between motor arms (L_{sp}, green squares). (C) The efficiency of force generation in two-dimensional actomyosin networks with different motor lengths varied by three methods.

Art is such an action. It is a kindred form of action to idealism. They are both expressions of the same drive, and the man who fails to fulfill this urge in one form or another is as guilty of escapism as the one who fails to occupy himself with the satisfaction of bodily needs.

Mark Rothko, *The Artist's Reality: Philosophies of Art*

3

Discussion of the Myosin II Thick Filament Structural Impacts

Actomyosin contractility represents a highly conserved molecular machinery critical for generating mechanical forces in animal cells. This mechanism plays a pivotal role in a wide range of physiological processes, including cytokinesis, cell migration, and tissue morphogenesis[125]. Central to

this process is myosin II, the primary molecular motor responsible for force generation within cells. Myosin II exists in the form of highly organized structures known as thick filaments. Over the past decades, the structural and functional characteristics of myosin thick filaments have been extensively studied. Despite the diversity in thick filament forms observed across different cell types, the specific effects of their structural properties on force generation remain poorly understood.

3.1 Optimized distribution of contractile units

An earlier *in vitro* study investigated the effects of myosin II filament size on force generation using disorganized actomyosin bundles composed of a few F-actins and three myosin isoforms: skeletal muscle myosin, smooth muscle myosin, and non-muscle myosin [167]. The findings revealed that the tensile force generated in these bundles was directly proportional to the number of myosin heads per filament, provided that the total number of myosin heads was constant. This proportionality was explained through a theoretical bundle model consisting of serially connected contractile units, where each myosin II filament served as a unit of force generation. While this explanation aligns partially with the observations in our study, it applies primarily to bundles with minimal overlap between thick filaments, where only a few thick filaments are present.

Although actomyosin contractility has been the subject of several theoretical and computational studies, most prior models adopted highly simplified representations of molecular motors, neglecting the structural intricacies of thick filaments [17,40,34]. Consequently, these models were unable to capture the influence of thick filament properties on force generation. A limited number of models have considered thick filament structures; however, these models were often restricted to simulating a single filament due to computational constraints [161,183], or they did not probe the detailed force generation process [22].

In this study, we employed motors with the geometry of bipolar thick filaments to systematically

investigate how force generation in disorganized actomyosin structures, including bundles and networks, is regulated by the number, spatial distribution, and structural properties of motors. First, using a minimal system comprising only two F-actins, we demonstrated that motors positioned between actin filaments with anti-cooperative positioning (ACPs) could not combine their forces to produce a larger net force (Fig. 2.4). We then examined disorganized bundles of varying thickness and observed that while the bundle-level force (F_{tot}) increased with thickness, the efficiency of force generation (η) decreased (Fig. 3). This reduction in efficiency was attributed to the larger number of motors in thicker bundles.

Our simulations further revealed that bundles with more motors generated higher forces but did so less efficiently (Fig. 3.1). When motors were distributed sparsely, with minimal overlap, the efficiency of force generation was inversely proportional to the number of motors ($\eta \sim 1/N_{\text{M}}$). However, as the number of motors increased, cooperative overlaps between motors became more frequent, leading to the formation of stronger contractile units and an efficiency greater than $1/N_{\text{M}}$. Additionally, we examined the effects of motor distribution and found that force generation was significantly enhanced when motors were confined to a smaller region, as this promoted cooperative overlaps among densely packed motors (Fig. 3.2).

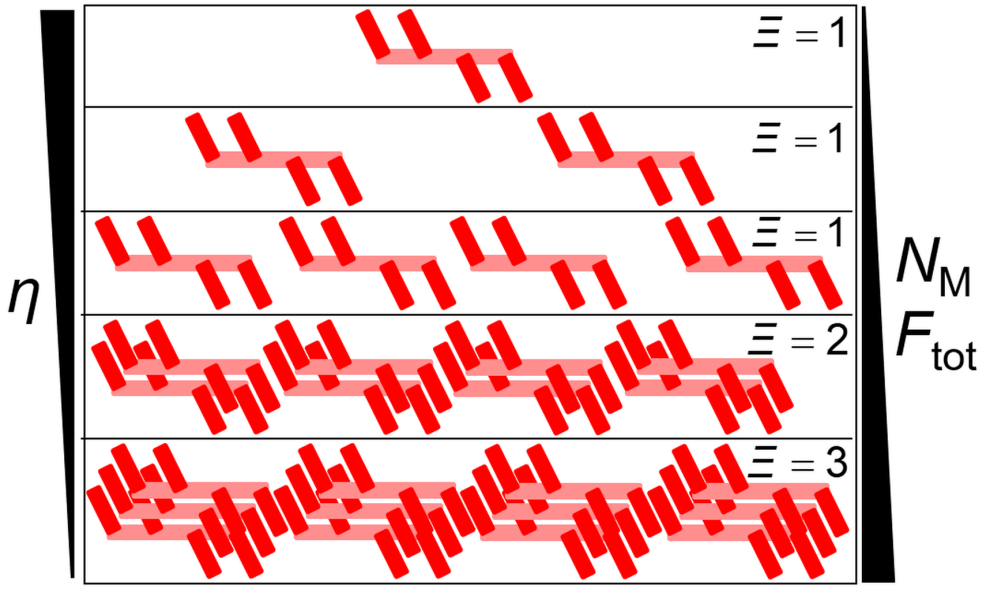

Figure 3.1: Configuration of bundles with different motor numbers. Ξ represents the estimated number of motors in the strongest contractile unit. With small N_{M}, F_{tot} and Ξ are unlikely to increase significantly until an entire bundle is occupied by motors, so η is roughly $1/N_{\mathrm{M}}$. By contrast, with high NM, an increase N_{M} directly enhances F_{tot} and Ξ, and η almost remains constant.

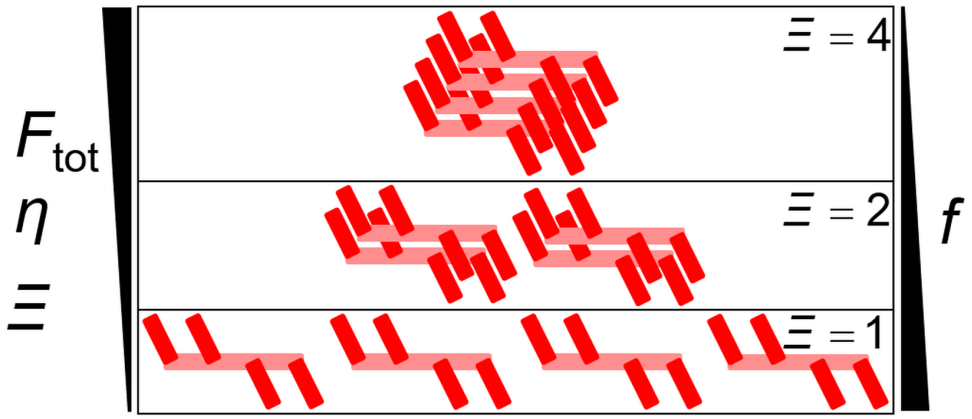

Figure 3.2: Configuration of motors with different motor distribution levels. Ξ indicates the estimated number of motors in the strongest contractile unit. f denotes the distribution level of motors, which increases with an increase of motor distribution area in the bundle. Given the number of motors, smaller f results in more cooperative overlaps (i.e., higher Ξ) and thus leads to higher F_{tot} and η.

3.2 Optimized motor structures depending on the cell types

We also explored how motor length and arm configuration affected force generation. Motors with longer lengths and more arms generated greater forces because the forces produced by the arms of a single motor could simply add up (Fig. 3.3). Interestingly, longer motors with an extended bare zone and fewer arms outperformed motors with shorter bare zones and wider arm spacing (Fig. 3.4). This is because the former required a smaller degree of overlap to achieve cooperative interactions, resulting in higher forces. Our findings underscore the importance of considering thick filament structural properties in force generation, challenging the conclusions of recent studies that focused solely on F-actin connectivity [34].

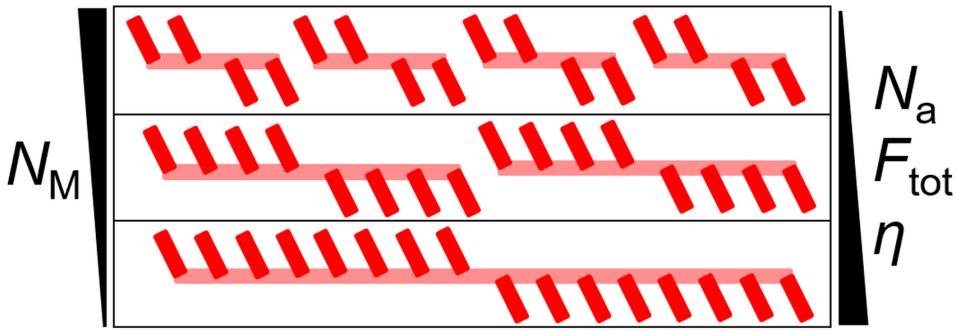

Figure 3.3: Configuration of bundles with longer motors incorporating more arms. As each motor has more arms (N_a), F_{tot} and the efficiency of force generation (η) become higher because forces generated by motor arms are counterbalanced to a lesser extent.

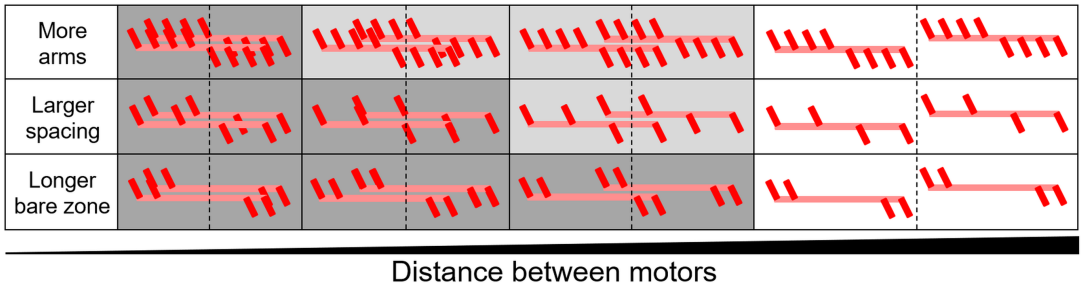

Figure 3.4: Possible overlaps between two motors with different structures. A dark gray color indicates a fully cooperative overlap, and light gray indicates a partially cooperative overlap. To have the fully cooperative overlap, motors with many arms need to located very closely, whereas motors with the long bare zone can overlap in the fully cooperative manner with a relatively long distance between them. This is because the latter requires a smaller degree of overlap to achieve cooperative interactions, resulting in higher forces.

3.3 Further implications for disorganized actomyosin bundles in non-muscle cells

Our results have broader implications for understanding the structural organization of stress fibers in non-muscle cells, which mediate various physiological processes such as cell protrusion, cytokinesis, and cell shape maintenance[27,78]. In stress fibers, non-muscle myosin II is the principal motor driving contractile forces. Stress fibers can be categorized into two main types: ventral stress fibers and transverse arcs[93]. Ventral stress fibers, which are derived from pre-existing precursors, possess sarcomere-like structures with serially connected contractile units separated by α-actinin, a type of ACP. In contrast, transverse arcs lack distinct repeating structures and contain fewer ACPs. In ventral stress fibers, the abundance of ACPs counterbalances motor-generated forces, as demonstrated in Fig. 2.4. This structural organization limits force amplification beyond what is generated by a single contractile unit. Consequently, ventral stress fibers are expected to produce smaller forces than transverse arcs of similar thickness. However, since ventral stress fibers are typically thicker, they generate larger overall tension, consistent with our findings (Fig.2.5)[92].

In addition to force generation, the contractile behavior of actomyosin structures, such as length reduction, has been a focus of interest. Our model can be adapted to study these behaviors by deactivating periodic boundary conditions and disconnecting the bundle or network from fixed domain boundaries, as previously described[96]. For achieving higher contractile speeds with the same total number of myosin heads, multiple contractile units are advantageous, as suggested in prior studies[167]. This highlights a trade-off between force generation and contractile speed. Furthermore, previous studies have shown that contractile speed in actomyosin networks is proportional to motor density[125,193,107]. Our model could be utilized to systematically investigate how contractile speed is regulated by parameters such as motor number, distribution, length, and structural properties.

In this study, we investigated how the process of force generation in disorganized actomyosin bundles and networks is regulated by the structural and spatial properties of myosin thick filaments. Our findings demonstrated that increasing the number of motors enables bundles and networks to generate larger tensile forces. However, this increase in force generation is accompanied by a reduction in the efficiency of force generation (η). Specifically, we observed that the relationship between the number of motors and force generation is non-linear and depends significantly on several key factors.

First, with the same total number of motors, the forces generated by bundles and networks can vary considerably depending on their spatial distribution. Sparse distributions of motors lead to lower cooperative interactions, resulting in less efficient force generation. In contrast, dense motor distributions promote cooperative overlaps, allowing for stronger contractile units and higher forces. Second, the number of myosin heads per thick filament is a critical determinant of the overall force. Thick filaments with more myosin heads can generate larger forces because their heads can exert additive forces when interacting with actin filaments. Finally, the length of the bare zone at the center of the thick filament plays a crucial role. Longer bare zones enable motors to position their arms closer to the ends of the filament, increasing the likelihood of cooperative force addition.

Our findings align partially with prior studies, such as the one conducted research[167], where the

effects of different myosin isoforms under varying conditions were examined. These results can also be further validated experimentally using synthetic myosin thick filaments. For instance, synthetic thick filaments constructed using advanced methods such as DNA origami[42] provide a unique platform to test our predictions. These artificially designed structures allow precise control over filament dimensions, motor head numbers, and bare zone lengths, enabling systematic verification of the role these factors play in force generation.

Our study highlights the intricate interplay between motor quantity, distribution, and structural properties in regulating actomyosin contractility, offering new insights into the fundamental mechanisms of force generation in cellular and synthetic systems.

Then this ebony bird beguiling my sad fancy into smiling,
By the grave and stern decorum of the countenance it wore,
"Through thy crest be shorn and shaven, thou", I said,
"art sure no craven,
Ghastly grim and ancient Raven
wandering from the Nightly shore-
Tell me what thy lordly name is
on the Night's Plutonian shore!"
Quoth the Raven "Nevermore."

Edgar Allan Poe, *The Raven*

4

Elucidating the Mechanical Adaptation of Actomyosin Bundles

Mechanical forces play an essential role in cellular processes including cell morphogenesis, migration, and cytokinesis[93,150,19,191]. Among these processes, how cells respond to external force and generate contractile force is intimately associated with biological functions and diseases, such as

wound healing and cancer[84,91]. However, depending on the cell type and the related function, distinct mechanical environments exist. These mechanical conditions and their alteration affect cellular processes profoundly. Diverse responses of cells under these changing mechanical conditions still require elucidation. Therefore, to comprehend the cell dynamics, cellular functions in force generation and mechanotransduction need to be explored systematically. As the origin of force generation, actin-myosin interactions play vital functions in such adaptive behaviors. Although their basic mechanisms are similar in different types of muscle cells as introduced in the previous chapters, their architectures among the striated muscle, smooth muscle, and non-muscle cells demonstrate significant differences. By associating with other protein complexes, striated muscles present a highly organized actomyosin structure, whereas the smooth muscle and non-muscle cells show relatively disordered configurations. In this chapter, we first summarize the current knowledge related to actomyosin structures among different cell types. Following that, we focus on how the actin-myosin interactions contribute to the mechanical adaptation in non-muscle cells, which is still unclear to date. An in vitro single-fiber experiment was conducted to show the dynamic properties of the actomyosin bundle. The observations were investigated quantitatively by associating with our agent-based model.

4.1 The in vitro single-fiber experiment

To isolate individual SFs, we first remove the apical cell membrane, cytosol, and nucleus in the A7r5 cells via the hypotonic shock technique[118]. The ventral SFs could remain attached to an underlying substrate by treating the de-roofed cells with a detergent. The contractility of these extracted SFs was maintained with the magnesium-ATP buffer at a physiological level that reactivated myosin ATPase. The isolated SF was further manipulated by a functionalized glass needle, which can stick on one end of the fiber and apply the external forces (Fig. 4.1A). Regarding the measurement of the bundle force, a specialized device has been developed with a pair of the glass needle, which is available to manipulate

individual SFs and detect their contractile forces. In this equipment, one of the needles is movable by associating with the piezo-actuator, whereas the other needle is fixed for stabilizing the bundle. An optical system is embedded as well, allowing the observation of the fluorescence image during the experiment (Fig. 4.1B).

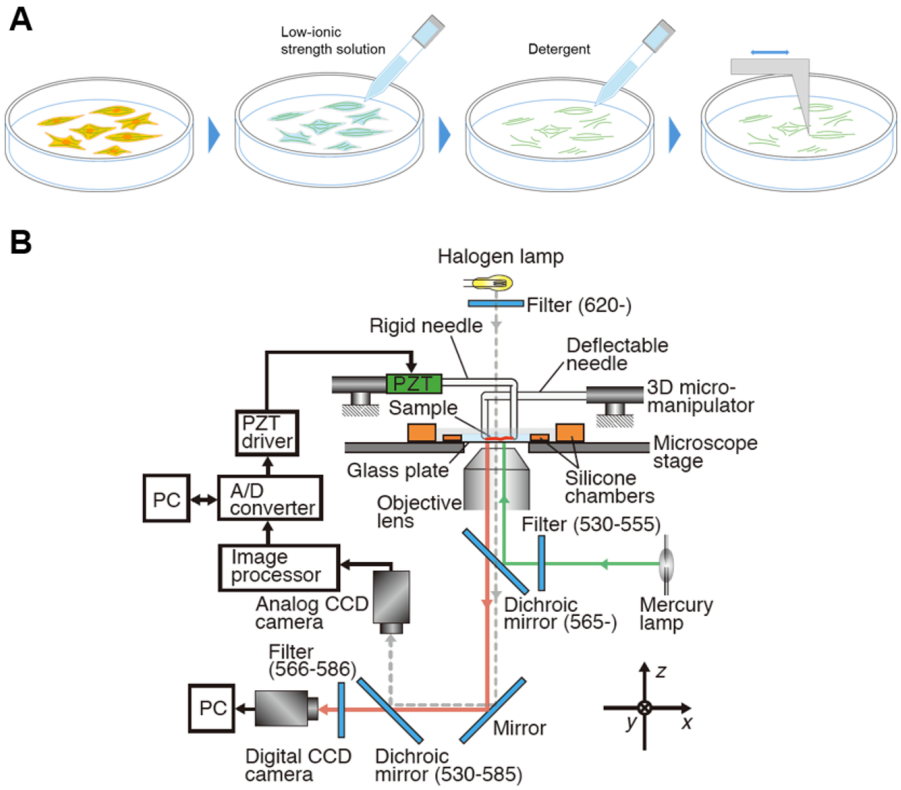

Figure 4.1: Methods for the SFs extraction and manipulation. (A) A single bundle was isolated from A7r5 cells by removing an apical cell membrane, cytosol, and nucleus via the hypotonic shock technique. The bundle could remain attached to an underlying substrate by treating the de-roofed cells with a detergent. Further manipulation can be achieved by a functionalized glass need. (B) Device for the bundle force measurement[118].

4.2 Model overview

Different with the model descried in the previous topic, each bundle consists of two sub-bundles, and each sub-bundle is composed by the identical number of F-actins with the same polarity positioned along a single circle whose radius is 13.5 nm (Fig. 4.2). The barbed ends of F-actins are attached to either the left or the right boundary. This configuration results in a bundle structure similar to the sarcomere found in muscle cells. Unless specified, the bundle length in the z direction is 5 μm with an F-actin length of 4.9 μm. According to polarity, 50 F-actins are symmetrically distributed in two sub-bundles in the computational domain as the reference case. The number of filament can vary in several simulations for investigating the effects of bundle mechanical properties.

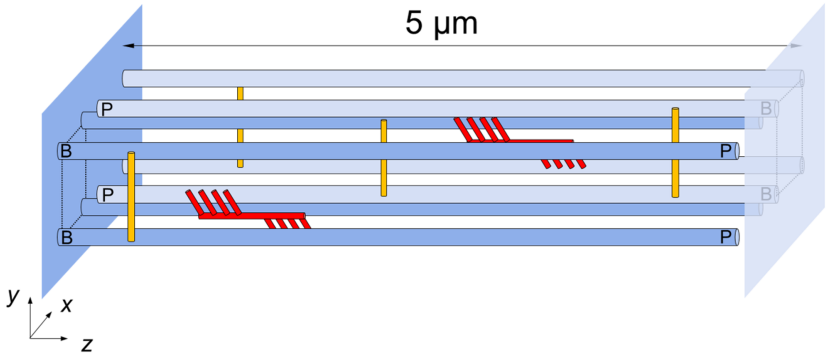

Figure 4.2: Structure of the sarcomeric model. The bundle consists of two sub-bundles, and each sub-bundle is composed by the identical number of F-actins with the same polarity. "B" and "P" indicate the barbed and pointed ends of the F-actins, respectively. The barbed ends of F-actins are attached to either the left or the right boundary. Deep and light blue colors denote the two sub-bundles of F-actins with anti-parallel polarities. The red color represents the myosin thick filaments, and the yellow color is for the ACPs.

4.3 Rheological test in the simulation

In the first 10s of simulations motors are assembled, and their arms bind to F-actins without walking. The arms of ACPs also bind to pairs of parallel F-actins to form cross-links. After the completion of this network formation, motor arms are allowed to walk. In addition, the +z boundary where the barbed ends of one sub-bundle are attached starts moving in +z direction, following a linearly increasing strain. After reaching the maximum strain level, the boundary moves in the -z direction with the same or different strain rate ($\dot{\varepsilon}$) until it comes back to the initial position. This results in the extension and compression of the bundle. Unless specified, the molar ratios of motors ($R_{\mathrm{M}} = C_{\mathrm{M}}/C_{\mathrm{A}}$) and ACPs ($R_{\mathrm{ACP}} = C_{\mathrm{ACP}}/C_{\mathrm{A}}$) are set to 0.01 and 0.1, respectively, where C_i denotes the concentration of each cytoskeletal components. With this rheological setting, we found the simulation with a maximum strain of 50% can reproduce the stretch-compression experiment well. As a reference value, the strain rate was set by 0.1 for the stretch phase, meaning 5 seconds according to the strain level, and it of the compression phase varies for comparison.

4.4 Quantification of bundle contour length and tensile forces

In this model, a bundle is formed by two sub-bundles with anti-parallel F-actins distributed in a symmetric manner. In both sub-bundles, F-actins have identical length and their barbed ends are clamped to the boundaries elastically. This arrangement mimics the sarcomeric structure in SFs. Since the bundle is formed in a three-dimensional domain, bundle buckling during the compression phase can exist in any cross-section that is perpendicular to its longitudinal direction. To quantify the bundle contour length in each time step, a middle cross-section plane is detected that identically bisects the instantaneous length between two boundaries in z direction. Using the coordinates of each actin segment, contour length in each half bundle can be calculated by accumulating the spatial distance between

two adjacent actin segments from the boundary to the middle position. Therefore, the entire bundle contour length (L) equals to the summation of that of the two half bundles.

To quantitatively measure the tensile forces with a high time resolution, the bundle is divided in z direction with 20 cross-sections. Polymer chains that cross each cross-section plane are detected, including F-actins, motor backbones, motor arms, and ACPs. Simultaneously, forces in those chains can be measured and be recorded per 0.1s, and only their components in z direction are considered. Based on this, tensile force in all divisions along the bundle can be analyzed during the entire stretch and compression processes. The bundle force, F_{B}, is the average of the detected tensile forces in all divisions during each time step.

4.5 Bundle buckling and recovery are functions of the strain rate but independent of its mechanical properties

In our in vitro experiment, the contractility of the extracted fibers can be maintained by adding the Mg-ATP buffer (Fig. 4.3A). The isolated SFs exhibited diverse responses depending on their external forces. Seven cycles of stretch and compression were conducted with increasing strain value. In all these cycles, we observed different buckling scales of SFs followed by a gradual deformation into a straight shape (Fig. 4.3B). By recording the change in their contour lengths over time, we found the SFs compressed with a larger strain rate showed more significant buckling and required a longer time for reforming their linear appearance (Fig. 4.4A and C). This gradual recovery can be ascribed to the active behaviors of myosin-II, which is triggered by the presence of Magnesium-ATP solution. These observations imply SFs have the ability of mechanical adaptation in that they are able to elongate, shorten, buckle, and reestablish the isometric contraction gradually.

To investigate the determinants of this bundle buckling and the subsequent recovery, we first ap-

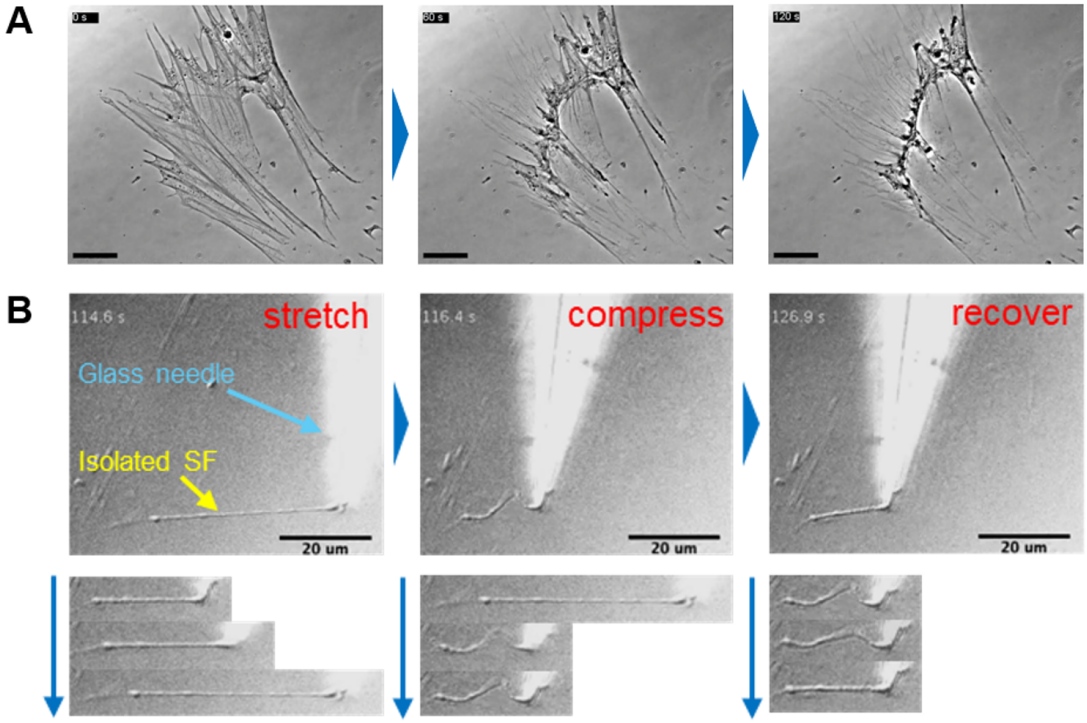

Figure 4.3: In vitro single-fiber experiment. (A) The contractility of the extracted fibers can be maintained by adding the Mg-ATP buffer (1mM) under the temperature of $25°C$ and the ionic strength of 100mM. (B) Buckling of the isolated SF was observed after the stretch-compression manipulation. It was followed by a gradual recovery into a straight shape.

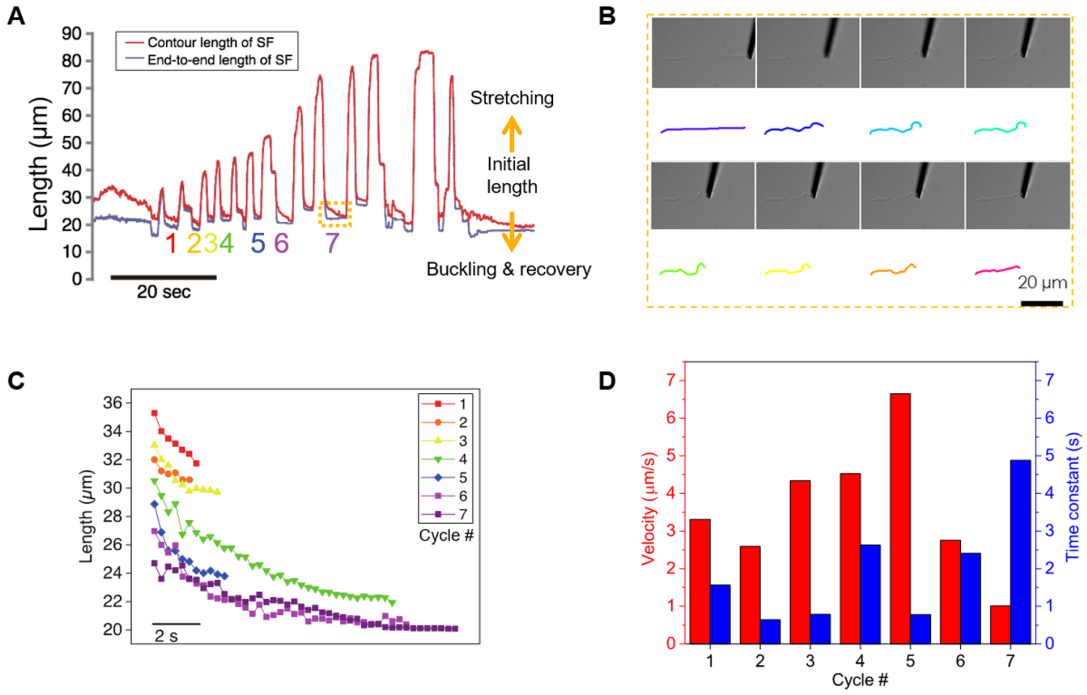

Figure 4.4: Analysis of the cyclic-stretched isolated SF. (A) Recording of the SF contour length and the end-to-end length. Numbers with different colors denote 7 selected cycles during the experiment. (B) An example of showing the recovery phase of the 7th cycle indicated by a dashed square in (A). (C) Recording the changes of the bundle contour lengths of 7 cycles during the recovery phase. (D) The calculated recovery rates of the 7 cycles.

plied our computational model to check wether it can recapture the whole process of the experiment. As shown in Figs. 4.5 and 4.6, a significant buckling can be observed after the compression, following by a recovery phase that is consistent with the experiment results. The stretch and the buckling after compression brought a longer contour length than the initial length. And the following recovery phase gradually reduced the buckling and contour length (Fig. 4.6A). By checking the development of the bundle force, the peak value was reached one second before the end of extension. A following tension release started and F_B stayed zero level during the recovery phase and raised again once the bundle returned to its initial length (Fig. 4.6B). This drastic drop of the bundle force are predominantly resulted from the unbinding events of motor arms and ACPs, because the continuously growing tension during the extension phase can approach to their stall value and trigger the unbinding.

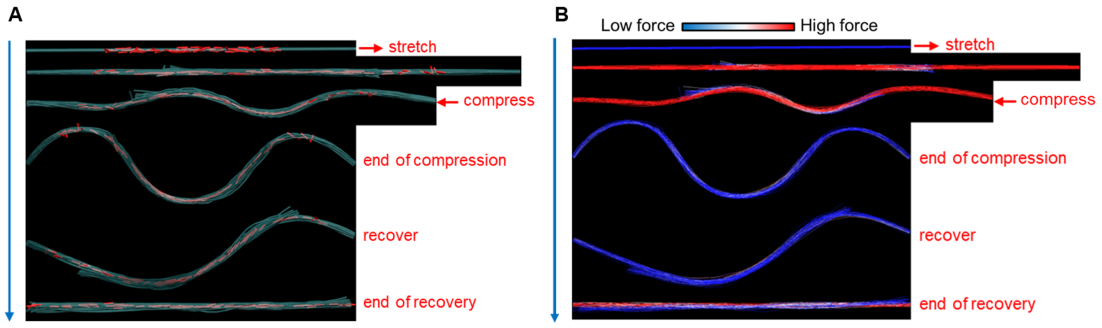

Figure 4.5: Simulation for the bundle stretch-compression experiment. (A) A clear buckling can be observed after the compression, following by a recovery phase that is consistent with the experiment results. Distribution of motors are shown in the red color, and cyan denotes the F-actins. (B) A same bundle visualized in a tension-related manner. The red color represents a high local tension while the blue color represents a low force. A release of tension during the compression phase occurred and the bundle cannot maintain a high tension until the end of recovery phase.

Considering the bundle persistence length, which is indispensable for the buckling level, we adopt two different methods including the alterations of actin bending stiffness and the bundle thickness to vary the persistence length. The bending stiffness between actin segments (k_b) can be enhanced directly and three values including the reference value, 10- and 100-fold of it were applied (Fig. 4.7). Strikingly, the bundle contour length after the compression and the generated force demonstrated a

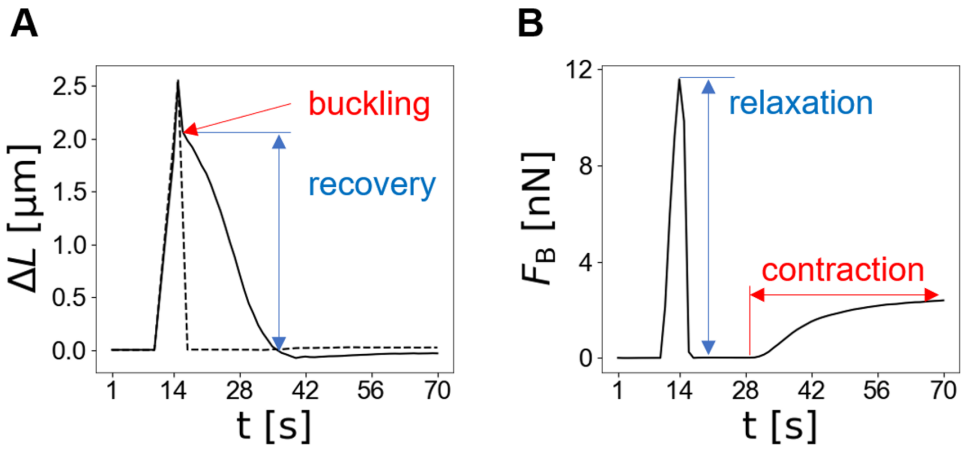

Figure 4.6: Analysis of bundle contour length and bundle force. (A) ΔL represents the change of bundle contour length. The dashed line denotes the position of the right z boundary. The stretch and the buckling after compression brought a longer contour length than the initial length. A following recovery phase gradually reduces the buckling and contour length. (B) F_{B} indicates the averaged bundle force. It reached to a peak value during the extension and a significant relaxation can be observed. The release of tension mainly came from the unbinding events of motor arms and ACPs. F_{B} stayed zero level during the recovery phase and raised again once the bundle returned to its initial length.

similar tendency regardless of the bending stiffness (Figs. 4.7A and C). We further changed the bundle thickness by varying the number of F-actins, N_{fila}, formed for the bundle configuration. Similarly, thinner ($N_{\mathrm{fila}} = 30$) and thicker ($N_{\mathrm{fila}} = 70$) bundles did not present the contour lengths after compression with a large difference compared to the reference case ($N_{\mathrm{fila}} = 50$) (Fig. 4.7B). However, the maximum bundle forces were proportional to the increase of N_{fila} (Fig. 4.7D). It should be noticed that the number of motors (N_{M}) was controlled identically among the bundles with different thicknesses, implying the same contractility. But the number of ACPs would increase within a thicker bundle because there are more actins and only the density of ACPs (R_{ACP}) was controlled. This results in more ACPs between the two sub-bundles and thus enhances bundle connection. Due to its slip-bond property, the thick bundles with more ACPs would become more elastic and consequently high tension can be built up during the extension phase. Together, these results imply that the inherent mechanical property, like the persistence length, would not affect the bundle contour length

during the stretch-compression phase. Therefore, we applied the actin bending stiffness 10-fold higher than the reference value in the following simulations to ensure a clear buckling pattern.

We further tested different strain rate $\dot{\varepsilon}$ for the bundle compression phase. With the largest strain rate ($\dot{\varepsilon} = 0.5, 1$s), the bundle had the longest contour length after compression (Fig. 4.8A) and the subsequent recovery required the longest time compared to others (Fig. 4.8B). This can be explained as that the significant buckling resulted in a longer distance for motors to walk on, which led to a longer recovery time consequently. Furthermore, the majority of motors feeling this large $\dot{\varepsilon}$ would unbind from F-actins since the force values acting on their arms would exceed the stall force level due to the large buckling. On the contrary, large buckling would not occur with a small strain rate (e.g. $\dot{\varepsilon} = 0.05, 10$s). Meanwhile, a certain number of motors could still interact with F-actins because of the lower local tension they felt, which would further shorten the recovery time after the compression. Therefore, the strain rate of the compression phase has a significant influence on the bundle buckling and the bundle recovery time, which is consistent with our observation in the experiment of isolated SFs.

4.6 Motor dynamics and density determine the bundle recovery rate and the force generation

Interactions between motor and F-actin are essential for generating the contractile force, which is a complicated mechanochemical process for the myosin cycle. In our experiment, the actin-myosin interactions were activated by adding the ATP-rich solution. To maintain the regular functions of the isolated SFs, the ATP concentration was strictly controlled at the physiological level. This allowed us to investigate the mechanical response of SFs under a certain chemical condition in vitro. However, myosin activity would be largely varied in vivo depending on multiple conditions (e.g. ATP concen-

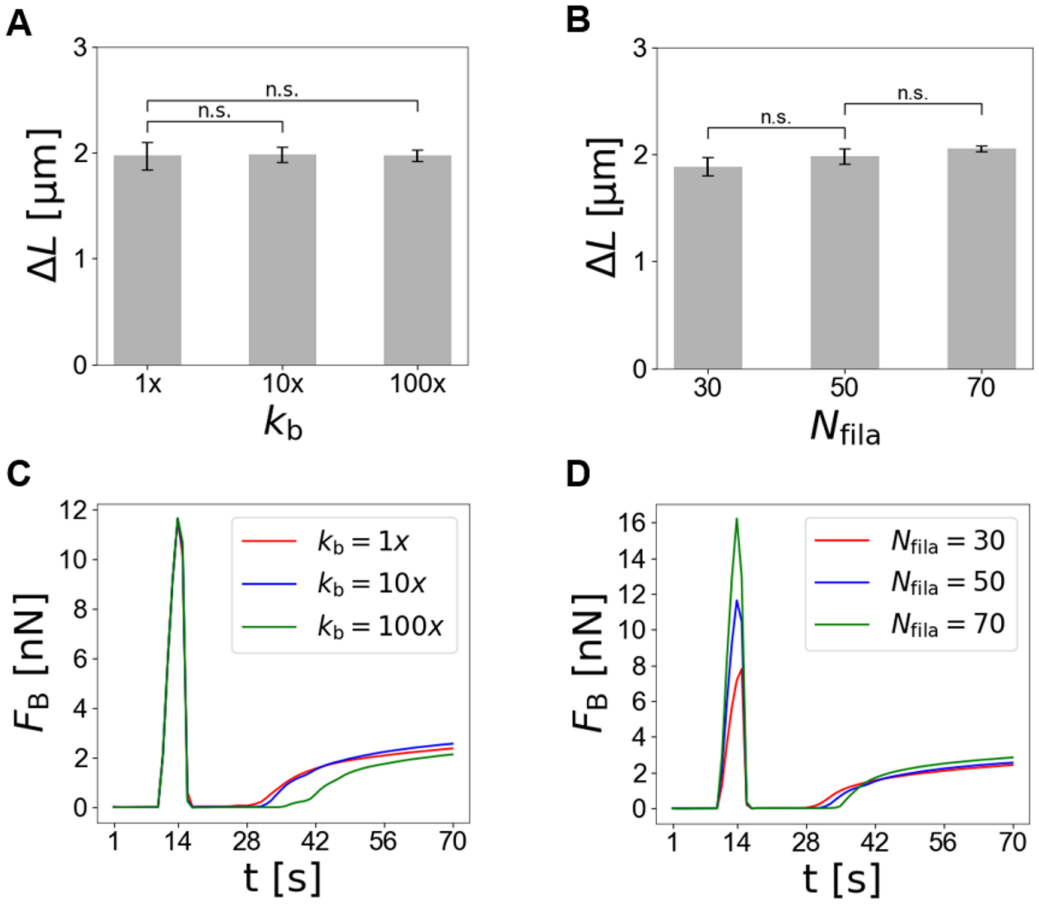

Figure 4.7: Bundle buckling is independent of its mechanical properties. (A) ΔL represents the change of bundle contour length at the end of the compression phase. Altering the bending stiffness of F-actin (k_b) cannot change the contour length significantly. Three cases represents the k_b of the reference value, 10- and 100-fold of the reference value. (B) Changing the bundle thickness by increasing the number of F-actins (N_{fila}) cannot bring difference in ΔL. (C-D) F_B indicates the averaged bundle force. Higher k_b did not show a different bundle force during the stretch-compression phase, whereas the increase of N_{fila} can enhance the maximum F_B due to the large number of ACPs. n.s. represents no significance between data.

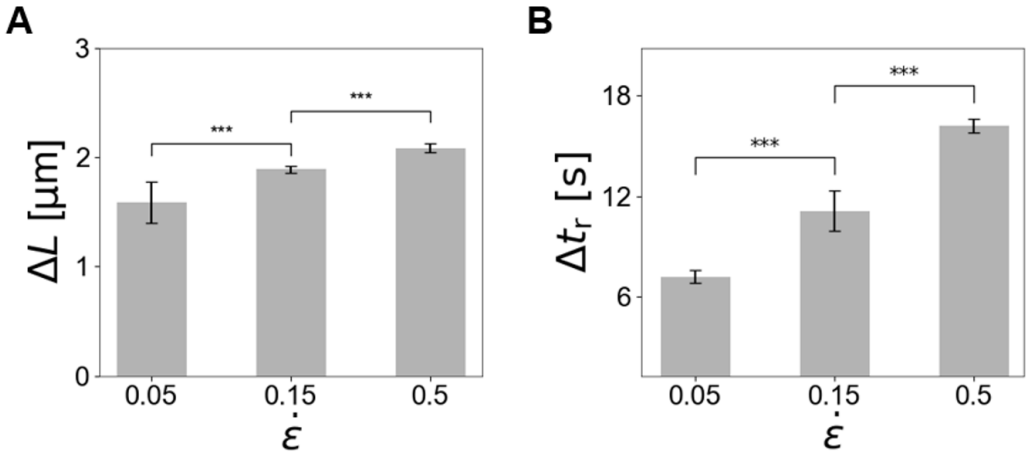

Figure 4.8: Bundle buckling and recovery are functions of the strain rate. (A) ΔL represents the change of bundle contour length at the end of the compression phase. $\dot{\varepsilon} = 0.05, 0.15, 0.5$ represents different strain rates corresponding to compression phases with 10s, 3.3s, and 1s. The bundle contour length increases with an increase of the strain rate. (B) Higher strain rates lead to longer recovery phases due to larger deformations.

tration and pH value)[74,139]. To overcome the obstacle of changing those conditions and keeping the regular functions of SFs in vitro simultaneously, we applied our agent-based model to investigate the motor dynamics influences on the bundle properties during this stretch-compression configuration.

We first adjusted the motor dynamics by changing the motor walking rate R_{w}. With an identical motor density ($R_{\mathrm{M}} = 0.01$), bundles with different motor walking rates demonstrated noticeable differences (Figs. 4.9A and B). Motors with a two-fold higher walking rate ($2\times$) compared to the reference case ($1\times$) contracted the bundle faster than others and a shortest recovery time (Δt_{r}) can be observed (Fig. 4.9B, $2\times$). Motors with a half of the reference walking rate ($0.5\times$) led to a mild decrease in the bundle contour length after the compression (Fig. 4.9B, $0.5\times$). This can be attributed to the fast relative displacement between motor and F-actin, which is highly related to the contractile force. As a consequence, the higher force level from the fast motor walking rate would obviously shorten the bundle recovery phase. However, the motor walking rate would not affect the bundle too much during the compression, because most motors would unbind from F-actins due to the high tension

level. This can explain the non-significance of the contour length after the compression phase between cases (Fig. 4.9A).

Another essential parameter that regulates the bundle mechanical response is the motor density. During a myriad of cell processes, in vivo SFs demonstrate a highly dynamic assembly, in which the number of motors can be different. However, there was no turnover of protein molecules in the isolated SFs and it is difficult to detect the exact number of myosin thick filaments in vitro. Hence, we applied a range of the motor density R_{M} (from 0.002 to 0.01) in the model during the bundle formation phase to investigate how the motor number influences the bundle mechanical reactions. It can be observed that the required recovery time were inversely proportional to the increase of R_{M} (Fig. 4.9C). We averaged the bundle force during the steady state near the end of simulations, the force level improved noticeably with the increase of motor density (Fig. 4.9D). It is significant that a large number of motors can enhance the bundle contraction so that shortens the recovery phase and brings a higher bundle force.

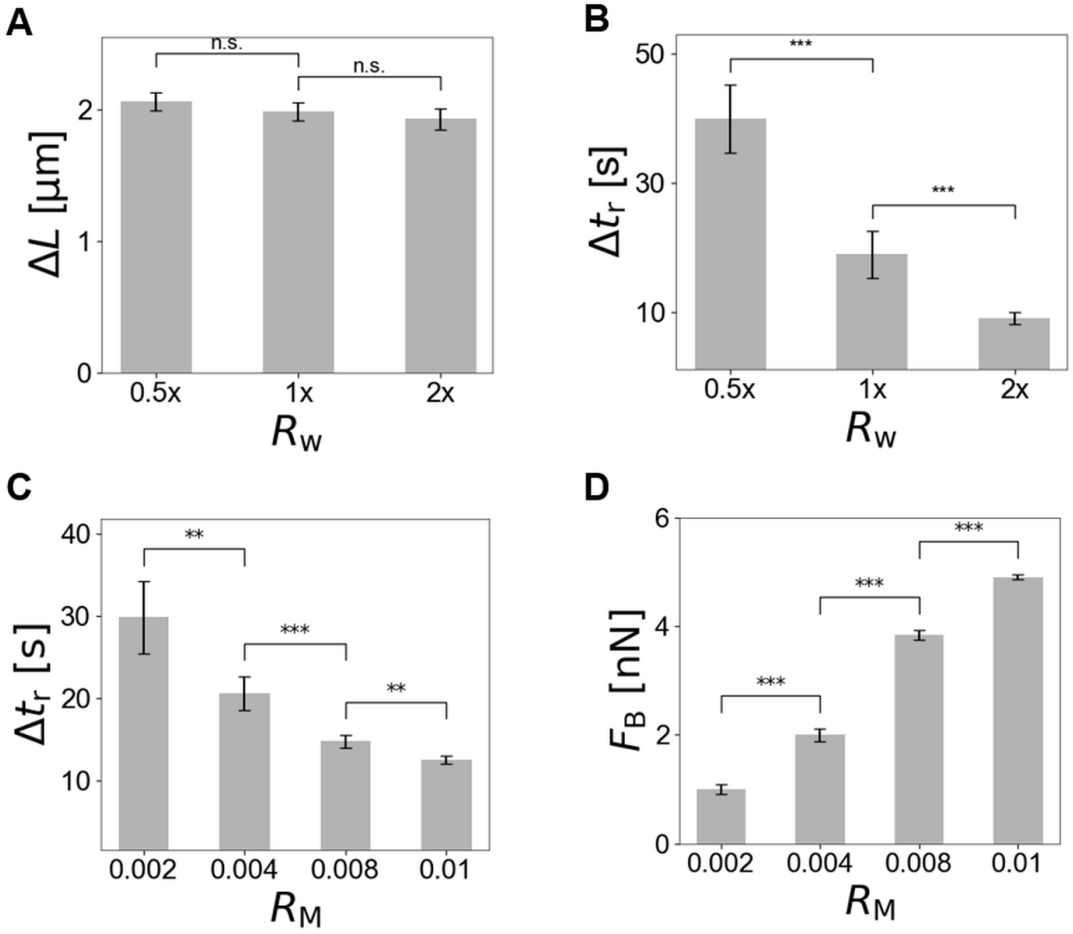

Figure 4.9: [Motor dynamics and density determine the bundle recovery and the force generation. (A) ΔL represents the change of bundle contour length at the end of the compression phase. $\dot{\varepsilon} = 0.05, 0.15, 0.5$ represents different strain rates corresponding to compression phases with 10s, 3.3s, and 1s. The bundle contour length increases with an increase of the strain rate. (B) Higher strain rates lead to longer recovery phases due to larger deformations.

O glaube, du warst nicht umsonst geboren!

Hast nicht umsonst gelebt, gelitten!

Was entstanden ist, das muss vergehen!

Was vergangen, aufersteh'n!

Hör' auf zu beben!

Bereite dich zu leben!

Gustav Mahler, *The Symphony No.2 in C Minor*

5

Discussion of the Actomyosin Impacts to the Bundle Mechanical Adaptation

A large fraction of the mechanical forces are generated by actomyosin bundles that consist mainly of myosin thick filaments, filamentous actins (F-actins), and actin cross-linking proteins (ACPs) called α-actinin. These proteins are distributed along the bundle in a different manners de-

pending on the cell types. Unlike the stereotypical structure found in striated muscles, distribution of these proteins in the non-muscle cells varies adaptively in response to changes in surrounding mechanical environments, which leads to variations in the contractile and mechanical properties of bundles. The adaptive behavior of the actomyosin bundles to mechanical environments is intimately related to diverse biological functions, but the molecular basis of the adaptation remains unclear to date. In this study, we combined our agent-based computational model with in vitro experiments to illuminate the mechanism of the adaptative behavior of actomyosin bundles.

5.1 Actin-Myosin interactions govern the bundle mechanical adaptation

In the in vitro experiments, we observed that the isolated bundles exhibited diverse responses depending on loading conditions; the bundles showed buckling with high curvature after rapid compression, followed by gradual recovery to a straight shape. By contrast, they did not show buckling in response to slow compression. The experimental results also implied that SFs can accommodate to large extension and compression. However, under the cyclic-stretch, we observed the contractility of the isolated SF significantly reduced after multiple cycles even with similar extents of the strain level. Meanwhile, several "dense bodies" appeared along the bundle. These structures might be different from the observations in smooth muscle fibers [53] and are much likely resulted from the disruption of its inner protein arrangement. Such disruptions and the consequent protein accumulation were barely reported in experiments in vivo, since the highly dynamic turnover of monomers occurs in the living cells. However, strikingly, our isolated SF could still adapt to the changes of the external forces by the activation of myosin, suggesting the indispensable contribution from the actin-myosin interactions.

This rate-dependent adaptive behaviors of the bundle were reproduced by the agent-based model.

Using the simulation, we found that buckling patterns vary primarily as a function of a compression rate but independent with the mechanical properties of bundles, such as the bending stiffness of individual F-actin and bundle thickness. On the other hand, the recovery behavior of the bundle depended on the force-dependent dynamic behaviors of myosin motors. With a higher motor walking rate, the bundle can remove the buckling rapidly compared to motors with lower walking rate. This walking speed is highly related to the motor number in each thick filament and the mechanochemical transition rates of myosin states. For instance, the walking speed can be reduced significantly when there is a few motor heads in each myosin ensemble. Meanwhile, this small number of motor heads can diminish the overall stall force level of the whole ensemble. It causes a frequent unbinding of the motor arms and further shortens the duty ratio of the whole ensemble. A numerical attempt for changing the ensemble unbinding rate and walking rate by varying the motor number in each arm and the individual myosin stall force can be found in Fig. A.1. Similarly, bundles with higher motor densities can contract and recover efficiently attributed to the large force generation.

5.2 Necessity of the sarcomeric structure and its potential stabilizer in disorder bundles

One intriguing and essential question is why the ventral stress fiber need to form the sarcomeric structures in serial. Considering other contractile actomyosin structures in non-muscle cells including the transverse arcs and the contractile ring during cell division, the polarities of F-actins and the proteins' distribution are more random. As for the dorsal stress fibers, they are not contractile and there is no myosin associates with dorsal SFs. One compelling explanation can obtained from their mechanical functions. Ventral SFs play vital roles during the cell migration. They are the predominant source of the contractile force and are the main skeleton for maintaining the cell shape. Meanwhile, one ventral

SF connect to two focal adhesions. Unlike transverse arcs and dorsal SFs, which primarily maintain cytoskeletal tension or serve as structural connectors, ventral SFs are responsible for generating contractile forces that are transmitted directly to focal adhesions and the extracellular matrix (ECM). This requires a sarcomeric arrangement of actomyosin structures, where periodic actin filament bundles alternate with myosin filaments, ensuring uniform contraction and efficient force transmission along their length. Without this organization, the forces generated by ventral SFs would be unevenly distributed, reducing their mechanical efficiency.

In contrast, transverse arcs and dorsal SFs do not need sarcomeric structures because their roles differ significantly[109]. Transverse arcs are not anchored to focal adhesions and function primarily as a contractile network supporting cytoskeletal tension, while dorsal SFs connect transverse arcs to focal adhesions at only one end, playing a less active role in force generation. These fibers do not require the same level of structural optimization for force transmission. The sarcomeric organization in ventral SFs also enables the summation of forces from multiple contractile units, amplifying their mechanical output while maintaining energy efficiency. This arrangement is critical for ventral SFs' roles in cell migration and mechanotransduction, where dynamic force adaptation is essential. Thus, the necessity of sarcomeric structures in ventral SFs reflects their specialized function in generating and transmitting forces, a requirement not shared by transverse arcs or dorsal SFs.

Another question is related to the stochastic binding of myosin heads in non-muscle myosin thick filaments. Different from that in the striated muscles, non-muscle myosin thick filaments incorporate a small number of myosin monomers in each ensemble, which would amplify the stochastic property regarding the actin-binding possibility. Similar with the skepticism in muscle modeling introduced before, the uneven bound motor numbers between the two sides of each thick filament might cause a lateral movement of the myosin stack along the bundle. However, this type of myosin sliding has not been observed in cells with their physiological conditions. For the highly organized striated muscle myosin, there are multiple associating priteins including the myosin-binding protein C and my-

omesin that are able to centralize the thick filament. Additionally, the giant protein titin is feasible to function as the myosin stabilizer and the mechanical clutch as introduced before. Considering the non-muscle cells, in fact, there have several recent studies reporting that additional proteins demonstrate the force-balancing and stabilizing functions. For instance, the protein caldesmon can connect the myosin light chains to the tropomyosin isoforms of Tpm 2.1, 1.6 / 1.7, and 3.1 / 3.2[87]. By kocking down this caldesmon protein, an irregular myosin distribution along ventral SFs were observed, which led to defects in processes including cell migration and morphogenesis. In addition, LUZP1, a leucine zipper protein, has been revealed to regulate the SFs' assembly by associating with actin and the neck region of non-muscle myosin II monomer[181]. Furthermore, an actin binding protein, Drebrin has recently reported to stabilize the focal adhesions and enhance the non-muscle myosin II activities in central and peripheral SFs by controlling the kinetics and conformation of the actin-myosin association[120,28]. Nonetheless, ventral SFs can actively adjust the number of sarcomeres by zyxin, which predominantly associates with focal adhesions but was revealed to localize along SFs when a high tension appearing[132,192]. According to their experiments, adjacent sarcomeres have a mechanical communication that can actively compensate the high tension felt by one sarcomere. New sarcomeres can be formed at the high tension area regulated by zyxin once the force exceeds a certain threshold. Interestingly, these myosin- or sarcomere-regulators found in non-muscle cells shown a relatively short lifttime with myosin or actin. This can be attributed to the highly dynamic mechanism of ventral SFs in the living non-muscle cells and further facilitates their ability of mechanical adaptation.

Men,

though they must die,

are not born in order to die

but in order to begin.

Hannah Arendt, *The Human Condition*

6

Conclusion

In this study, we explored the dynamics of force generation in various myosin-based structures, including disorganized bundles and networks, as well as isolated stress fibers (SFs) under different conditions. Our investigations revealed that the properties of myosin thick filaments play a crucial role in regulating the efficiency and magnitude of force generation. Specifically, we observed that while an increased number of myosin motors enhances the tensile forces generated

by bundles and networks, the efficiency of force generation decreases. Additionally, with a fixed number of motors, the force output varies significantly depending on the spatial distribution of motors, the structural characteristics of thick filaments (such as the number of myosin heads and the bare zone length), and the loading conditions. These findings suggest that the structural organization of myosin filaments directly influences their mechanical output.

Our in vitro experiments with isolated SFs highlighted their diverse mechanical responses under different loading conditions. Rapid compression induced buckling with high curvature, followed by a gradual recovery to a straight configuration, whereas slow compression did not result in buckling. These results demonstrate the SFs' significant adaptability to large extensions and compressions through myosin activation, emphasizing the critical role of actin-myosin interactions.

Agent-based simulations supported our experimental findings and provided further insights into the rate-dependent adaptive behaviors of SFs. The simulations demonstrated that buckling patterns are primarily influenced by the compression rate, with minimal dependency on the intrinsic mechanical properties of the bundles, such as bending stiffness and thickness. In contrast, the recovery behavior depended significantly on the force-dependent dynamics of myosin motors. Higher motor walking rates facilitated rapid buckling recovery compared to slower motors, implying the importance of motor kinetics.

Together, these findings illuminate the complex interplay between structural and dynamic factors in myosin-based force generation and adaptation. By integrating experimental observations with computational modeling, we provide a comprehensive understanding of the mechanisms governing the mechanical behavior of myosin filaments and stress fibers. This knowledge paves the way for future studies employing synthetic systems to validate and extend these insights, offering potential applications in bioengineering and cellular mechanics.

A

Dynamics of Agents

A.1 Brownian Dynamics via the Langevin Equation

In this model, F-actin is represented as a series of serially connected cylindrical segments, each characterized by barbed and pointed ends. Actin cross-linking proteins (ACPs) are modeled as two segments connected by an elastic hinge, enabling flexibility in their interactions. Motors are designed to mimic the structure of myosin thick filaments, with each motor comprising a backbone structure that con-

tains a certain number of arms (N_a). Each arm corresponds to 8 real myosin heads ($N_h = 8$), leading to a total of $N_h N_a$ myosin heads per motor. The backbone itself is composed of multiple identical segments, with a bare zone at its center consisting of one or more segments. The arms of the motor are connected to the endpoints of backbone segments located outside the bare zone, with the spacing between adjacent motor arms corresponding to the length of a single backbone segment.

The dynamics of the segments constituting F-actin, motors, and ACPs are governed by the Langevin equation, where inertial effects are neglected:

$$\zeta_i \frac{d\mathbf{r}_i}{dt} = \mathbf{F}_i + \mathbf{F}_i^{\mathrm{T}}, \tag{A.1}$$

where $\mathbf{r}_i$ is the position vector of the ith element, ζ_i represents the drag coefficient, t is the time, $\mathbf{F}_i$ is the deterministic force, and $\mathbf{F}_i^{\mathrm{T}}$ is the stochastic force. The stochastic force satisfies the fluctuation-dissipation theorem[174]:

$$\langle \mathbf{F}_i^{\mathrm{T}}(t) \cdot \mathbf{F}_j^{\mathrm{T}}(t') \rangle = 2k_{\mathrm{B}} T \zeta_i \delta_{ij} \delta(t - t'), \tag{A.2}$$

where δ_{ij} is the Kronecker delta, $\delta(t - t')$ is the Dirac delta function, k_{B} is the Boltzmann constant, T is the absolute temperature, and $\Delta t = 1.15 \times 10^{-5}$ s is the simulation time step.

Drag coefficients are calculated using an approximate formula for cylindrical objects[21]:

$$\zeta_i = 3\pi\mu r_{c,i} \frac{(3 + 2r_{0,i}/r_{c,i})}{5}, \tag{A.3}$$

where μ is the viscosity of the surrounding medium, $r_{0,i}$ is the length of the segment, and $r_{c,i}$ is the diameter of the segment. The position vectors of all segments are updated at each time step using the Euler integration scheme:

$$\mathbf{r}_i(t + \Delta t) = \mathbf{r}_i(t) + \frac{\Delta t}{\zeta_i}(\mathbf{F}_i + \mathbf{F}_i^{\mathrm{T}}). \tag{A.4}$$

A.2 Structures of Elements and Deterministic Forces

The deterministic forces acting on the elements are categorized as follows: i) extensional forces maintaining equilibrium lengths, ii) bending forces preserving equilibrium angles, and iii) repulsive forces accounting for volume-exclusion effects between F-actins. The extensional and bending forces arise from specific potential energy functions:

$$U_{\mathrm{b}} = \frac{1}{2}\kappa_{\mathrm{b}}(\theta - \theta_0)^2, \tag{A.5}$$

$$U_{\mathrm{s}} = \frac{1}{2}\kappa_{\mathrm{s}}(r - r_0)^2, \tag{A.6}$$

where κ_{b} and κ_{s} represent the bending and extensional stiffnesses, respectively, θ and θ_0 denote the instantaneous and equilibrium angles, and r and r_0 are the instantaneous and equilibrium lengths of the segments.

The equilibrium parameters for F-actin segments, ACP arms, and motor backbones are defined by their respective stiffnesses and geometries, ensuring structural consistency during simulations. Repulsive forces are modeled using a harmonic potential, and their parameters are set to prevent overlapping of actin segments. An equilibrium angle formed by two adjacent actin segments ($\theta_{0,\mathrm{A}} = 0$ rad) and the equilibrium length of actin segments ($r_{0,\mathrm{A}} = 140$ nm) are regulated by the bending ($\kappa_{\mathrm{b,A}}$) and extensional ($\kappa_{\mathrm{s,A}}$) stiffnesses of F-actin, respectively. The value of $\kappa_{\mathrm{b,A}}$ corresponds to the persistence length of 9 μm[68]. An equilibrium angle formed by two arms of each ACP ($\theta_{0,\mathrm{ACP}} = 0$ rad) and the equilibrium length of ACP arms ($r_{0,\mathrm{ACP}} = 23.5$ nm) are maintained by the extensional ($\kappa_{\mathrm{s,ACP}}$) and bending ($\kappa_{\mathrm{b,ACP}}$) stiffnesses of ACPs, respectively.

An equilibrium angle formed by adjacent backbone segments ($\theta_{0,\mathrm{M}} = 0$ rad) and the equilibrium

length of motor backbone segments ($r_{s,M1}$) are maintained by bending ($\kappa_{b,M}$) and extensional ($\kappa_{s,M1}$) stiffnesses, respectively. The value of $\kappa_{s,M1}$ is equal to that of $\kappa_{s,A}$, whereas the value of $\kappa_{b,M}$ is larger than that of $\kappa_{b,A}$ so that the backbone does not bend significantly. The reference value of $r_{s,M1}$ is 42 nm, but it is varied in some of the simulations to increase the spacing between motor arms as well as the total length of the motor backbone. The number of segments in the bare zone determines the length of the bare zone. Two motor arms are located on each endpoint of backbone segments which are not part of the bare zone. The extension of each motor arm is regulated by the two-spring model with transverse ($\kappa_{s,M2}$) and longitudinal ($\kappa_{s,M3}$) springs. The transverse spring regulates an equilibrium distance ($r_{0,M2} = 13.5$ nm) between the endpoint of a motor backbone and an actin segment where the arm of the motor is bound, whereas the longitudinal spring maintains a right angle between the motor arm and the actin segment ($r_{0,M3} = 0$ nm).

Repulsive forces are from a harmonic potential[83]:

$$U_r = \begin{cases} \frac{1}{2}\kappa_{r,A}(r_{12} - r_{c,A})^2 & \text{if } r_{12} < r_{c,A}, \\ 0 & \text{if } r_{12} \geq r_{c,A}. \end{cases} \tag{A.7}$$

where $\kappa_{r,A}$ is the strength of repulsive force, and r_{12} is the minimum distance between two neighboring actin segments.

Forces exerted on actin segments by bound motor arms and ACPs or by the repulsive forces are distributed onto two ends (barbed and pointed ends) of the actin segments as described in our previous work in detail[73].

A.3 Dynamic Behaviors of ACPs

The arms of ACPs bind to F-actin segments at specific binding sites spaced 7 nm apart. Two arms that belong to the same ACP are not allowed to bind to the identical F-actins. Binding occurs at a constant rate without any preference for the contact angle. Once bound, ACPs form permanent cross-links in the study introduced in chapter 2, ensuring stable interactions during the simulation. For other simulations, ACPs can unbind from F-actin, following Bell's law[9]:

$$k_{\mathrm{u,ACP}} = \begin{cases} k^0_{\mathrm{u,ACP}} \exp\left(\frac{\lambda_{\mathrm{u,ACP}} |\mathbf{F}_{\mathrm{s,ACP}}|}{k_{\mathrm{B}} T}\right) & \text{if } r_{\mathrm{ACP}} \geq r_{\mathrm{o,ACP}}, \\ k^0_{\mathrm{u,ACP}} & \text{if } r_{\mathrm{ACP}} < r_{\mathrm{o,ACP}}. \end{cases} \tag{A.8}$$

where $k^0_{\mathrm{u,ACP}}$ is the zero-force unbinding rate constant, $\lambda_{\mathrm{u,ACP}}$ represents the sensitivity of the unbinding rate to an applied force $\mathbf{F}_{\mathrm{s,ACP}} = \nabla U_{\mathrm{s,ACP}}$, and r_{ACP} denotes the instantaneous length of ACP arms. The values of $k^0_{\mathrm{u,ACP}}$ and $\lambda_{\mathrm{u,ACP}}$ are adopted from a previous single-molecule experiment[37].

A.4 Dynamic Behaviors of Motors

Motor arms bind to F-actin segments at a rate of $40 N_{\mathrm{h}}\ \mathrm{s}^{-1}$, where N_{h} is the number of myosin heads per arm. Proper alignment with the polarity of F-actin is required for binding, as misaligned motor heads do not interact with actin filaments[171,155]. Upon binding, motor arms walk toward the barbed end of F-actin at rates determined by the parallel cluster model (PCM)[36,35], which simulates the mechanochemical cycle of non-muscle myosin II. The walking and unbinding rates are modulated by applied loads, incorporating catch-bond behavior.

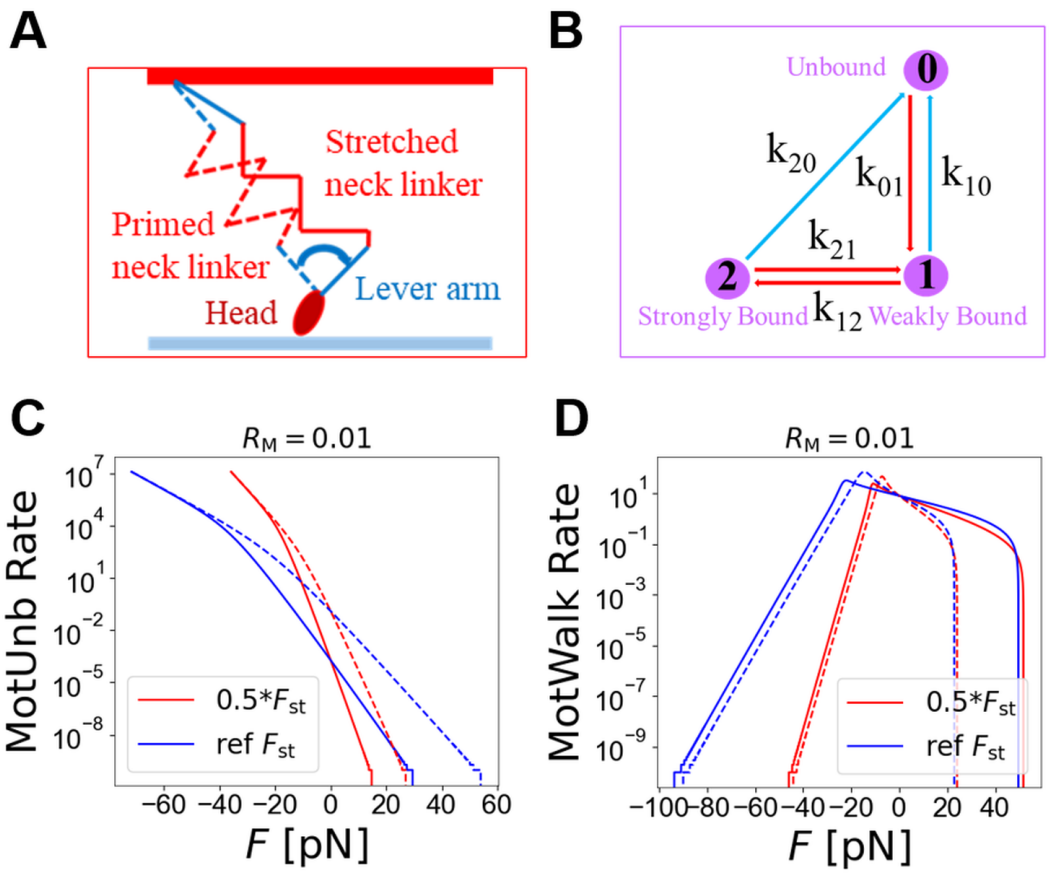

Figure A.1: Dynamics of the motor ensemble is regulated by the parallel cluster model. (A) Myosin lever arm swings with an angle triggered by the Pi release, causing the actin-myosin transition from the weakly bound state to the strongly bound state. (B) Mechanochemical transitions among the three states in myosin ATPase cycle. (C) Unbinding rate of the myosin ensemble based on PCM is highly affected by the stall force of individual myosin head (F_{st}) and the number of motor head in each ensemble (N_{h}). (D) Walking rate of the myosin ensemble based on PCM. Solid lines denote $N_{\text{h}} = 8$, whereas the dashed lines represent $N_{\text{h}} = 4$.

A.5 Tables of Parameters

The parameter values used in the model are provided in Table. A.1, detailing the structural and dynamic properties of F-actin, ACPs, and motors. Table. A.2 lists parameters specific to the PCM, including rates and forces.

Table A.1: List of parameters used in the model.

Symbol	Definition	Value
$r_{0,\mathrm{A}}$	Equilibrium length of the actin segment	1.4×10^{-7} [m]
$r_{\mathrm{c,A}}$	Diameter of the actin segment	7.0×10^{-9} [m]
$\theta_{0,\mathrm{A}}$	Equilibrium angle of F-actin	0 [rad]
$\kappa_{\mathrm{s,A}}$	Extensional stiffness of F-actin	1.69×10^{-2} [N/m]
$\kappa_{\mathrm{b,A}}$	Bending stiffness of F-actin	2.64×10^{-19} [N · m]
$r_{0,\mathrm{ACP}}$	Equilibrium length of the ACP segment	2.35×10^{-8} [m]
$r_{\mathrm{c,ACP}}$	Diameter of the ACP segment	1.0×10^{-8} [m]
$\theta_{0,\mathrm{ACP}}$	Equilibrium angle of ACP	0 [rad]
$\kappa_{s,\mathrm{ACP}}$	Extensional stiffness of the ACP	2.0×10^{-3} [N/m]
$\kappa_{b,\mathrm{ACP}}$	Bending stiffness of ACP	1.04×10^{-19} [N · m]
$r_{0,\mathrm{M1}}$	Equilibrium length of the motor backbone segment	$42 - 138$ [nm]
$r_{\mathrm{c,M}}$	Diameter of the motor backbone segment	1.0×10^{-8} [m]
$\theta_{0,\mathrm{M}}$	Equilibrium angle of the motor backbone	0 [rad]
$\kappa_{\mathrm{s,M1}}$	Extensional stiffness of the motor backbone	1.69×10^{-2} [N/m]
$\kappa_{\mathrm{b,M}}$	Bending stiffness of the motor backbone	5.07×10^{-18} [N · m]
$r_{0,\mathrm{M2}}$	Equilibrium length 1 of the motor arm	1.35×10^{-8} [m]
$r_{0,\mathrm{M3}}$	Equilibrium length 2 of the motor arm	0 [m]
$\kappa_{\mathrm{s,M2}}$	Extensional stiffness 1 of a motor arm	1.0×10^{-3} [N/m]
$\kappa_{\mathrm{s,M3}}$	Extensional stiffness 2 of a motor arm	1.0×10^{-3} [N/m]
N_{h}	Number of myosin heads per motor arm	8
N_{a}	Number of arms in a single motor	$4 - 48$
$\kappa_{\mathrm{r,A}}$	Strength of the repulsive force	1.69×10^{-3} [N/m]
N_{M}	Number of motors in the system	$1 - 2,000$
$\Delta \mathrm{t}$	Time step	1.15×10^{-5} [s]
μ	Viscosity of the medium	8.6×10^{-1} [kg/m · s]
$k_{\mathrm{B}}T$	Thermal energy	4.142×10^{-21} [J]

Table A.2: Parameter values used for the parallel cluster model.

Symbol	Definition	Value
k_{01}	A rate from unbound to weakly bound state	$40\ [\mathrm{s}^{-1}]$
k_{10}	A rate from weakly bound to unbound state	$2\ [\mathrm{s}^{-1}]$
k_{12}	A rate from weakly bound to post-power-stroke state	$1,000\ [\mathrm{s}^{-1}]$
k_{21}	A rate from post-power-stroke to weakly bound state	$1,000\ [\mathrm{s}^{-1}]$
k_{20}	A rate from post-power-stroke to unbound state	$20\ [\mathrm{s}^{-1}]$
F_0	Force dependence	$5.04 \times 10^{-12}\ \mathrm{N}$
E_{pp}	Free energy bias toward the post-power-stroke state	$-60 \times 10^{-21}\ [\mathrm{J}]$
E_{ext}	External energy contribution	$0\ [\mathrm{J}]$
d	Step size	$7 \times 10^{-9}\ [\mathrm{m}]$
k_{m}	Spring constant of the neck linkers	$1 \times 10^{-3}\ [\mathrm{N/m}]$

B

Parallel Cluster Model

According to the cross-bridge model, binding and unbinding events of each myosin-II protein can be described in stochastic transitions with certain transition rates[63]. However, dividing the myosin cycle into only two states can reduce the resolution a lot when we consider the overall dynamics of an ensemble. Therefore, the PCM is adopted in this study which separates the myosin cycle into three mechanochemical states including the unbound (free), weakly bound (pre-power stroke), and strongly bound (post-power stroke) states[36,35]. In addition, the local thermodynamic equilibrium

can be assumed in each ensemble due to the instant transitions among myosin states compared to the relatively long time that muscle activities cost[72]. Based on this assumption, a certain distribution of the three myosin states can be calculated, which simplifies the simulation significantly. Using subscripts 0, 1, and 2 to represent the unbound, weakly bound, and strongly bound states, respectively. Then, the transition rates among these mechanochemical states can be denoted as $k_{01}, k_{10}, k_{12}, k_{21}$, and k_{20}. Considering the thermodynamics, transitions between states 0 and 1, states 1 and 2 are reversible, while only the unbinding from state 2 to 0 is irreversible since a new ATP binds to the myosin and is hydrolyzed during this process. Assume that there are a total N number of myosin in the ensemble and i of them exist in the bound states. Then, the number of free myosin is $N-i$. Similarly, with j number of myosin staying at the strongly bound state, the number of myosin in the weakly bound state can be denoted as $i-j$. It should be noticed that the relation among these parameters is $0 \leqslant j \leqslant i \leqslant N$.

In the PCM, the behavior of power stroke and the most unbinding events are induced by the local force exerted on the protein, and monomers in the same state are regarded to share the equivalent load[35]. Based on this assumption, myosin proteins in the weakly bound state have the same strain ε_{ij} where the subscripts indicate that this strain depends on the state (i, j) of the entire ensemble. With the release of Pi, the subsequent power stroke can stretch the myosin monomer with a further strain d to the strongly bound state. Regarding a constant external force F_{ext} acting on the ensemble, it has to be balanced by the elastic force arising by the myosin monomers as $F_{\text{ext}} = k_{\text{m}}[(i-j)\varepsilon_{ij} + j(\varepsilon_{ij} + jd)] = k_{\text{m}}(i\varepsilon_{ij} + jd)$, in which k_{m} is the stiffness of the myosin neck linker determined by single-molecule studies[175]. Therefore, the myosin strain in the weakly bound state can be calculated as follows,

$$\varepsilon_{ij} = \frac{1}{i}[(F_{\text{ext}}/k_{\text{m}}) - jd] \tag{B.1}$$

Based on this expression of strain, the elastic energy stored in bound myosin can be calculated as $E_{ij}^{\text{el}} =$

$k_m[(i-j)\varepsilon_{ij}^2 + j(\varepsilon_{ij}+d)^2]/2$. Since a constant external force cannot bring energy contribution to the ensemble, then the total energy in an ensemble is $E_{ij} = E_{ij}^{el} + jE_{pp}$, where E_{pp} denotes the energy bias to the strongly bound state caused by Pi release. Therefore, according to the assumption of local thermodynamic equilibrium, the Boltzmann distribution can be adopted to describe the conditional probability to find j number of myosin existing in the state 2 with a given condition of i as $\Pr(j|i) = \exp(-E_{ij}/k_B T)/Q_i$, in which $k_B T$ represents the local thermal energy in the ensemble, and Q_i is the partition sum.

According to the single-molecule studies, transition rates k_{01}, k_{10}, k_{12}, and k_{21} can be considered constants since their relative stability compared to the unbinding that predominantly depends on the unbinding force $F_0 = k_B T/\delta$[175,178]. The parameter δ indicates an additional strain during the unbinding process, which is frequently observed in experimental works[175]. Therefore, the transition rate from state 2 to 0 can be calculated as $k_{20}(i,j) = k_{20}^0 \exp[-k_m(\varepsilon_{ij}+d)/F_0]$, where k_{20}^0 is the zero-force unbinding rate obtained from experiments. Based on these expressions, the effective binding and unbinding rates for myosin in the ensemble with state (i,j) can be calculated as follows.

$$k_{on}(i) = (N-i)k_{01} \tag{B.2}$$

$$k_{off}(i) = \sum_{j=0}^{i}[(i-j)k_{10} + jk_{20}(i,j)]\Pr(j|i) \tag{B.3}$$

In order to evaluate the dynamics of the entire ensemble, its position alteration needs to be defined quantitatively. Considering the backbone of myosin thick filament, it is assembled by the myosin coiled-coil tails, which indicates the position of myosin anchors can be simplified as a relative constant

Z_0. Consequently, the position of each bound myosin head Z_{ij} equals the summation of Z_0 and its corresponding offset from the backbone. Since the conformational change triggered by the power stroke cannot change the position of the bound myosin head, thus the offset of both myosin heads in states 1 and 2 equals the strain value ε_{ij}. Assuming the position of an ensemble $\bar{Z}_{ij}$ is the averaged coordinate of all bound myosin. Hence, it can be expressed as $\bar{Z}_{ij} = Z_{ij} = Z_0 + \varepsilon_{ij}$. Since the ensemble movements only depend on the binding and unbinding dynamics according to the cross-bridge model, the unbound myosin can present a zero-strain state that implies its position can be simplified as Z_0 as well. As a result, an additional binding event can alter the ensemble to a new position $\bar{Z}'_{ij}$ with a step value ΔZ_i^{on} as shown below.

$$\bar{Z}'_{ij} = \frac{i\bar{Z}_{ij} + Z_0}{i+1} = Z_0 + \frac{i}{i+1}\varepsilon_{ij} \tag{B.4}$$

$$\Delta Z_i^{\text{on}} = \sum_{j=0}^{i} (\bar{Z}_{ij}^{i} - \bar{Z}_{ij}) \Pr(j|i) = -\frac{i}{i+1} \sum_{j=0}^{i} \varepsilon_{ij} \Pr(j|i) \tag{B.5}$$

Similarly, an additional unbinding event of myosin with its offset can bring the ensemble to a new position $\bar{Z}''_{ij}$ with a step size $\Delta Z_{ij}^{\text{off}}$ as shown below.

$$\bar{Z}''_{ij} = \frac{i\bar{Z}_{ij} - Z_{ij}}{i-1} = Z_0 + \varepsilon_{ij} \tag{B.6}$$

$$\Delta Z_{ij}^{\text{off}} = \bar{Z}''_{ij} - \bar{Z}_{ij} = 0 \tag{B.7}$$

According to Eq.B.7, the result indicates that unbinding in the PCM cannot affect the ensemble position. However, there exists a special situation in which the unbinding of the only bound myosin ($i = 1$) can change the position of the entire ensemble. In this case, the unbinding step can be represented by the offset of the related myosin as $\Delta Z_{1j}^{\text{off}} = -\varepsilon_{1j}$, where $j = 0, 1$.

In the PCM, the velocity of the myosin ensemble can be obtained by multiplying the effective binding or unbinding rate with its corresponding step value[36]. As shown in Eq.B.7, for the transition of unbinding, only that of the last bound myosin can influence the result. Thus the ensemble velocity for a given condition of i can be expressed as follows.

$$\begin{aligned} V_i =& k_{\text{on}}(i)\Delta Z_i^{\text{on}} + [k_{10}\varepsilon_{10}\Pr(0|1) + \\ & k_{20}(1,1)\varepsilon_{11}\Pr(1|1)]\delta_{i1} \end{aligned} \tag{B.8}$$

where δ_{i1} denotes the Kronecker delta that can determine whether the condition $i = 1$ exists.

Publication List

Publications

Ding, S., Chou, P. E., Deguchi, S., & Kim, T. (2024). Impacts of Structural Properties of Myosin II Filaments on Force Generation. *eLife, accepted*, eLife-RP-RA-2024-105236. DOI: 10.7554/eLife.105236.

Ding, S., Deguchi, S., & Kim, T. (2024). Unraveling a Key Molecular Player Governing Pulmonary Alveolar Development. *American Journal of Respiratory Cell and Molecular Biology, 70*(4), 237-238 (commentary).

Zhao, Y., **Ding, S.**, & Todoh, M. (2022). Validate the Force-Velocity Relation of the Hill's Muscle Model from a Molecular Perspective. *Frontiers in Bioengineering and Biotechnology, 10*, 1006571.

Conferences

Ding, S., Kim, T., & Deguchi, S. (2024). Elucidating the Adaptive Mechanical Behaviors of Actomyosin Bundles in Cells. *2024 21st International Union for Pure and Applied Biophysics (IUPAB) and 62nd Annual Meeting of the Biophysical Society of Japan Congress*, Kyoto, Japan, poster

presentation no. 26P-218.

Ding, S., Matsunaga, D., Kim, T., & Deguchi, S. (2023). Mechanical Adaptation of Actomyosin Fibers: Experiment and Simulation. *12th Asian-Pacific Conference on Biomechanics*, Kuala Lumpur, Malaysia, oral presentation, no. p6b-83.

Ding, S., Kim, T., Matsunaga, D., & Deguchi, S. (2023). Numerical Analysis of Mechanical Response of Stress Fibers. *2023 Annual Conference of JSME*, Tokyo, Japan, oral presentation, no. s021-02.

Ding, S., Zhao, Y., & Todoh, M. (2022). Computational Modeling of the Force-Velocity Relation in Skeletal Muscle for Potential Muscular Rehabilitation Therapy. *2022 IEEE/RSJ International Conference on Intelligent Robots and Systems (IROS)*, Kyoto, Japan, oral presentation, no. 4838.

Zhao, Y., Zhang, M., **Ding, S.**, Todoh, M., & Feng, L. (2022). Computational Simulation for Lifting Motion of Musculoskeletal Arm. *The 34th Chinese Control and Decision Conference (CCDC), IEEE*, Hefei, China, accepted paper ID 550.

Ding, S., Matsunaga, D., Fukushima, S., & Deguchi, S. (2022). RICM-based Micro-Object Detection and Applications. *32nd Bio-Frontier Conference (JSME)*, online, oral presentation, no. 1D13.

Ding, S., Matsunaga, D., Fukushima, S., & Deguchi, S. (2022). RICM-based Micro-Object Detection and Application. 11th Asian-Pacific Conference on Biomechanics, Kyoto, Japan, poster presentation, no. pp1-15.

Acknowledgments

First of all, I would like to express my deep appreciation to Prof. Shinji Deguchi, who has been my supervisor during my whole study life here in Osaka. As an international student who lived alone in an unfamiliar land for the first time, I encountered many difficulties at the beginning. Prof. Deguchi always lent his hand to me whenever I needed help. His warm heart and open mind are the best fortune I could ever expect. Regarding my studies, I experienced great confusion when I was a master's student. Magical words including "stress fibers", "myosin", and "actin" always threw me into a great labyrinth of terms. At that time, I had no background knowledge related to cytoskeleton elements since I majored in mechanical design for my undergraduate study. Huge self-doubt together with the cultural impact hit me like an enormous tide. It was at that time that he encouraged me to start with the areas I was familiar with and take the time to understand the main topics of the laboratory step by step. It is clear that I could never have had a chance to finish this study without Prof. Deguchi's help.

I also want to show my profound gratitude to Prof. Taeyoon Kim at Purdue University. Prof. Kim takes me seriously as his own student and has held weekly discussions for the past three years. I was deeply impressed by his rigorous attitude towards academics. Every week's discussion taught me a lot and such regular discussion every Monday night (due to the time difference) reshaped my

understanding of many things, including not only the details of the agent-based simulation but also the critical thinking for any question and result we got. It has inevitably become a part of my study life to prepare for and enjoy each meeting with Prof. Kim.

I also want to send my great thanks to Assoc. Prof. Daiki Matsunaga and Dr. Tsubasa S. Matsui. I remember I disturbed Matsunaga-sensei many times, but he never turned me off. Many questions I asked might be very simple and naive for him. However, he always explained to me patiently. Aside from the academic questions, we enjoyed a lot of discussion related to the literature (i.e. Haruki Murakami, Three-body, Dostoevsky, and so on). When I encountered setbacks, Matsunaga-sensei always showed his sympathy and encouraged me to overcome the difficulties. Matsui-sensei helped me a lot when he was in our lab. I still remember when I arrived at the airport and could not take any transportation due to the pandemic regulations, it was Matsui-sensei who picked me up at the airport and drove me home directly. He taught me many techniques related to microscope usage as well, which facilitated my understanding of biological experiments.

I would like to thank Prof. Shigeo Wada and Prof. Shinya Aoi for reviewing my thesis.

A profound gratitude from me is also for Asst. Prof. Takumi Saito, Dr. Pirawan Chantachotikul, Rosario Ibáñez Prat, Intan Chairun Nisa, and Yuika Ueda. Their constructive suggestions improved my presentation and enhanced the clarity of the contents. I also want to thank all the lab members for the cheerful and relaxing atmosphere in the lab.

I also want to express my appreciation for the friendship of Sofia Pedrini, Davide Ferri, and Jesus Giovanni. All the experiences and communications we had have strengthened me a lot. At a certain period, I was lost in the definition of good and bad. Their kindness enhanced my faith for many things I believe and kept them away from the interference of "possibility". My friendship with them continues and I trust that human goodness is a common virtue beyond nationality even though I am no longer searching for a clear definition of good or bad.

In addition, I wish to acknowledge and memorize my friend Chong Liu. All the pieces of memory

with him are still my treasures. However, the sudden deterioration and his waving hand from the other side of the curtain in the sterile room engraved my memory so deeply till that peaceful moment. His leaving made me understand that silence can be so accurate and how fragile life can be. All the promises for joking would never have a chance to be fulfilled. However, I am still walking in this world, carrying the treasure from him, and continuously engraving the time on this body like the annual rings. When the icy moon sinks into the ocean of uncertainty, I walk toward the distant mountain of impermanence.

Lastly, I would like to express my greatest gratitude to my family for all the support.

This study is supported by Japan Science and Technology Agency SPRING Project (JPMJSP2138).

References

[1] Abbott, B. & Aubert, X. (1952). The force exerted by active striated muscle during and after change of length. *The Journal of physiology*, 117(1), 77.

[2] Alvarado, J., Sheinman, M., Sharma, A., MacKintosh, F. C., & Koenderink, G. H. (2013). Molecular motors robustly drive active gels to a critically connected state. *Nature physics*, 9(9), 591–597.

[3] Alvarado, J., Sheinman, M., Sharma, A., MacKintosh, F. C., & Koenderink, G. H. (2017). Force percolation of contractile active gels. *Soft matter*, 13(34), 5624–5644.

[4] Åström, J. A., Kumar, P. S., & Karttunen, M. (2009). Aster formation and rupture transition in semi-flexible fiber networks with mobile cross-linkers. *Soft Matter*, 5(15), 2869–2874.

[5] Banerjee, S., Gardel, M. L., & Schwarz, U. S. (2020). The actin cytoskeleton as an active adaptive material. *Annual review of condensed matter physics*, 11(1), 421–439.

[6] Barger, S. R., Gauthier, N. C., & Krendel, M. (2020). Squeezing in a meal: myosin functions in phagocytosis. *Trends in cell biology*, 30(2), 157–167.

[7] Beach, J. R., Bruun, K. S., Shao, L., Li, D., Swider, Z., Remmert, K., Zhang, Y., Conti, M. A., Adelstein, R. S., Rusan, N. M., et al. (2017). Actin dynamics and competition for myosin

monomer govern the sequential amplification of myosin filaments. *Nature cell biology*, 19(2), 85–93.

[8] Bean, B. P. (2007). The action potential in mammalian central neurons. *Nature Reviews Neuroscience*, 8(6), 451–465.

[9] Bell, G. I. (1978). Models for the specific adhesion of cells to cells: a theoretical framework for adhesion mediated by reversible bonds between cell surface molecules. *Science*, 200(4342), 618–627.

[10] Bendix, P. M., Koenderink, G. H., Cuvelier, D., Dogic, Z., Koeleman, B. N., Brieher, W. M., Field, C. M., Mahadevan, L., & Weitz, D. A. (2008). A quantitative analysis of contractility in active cytoskeletal protein networks. *Biophysical journal*, 94(8), 3126–3136.

[11] Besser, A. & Schwarz, U. S. (2007). Coupling biochemistry and mechanics in cell adhesion: a model for inhomogeneous stress fiber contraction. *New Journal of Physics*, 9(11), 425.

[12] Bidone, T. C., Jung, W., Maruri, D., Borau, C., Kamm, R. D., & Kim, T. (2017). Morphological transformation and force generation of active cytoskeletal networks. *PLoS computational biology*, 13(1), e1005277.

[13] Blemker, S. S. (2017). Three-dimensional modeling of active muscle tissue: The why, the how, and the future. In *Biomechanics of living organs* (pp. 361–375). Elsevier.

[14] Brunello, E., Reconditi, M., Elangovan, R., Linari, M., Sun, Y.-B., Narayanan, T., Panine, P., Piazzesi, G., Irving, M., & Lombardi, V. (2007). Skeletal muscle resists stretch by rapid binding of the second motor domain of myosin to actin. *Proceedings of the National Academy of Sciences*, 104(50), 20114–20119.

[15] Burridge, K. & Wittchen, E. S. (2013). The tension mounts: stress fibers as force-generating mechanotransducers. *Journal of Cell Biology*, 200(1), 9–19.

[16] Cagigas, M. L., Bryce, N. S., Ariotti, N., Brayford, S., Gunning, P. W., & Hardeman, E. C. (2022). Correlative cryo-et identifies actin/tropomyosin filaments that mediate cell–substrate adhesion in cancer cells and mechanosensitivity of cell proliferation. *Nature materials*, 21(1), 120–128.

[17] Chandrasekaran, A., Upadhyaya, A., & Papoian, G. A. (2019). Remarkable structural transformations of actin bundles are driven by their initial polarity, motor activity, crosslinking, and filament treadmilling. *PLoS computational biology*, 15(7), e1007156.

[18] Chapin, L. M., Blankman, E., Smith, M. A., Shiu, Y.-T., & Beckerle, M. C. (2012). Lateral communication between stress fiber sarcomeres facilitates a local remodeling response. *Biophysical journal*, 103(10), 2082–2092.

[19] Cheffings, T. H., Burroughs, N. J., & Balasubramanian, M. K. (2016). Actomyosin ring formation and tension generation in eukaryotic cytokinesis. *Current Biology*, 26(15), R719–R737.

[20] Chin, D. & Means, A. R. (2000). Calmodulin: a prototypical calcium sensor. *Trends in cell biology*, 10(8), 322–328.

[21] Clift, R., Grace, J. R., & Weber, M. E. (2005). Bubbles, drops, and particles.

[22] Cortes, D. B., Gordon, M., Nédélec, F., & Maddox, A. S. (2020). Bond type and discretization of nonmuscle myosin ii are critical for simulated contractile dynamics. *Biophysical Journal*, 118(11), 2703–2717.

[23] Costa, K. D., Hucker, W. J., & Yin, F. C.-P. (2002). Buckling of actin stress fibers: a new wrinkle in the cytoskeletal tapestry. *Cell motility and the cytoskeleton*, 52(4), 266–274.

[24] Craig, R. & Megerman, J. (1977). Assembly of smooth muscle myosin into side-polar filaments. *The Journal of cell biology*, 75(3), 990–996.

[25] Dasbiswas, K., Hu, S., Schnorrer, F., Safran, S. A., & Bershadsky, A. D. (2018). Ordering of myosin ii filaments driven by mechanical forces: experiments and theory. *Philosophical Transactions of the Royal Society B: Biological Sciences*, 373(1747), 20170114.

[26] Deguchi, S., Matsui, T. S., & Sato, M. (2012). Simultaneous contraction and buckling of stress fibers in individual cells. *Journal of Cellular Biochemistry*, 113(3), 824–832.

[27] Deguchi, S., Ohashi, T., & Sato, M. (2006). Tensile properties of single stress fibers isolated from cultured vascular smooth muscle cells. *Journal of biomechanics*, 39(14), 2603–2610.

[28] Ding, S., Deguchi, S., & Kim, T. (2024). Unraveling a key molecular player governing pulmonary alveolar development.

[29] Dominguez, R. & Holmes, K. C. (2011). Actin structure and function. *Annual review of biophysics*, 40, 169–186.

[30] Eckels, E. C., Tapia-Rojo, R., Rivas-Pardo, J. A., & Fernández, J. M. (2018). The work of titin protein folding as a major driver in muscle contraction. *Annual review of physiology*, 80(1), 327–351.

[31] Eckenstaler, R., Hauke, M., & Benndorf, R. A. (2022). A current overview of rhoa, rhob, and rhoc functions in vascular biology and pathology. *Biochemical Pharmacology*, 206, 115321.

[32] Edman, K., Elzinga, G., & Noble, M. (1982). Residual force enhancement after stretch of contracting frog single muscle fibers. *The Journal of general physiology*, 80(5), 769–784.

[33] Eldemire, R., Tharp, C. A., Taylor, M. R., Sbaizero, O., & Mestroni, L. (2021). The sarcomeric spring protein titin: biophysical properties, molecular mechanisms, and genetic mutations associated with heart failure and cardiomyopathy. *Current cardiology reports*, 23, 1–9.

[34] Eliaz, Y., Nedelec, F., Morrison, G., Levine, H., & Cheung, M. S. (2020). Insights from graph theory on the morphologies of actomyosin networks with multilinkers. *Physical Review E*, 102(6), 062420.

[35] Erdmann, T., Albert, P. J., & Schwarz, U. S. (2013). Stochastic dynamics of small ensembles of non-processive molecular motors: The parallel cluster model. *The Journal of chemical physics*, 139(17).

[36] Erdmann, T. & Schwarz, U. S. (2012). Stochastic force generation by small ensembles of myosin ii motors. *Physical review letters*, 108(18), 188101.

[37] Ferrer, J. M., Lee, H., Chen, J., Pelz, B., Nakamura, F., Kamm, R. D., & Lang, M. J. (2008). Measuring molecular rupture forces between single actin filaments and actin-binding proteins. *Proceedings of the National Academy of Sciences*, 105(27), 9221–9226.

[38] Fill, M. & Copello, J. A. (2002). Ryanodine receptor calcium release channels. *Physiological reviews*, 82(4), 893–922.

[39] Fletcher, D. A. & Mullins, R. D. (2010). Cell mechanics and the cytoskeleton. *Nature*, 463(7280), 485–492.

[40] Freedman, S. L., Banerjee, S., Hocky, G. M., & Dinner, A. R. (2017). A versatile framework for simulating the dynamic mechanical structure of cytoskeletal networks. *Biophysical journal*, 113(2), 448–460.

[41] Frontera, W. R. & Ochala, J. (2015). Skeletal muscle: a brief review of structure and function. *Calcified tissue international*, 96, 183–195.

[42] Fujita, K., Ohmachi, M., Ikezaki, K., Yanagida, T., & Iwaki, M. (2019). Direct visualization of human myosin ii force generation using dna origami-based thick filaments. *Communications biology*, 2(1), 437.

[43] Fusi, L., Brunello, E., Reconditi, M., Piazzesi, G., & Lombardi, V. (2014). The non-linear elasticity of the muscle sarcomere and the compliance of myosin motors. *The Journal of physiology*, 592(5), 1109–1118.

[44] Galburt, E. A. & Tomko, E. J. (2017). Conformational selection and induced fit as a useful framework for molecular motor mechanisms. *Biophysical chemistry*, 223, 11–16.

[45] Galińska-Rakoczy, A., Engel, P., Xu, C., Jung, H., Craig, R., Tobacman, L. S., & Lehman, W. (2008). Structural basis for the regulation of muscle contraction by troponin and tropomyosin. *Journal of molecular biology*, 379(5), 929–935.

[46] Garrido-Casado, M., Asensio-Juárez, G., & Vicente-Manzanares, M. (2021). Nonmuscle myosin ii regulation directs its multiple roles in cell migration and division. *Annual review of cell and developmental biology*, 37(1), 285–310.

[47] Gateva, G., Kremneva, E., Reindl, T., Kotila, T., Kogan, K., Gressin, L., Gunning, P. W., Manstein, D. J., Michelot, A., & Lappalainen, P. (2017). Tropomyosin isoforms specify functionally distinct actin filament populations in vitro. *Current biology*, 27(5), 705–713.

[48] Goley, E. D. & Welch, M. D. (2006). The arp2/3 complex: an actin nucleator comes of age. *Nature reviews Molecular cell biology*, 7(10), 713–726.

[49] Gong, D., Yan, N., & Ledford, H. A. (2021). Structural basis for the modulation of ryanodine receptors. *Trends in Biochemical Sciences*, 46(6), 489–501.

[50] Gordon III, W. E. (1978). Immunofluorescent and ultrastructural studies of "sarcomeric" units in stress fibers of cultured non-muscle cells. *Experimental cell research*, 117(2), 253–260.

[51] Grewe, J. & Schwarz, U. S. (2020). Mechanosensitive self-assembly of myosin ii minifilaments. *Physical Review E*, 101(2), 022402.

[52] Hanson, J. (1955). The structural basis of contraction in striated muscle. In *Symp. Exp. Biol.*, volume 9 (pp. 228–264).

[53] Herrera, A. M., McParland, B. E., Bienkowska, A., Tait, R., Paré, P. D., & Seow, C. Y. (2005). Sarcomeres' of smooth muscle: functional characteristics and ultrastructural evidence. *Journal of cell science*, 118(11), 2381–2392.

[54] Herzog, W. (2017). Skeletal muscle mechanics: questions, problems and possible solutions. *Journal of neuroengineering and rehabilitation*, 14, 1–17.

[55] Hessel, A. L., Engels, N. M., Kuehn, M. N., Nissen, D., Sadler, R. L., Ma, W., Irving, T. C., Linke, W. A., & Harris, S. P. (2024). Myosin-binding protein c regulates the sarcomere lattice and stabilizes the off states of myosin heads. *Nature Communications*, 15(1), 2628.

[56] Hessel, A. L., Ma, W., Mazara, N., Rice, P. E., Nissen, D., Gong, H., Kuehn, M., Irving, T., & Linke, W. A. (2022). Titin force in muscle cells alters lattice order, thick and thin filament protein formation. *Proceedings of the National Academy of Sciences*, 119(48), e2209441119.

[57] Hill, A. V. (1938). The heat of shortening and the dynamic constants of muscle. *Proceedings of the Royal Society of London. Series B-Biological Sciences*, 126(843), 136–195.

[58] Hill, A. V. (1953). The mechanics of active muscle. *Proceedings of the Royal Society of London. Series B-Biological Sciences*, 141(902), 104–117.

[59] Hong, F., Haldeman, B. D., Jackson, D., Carter, M., Baker, J. E., & Cremo, C. R. (2011). Biochemistry of smooth muscle myosin light chain kinase. *Archives of biochemistry and biophysics*, 510(2), 135–146.

[60] Hotulainen, P. & Lappalainen, P. (2006). Stress fibers are generated by two distinct actin assembly mechanisms in motile cells. *The Journal of cell biology*, 173(3), 383–394.

[61] Hu, S., Dasbiswas, K., Guo, Z., Tee, Y.-H., Thiagarajan, V., Hersen, P., Chew, T.-L., Safran, S. A., Zaidel-Bar, R., & Bershadsky, A. D. (2017). Long-range self-organization of cytoskeletal myosin ii filament stacks. *Nature cell biology*, 19(2), 133–141.

[62] Huang, W., Matsui, T. S., Saito, T., Kuragano, M., Takahashi, M., Kawahara, T., Sato, M., & Deguchi, S. (2021). Mechanosensitive myosin ii but not cofilin primarily contributes to cyclic cell stretch-induced selective disassembly of actin stress fibers. *American Journal of Physiology-Cell Physiology*, 320(6), C1153–C1163.

[63] Huxley, A. F. (1957). Muscle structure and theories of contraction. *Progress in biophysics and biophysical chemistry*, 7, 255–318.

[64] Huxley, A. F. & Niedergerke, R. (1954). Structural changes in muscle during contraction: interference microscopy of living muscle fibres. *Nature*, 173(4412), 971–973.

[65] Huxley, H. (1953). Electron microscope studies of the organisation of the filaments in striated muscle. *Biochimica et biophysica acta*, 12(1-2), 387–394.

[66] Huxley, H. & Hanson, J. (1954). Changes in the cross-striations of muscle during contraction and stretch and their structural interpretation. *Nature*, 173(4412), 973–976.

[67] Hwang, W. & Karplus, M. (2019). Structural basis for power stroke vs. brownian ratchet mechanisms of motor proteins. *Proceedings of the National Academy of Sciences*, 116(40), 19777–19785.

[68] Isambert, H., Venier, P., Maggs, A. C., Fattoum, A., Kassab, R., Pantaloni, D., & Carlier, M.-F. (1995). Flexibility of actin filaments derived from thermal fluctuations: effect of bound nucleotide, phalloidin, and muscle regulatory proteins. *Journal of Biological Chemistry*, 270(19), 11437–11444.

[69] Ishikawa, Y. & Kurotani, R. (2008). Cardiac myosin light chain kinase: a new player in the regulation of myosin light chain in the heart.

[70] Johnston, K., Jinha, A., & Herzog, W. (2016). The role of sarcomere length non-uniformities in residual force enhancement of skeletal muscle myofibrils. *Royal Society Open Science*, 3(3), 150657.

[71] Josephs, R. & Harrington, W. F. (1966). Studies on the formation and physical chemical properties of synthetic myosin filaments. *Biochemistry*, 5(11), 3474–3487.

[72] Jülicher, F., Ajdari, A., & Prost, J. (1997). Modeling molecular motors. *Reviews of Modern Physics*, 69(4), 1269.

[73] Jung, W., Murrell, M. P., & Kim, T. (2015). F-actin cross-linking enhances the stability of force generation in disordered actomyosin networks. *Computational particle mechanics*, 2, 317–327.

[74] Kaminer, B. & Bell, A. L. (1966). Myosin filamentogenesis: effects of ph and ionic concentration. *Journal of molecular biology*, 20(2), 391–401.

[75] Karlin, A. (2002). Emerging structure of the nicotinic acetylcholine receptors. *Nature Reviews Neuroscience*, 3(2), 102–114.

[76] Kassianidou, E., Brand, C. A., Schwarz, U. S., & Kumar, S. (2017). Geometry and network connectivity govern the mechanics of stress fibers. *Proceedings of the National Academy of Sciences*, 114(10), 2622–2627.

[77] Katz, B. & Thesleff, S. (1957). A study of thedesensitization'produced by acetylcholine at the motor end-plate. *The Journal of physiology*, 138(1), 63.

[78] Kaunas, R. & Deguchi, S. (2011). Multiple roles for myosin ii in tensional homeostasis under mechanical loading. *Cellular and molecular bioengineering*, 4, 182–191.

[79] Kaunas, R., Nguyen, P., Usami, S., & Chien, S. (2005). Cooperative effects of rho and mechanical stretch on stress fiber organization. *Proceedings of the National Academy of Sciences*, 102(44), 15895–15900.

[80] Kee, Y.-S. & Robinson, D. N. (2008). Motor proteins: myosin mechanosensors. *Current Biology*, 18(18), R860–R862.

[81] Kilian, L. S., Voran, J., Frank, D., & Rangrez, A. Y. (2021). Rhoa: a dubious molecule in cardiac pathophysiology. *Journal of biomedical science*, 28(1), 33.

[82] Kim, T. (2015). Determinants of contractile forces generated in disorganized actomyosin bundles. *Biomechanics and modeling in mechanobiology*, 14, 345–355.

[83] Kim, T., Hwang, W., Lee, H., & Kamm, R. D. (2009). Computational analysis of viscoelastic properties of crosslinked actin networks. *PLoS computational biology*, 5(7), e1000439.

[84] Kim, Y.-E., Won, M., Lee, S.-G., Park, C., Song, C.-H., & Kim, K. K. (2019). Rbm47-regulated alternative splicing of tjp1 promotes actin stress fiber assembly during epithelial-to-mesenchymal transition. *Oncogene*, 38(38), 6521–6536.

[85] Kodera, N., Yamamoto, D., Ishikawa, R., & Ando, T. (2010). Video imaging of walking myosin v by high-speed atomic force microscopy. *Nature*, 468(7320), 72–76.

[86] Koenderink, G. H., Dogic, Z., Nakamura, F., Bendix, P. M., MacKintosh, F. C., Hartwig, J. H., Stossel, T. P., & Weitz, D. A. (2009). An active biopolymer network controlled by molecular motors. *Proceedings of the National Academy of Sciences*, 106(36), 15192–15197.

[87] Kokate, S. B., Ciuba, K., Tran, V. D., Kumari, R., Tojkander, S., Engel, U., Kogan, K., Kumar, S., & Lappalainen, P. (2022). Caldesmon controls stress fiber force-balance through dynamic cross-linking of myosin ii and actin-tropomyosin filaments. *Nature Communications*, 13(1), 6032.

[88] Kumar, S., Maxwell, I. Z., Heisterkamp, A., Polte, T. R., Lele, T. P., Salanga, M., Mazur, E., & Ingber, D. E. (2006). Viscoelastic retraction of single living stress fibers and its impact on cell shape, cytoskeletal organization, and extracellular matrix mechanics. *Biophysical journal*, 90(10), 3762–3773.

[89] Kuo, I. Y. & Ehrlich, B. E. (2015). Signaling in muscle contraction. *Cold Spring Harbor perspectives in biology*, 7(2), a006023.

[90] Lee, C.-F., Haase, C., Deguchi, S., & Kaunas, R. (2010). Cyclic stretch-induced stress fiber dynamics–dependence on strain rate, rho-kinase and mlck. *Biochemical and biophysical research communications*, 401(3), 344–349.

[91] Lee, J. Y., Chang, J. K., Dominguez, A. A., Lee, H.-p., Nam, S., Chang, J., Varma, S., Qi, L. S., West, R. B., & Chaudhuri, O. (2019). Yap-independent mechanotransduction drives breast cancer progression. *Nature communications*, 10(1), 1848.

[92] Lee, S., Kassianidou, E., & Kumar, S. (2018). Actomyosin stress fiber subtypes have unique viscoelastic properties and roles in tension generation. *Molecular biology of the cell*, 29(16), 1992–2004.

[93] Lehtimäki, J. I., Rajakylä, E. K., Tojkander, S., & Lappalainen, P. (2021). Generation of stress fibers through myosin-driven reorganization of the actin cortex. *Elife*, 10, e60710.

[94] Lenz, M. (2020). Reversal of contractility as a signature of self-organization in cytoskeletal bundles. *Elife*, 9, e51751.

[95] Lenz, M., Thoresen, T., Gardel, M. L., & Dinner, A. R. (2012). Contractile units in disordered actomyosin bundles arise from f-actin buckling. *Physical review letters*, 108(23), 238107.

[96] Li, J., Biel, T., Lomada, P., Yu, Q., & Kim, T. (2017). Buckling-induced f-actin fragmentation modulates the contraction of active cytoskeletal networks. *Soft Matter*, 13(17), 3213–3220.

[97] Lichtwark, G. & Wilson, A. (2007). Is achilles tendon compliance optimised for maximum muscle efficiency during locomotion? *Journal of biomechanics*, 40(8), 1768–1775.

[98] Lim, C., Zhou, E., & Quek, S. (2006). Mechanical models for living cells—a review. *Journal of biomechanics*, 39(2), 195–216.

[99] Lindstedt, S. & Nishikawa, K. (2017). Huxleys' missing filament: form and function of titin in vertebrate striated muscle. *Annual review of physiology*, 79(1), 145–166.

[100] Linke, W. A. (2023). Stretching the story of titin and muscle function. *Journal of biomechanics*, 152, 111553.

[101] Linsmeier, I., Banerjee, S., Oakes, P. W., Jung, W., Kim, T., & Murrell, M. P. (2016). Disordered actomyosin networks are sufficient to produce cooperative and telescopic contractility. *Nature communications*, 7(1), 12615.

[102] Liu, J. C.-Y., Rottler, J., Wang, L., Zhang, J., Pascoe, C. D., Lan, B., Norris, B. A., Herrera, A. M., Paré, P. D., & Seow, C. Y. (2013). Myosin filaments in smooth muscle cells do not have a constant length. *The Journal of physiology*, 591(23), 5867–5878.

[103] Liu, S., Matsui, T. S., Kang, N., & Deguchi, S. (2022). Analysis of senescence-responsive stress fiber proteome reveals reorganization of stress fibers mediated by elongation factor eef2 in hff-1 cells. *Molecular biology of the cell*, 33(1), ar10.

[104] Lo, H. S. & Xie, S. Q. (2012). Exoskeleton robots for upper-limb rehabilitation: State of the art and future prospects. *Medical engineering & physics*, 34(3), 261–268.

[105] Mai, J. K. & Paxinos, G. (2011). *The human nervous system*. Academic press.

[106] Mak, M., Zaman, M. H., Kamm, R. D., & Kim, T. (2016). Interplay of active processes modulates tension and drives phase transition in self-renewing, motor-driven cytoskeletal networks. *Nature communications*, 7(1), 10323.

[107] Malik-Garbi, M., Ierushalmi, N., Jansen, S., Abu-Shah, E., Goode, B. L., Mogilner, A., & Keren, K. (2019). Scaling behaviour in steady-state contracting actomyosin networks. *Nature physics*, 15(5), 509–516.

[108] Maninova, M., Caslavsky, J., & Vomastek, T. (2017). The assembly and function of perinuclear actin cap in migrating cells. *Protoplasma*, 254, 1207–1218.

[109] Maninová, M. & Vomastek, T. (2016). Dorsal stress fibers, transverse actin arcs, and perinuclear actin fibers form an interconnected network that induces nuclear movement in polarizing fibroblasts.

[110] Marcucci, L. & Yanagida, T. (2012). From single molecule fluctuations to muscle contraction: a brownian model of af huxley's hypotheses. *PLoS One*, 7(7), e40042.

[111] Marden, J. H. & Allen, L. R. (2002). Molecules, muscles, and machines: universal performance characteristics of motors. *Proceedings of the National Academy of Sciences*, 99(7), 4161–4166.

[112] Marko, J. F. & Siggia, E. D. (1995). Stretching dna. *Macromolecules*, 28(26), 8759–8770.

[113] Martin, T. G. & Kirk, J. A. (2020). Under construction: The dynamic assembly, maintenance, and degradation of the cardiac sarcomere. *Journal of Molecular and Cellular Cardiology*, 148, 89–102.

[114] Martins, B., Sorrentino, S., Chung, W.-L., Tatli, M., Medalia, O., & Eibauer, M. (2021). Unveiling the polarity of actin filaments by cryo-electron tomography. *Structure*, 29(5), 488–498.

[115] Maruyama, K. (1976). Connectin, an elastic protein from myofibrils. *The Journal of Biochemistry*, 80(2), 405–407.

[116] Massou, S., Nunes Vicente, F., Wetzel, F., Mehidi, A., Strehle, D., Leduc, C., Voituriez, R., Rossier, O., Nassoy, P., & Giannone, G. (2020). Cell stretching is amplified by active actin remodelling to deform and recruit proteins in mechanosensitive structures. *Nature cell biology*, 22(8), 1011–1023.

[117] Masters, T. A., Kendrick-Jones, J., & Buss, F. (2017). Myosins: domain organisation, motor properties, physiological roles and cellular functions. *The actin cytoskeleton*, (pp. 77–122).

[118] Matsui, T. S., Deguchi, S., Sakamoto, N., Ohashi, T., & Sato, M. (2009). A versatile micromechanical tester for actin stress fibers isolated from cells. *Biorheology*, 46(5), 401–415.

[119] Matsui, T. S., Sato, M., & Deguchi, S. (2013). High extensibility of stress fibers revealed by in vitro micromanipulation with fluorescence imaging. *Biochemical and biophysical research communications*, 434(3), 444–448.

[120] McGowan, S. E., Gilfanov, N., Chandurkar, M. K., Stiber, J. A., & Han, S. J. (2024). Drebrin is required for myosin-facilitated actin cytoskeletal remodeling during pulmonary alveolar development. *American journal of respiratory cell and molecular biology*, 70(4), 308–321.

[121] Mizuno, D., Tardin, C., Schmidt, C. F., & MacKintosh, F. C. (2007). Nonequilibrium mechanics of active cytoskeletal networks. *Science*, 315(5810), 370–373.

[122] Morgan, D. (1990). New insights into the behavior of muscle during active lengthening. *Biophysical journal*, 57(2), 209–221.

[123] Morgan, R. S. (1977). Actin rotates as myosin translates. *Journal of Theoretical Biology*, 67(4), 769–771.

[124] Morita, H., Seidman, J., Seidman, C. E., et al. (2005). Genetic causes of human heart failure. *The Journal of clinical investigation*, 115(3), 518–526.

[125] Murrell, M., Oakes, P. W., Lenz, M., & Gardel, M. L. (2015). Forcing cells into shape: the mechanics of actomyosin contractility. *Nature reviews Molecular cell biology*, 16(8), 486–498.

[126] Murrell, M. P. & Gardel, M. L. (2012). F-actin buckling coordinates contractility and severing in a biomimetic actomyosin cortex. *Proceedings of the National Academy of Sciences*, 109(51), 20820–20825.

[127] Niederman, R. & Pollard, T. D. (1975). Human platelet myosin. ii. in vitro assembly and structure of myosin filaments. *The Journal of cell biology*, 67(1), 72–92.

[128] Nishikawa, K. (2020). Titin: a tunable spring in active muscle. *Physiology*, 35(3), 209–217.

[129] Nishikawa, K. & Huck, T. G. (2021). Muscle as a tunable material: implications for achieving muscle-like function in robotic prosthetic devices. *Journal of Experimental Biology*, 224(19), jeb225086.

[130] Nishikawa, K. C., Monroy, J. A., Powers, K. L., Gilmore, L. A., Uyeno, T. A., & Lindstedt, S. L. (2013). A molecular basis for intrinsic muscle properties: implications for motor control. In *Progress in Motor Control: Neural, Computational and Dynamic Approaches* (pp. 111–125).: Springer.

[131] Nishikawa, K. C., Monroy, J. A., Uyeno, T. E., Yeo, S. H., Pai, D. K., & Lindstedt, S. L. (2012). Is titin a 'winding filament'? a new twist on muscle contraction. *Proceedings of the royal society B: Biological sciences*, 279(1730), 981–990.

[132] Oakes, P. W., Wagner, E., Brand, C. A., Probst, D., Linke, M., Schwarz, U. S., Glotzer, M., & Gardel, M. L. (2017). Optogenetic control of rhoa reveals zyxin-mediated elasticity of stress fibres. *Nature communications*, 8(1), 15817.

[133] Okamoto, T., Matsui, T. S., Ohishi, T., & Deguchi, S. (2020). Helical structure of actin stress fibers and its possible contribution to inducing their direction-selective disassembly upon cell shortening. *Biomechanics and Modeling in Mechanobiology*, 19, 543–555.

[134] Oshima, K., Sugimoto, Y., Irving, T. C., & Wakabayashi, K. (2012). Head-head interactions of resting myosin crossbridges in intact frog skeletal muscles, revealed by synchrotron x-ray fiber diffraction. *PLoS One*, 7(12), e52421.

[135] Pellegrin, S. & Mellor, H. (2007). Actin stress fibres. *Journal of cell science*, 120(20), 3491–3499.

[136] Pertici, I., Caremani, M., & Reconditi, M. (2019). A mechanical model of the half-sarcomere which includes the contribution of titin. *Journal of muscle research and cell motility*, 40, 29–41.

[137] Peterson, L. J., Rajfur, Z., Maddox, A. S., Freel, C. D., Chen, Y., Edlund, M., Otey, C., & Burridge, K. (2004). Simultaneous stretching and contraction of stress fibers in vivo. *Molecular biology of the cell*, 15(7), 3497–3508.

[138] Pirentis, A. P., Peruski, E., Iordan, A. L., & Stamenović, D. (2011). A model for stress fiber realignment caused by cytoskeletal fluidization during cyclic stretching. *Cellular and molecular bioengineering*, 4, 67–80.

[139] Pollard, T. D. (1982). Structure and polymerization of acanthamoeba myosin-ii filaments. *The Journal of cell biology*, 95(3), 816–825.

[140] Powers, J. D., Bianco, P., Pertici, I., Reconditi, M., Lombardi, V., & Piazzesi, G. (2020). Contracting striated muscle has a dynamic i-band spring with an undamped stiffness 100 times larger than the passive stiffness. *The Journal of Physiology*, 598(2), 331–345.

[141] Powers, J. D., Malingen, S. A., Regnier, M., & Daniel, T. L. (2021). The sliding filament theory since andrew huxley: multiscale and multidisciplinary muscle research. *Annual review of biophysics*, 50(1), 373–400.

[142] Powers, J. D., Williams, C. D., Regnier, M., & Daniel, T. L. (2018). A spatially explicit model shows how titin stiffness modulates muscle mechanics and energetics. *Integrative and comparative biology*, 58(2), 186–193.

[143] Rassier, D. E., Herzog, W., & Pollack, G. H. (2003). Stretch-induced force enhancement and stability of skeletal muscle myofibrils. In *Molecular and Cellular Aspects of Muscle Contraction* (pp. 501–515).: Springer.

[144] Reisler, E., Smith, C., & Seegan, G. (1980). Myosin minifilaments. *Journal of Molecular Biology*, 143(1), 129–145.

[145] Rode, C., Siebert, T., & Blickhan, R. (2009). Titin-induced force enhancement and force depression: a 'sticky-spring'mechanism in muscle contractions? *Journal of theoretical biology*, 259(2), 350–360.

[146] Ronceray, P., Broedersz, C. P., & Lenz, M. (2019). Fiber plucking by molecular motors yields large emergent contractility in stiff biopolymer networks. *Soft matter*, 15(7), 1481–1487.

[147] Saito, T., Huang, W., Matsui, T. S., Kuragano, M., Takahashi, M., & Deguchi, S. (2021). What factors determine the number of nonmuscle myosin ii in the sarcomeric unit of stress fibers? *Biomechanics and Modeling in Mechanobiology*, 20, 155–166.

[148] Sakamoto, Y., Buchanan, R. M., & Sacks, M. S. (2016). On intrinsic stress fiber contractile forces in semilunar heart valve interstitial cells using a continuum mixture model. *Journal of the mechanical behavior of biomedical materials*, 54, 244–258.

[149] Sakamoto, Y., Buchanan, R. M., Sanchez-Adams, J., Guilak, F., & Sacks, M. S. (2017). On the functional role of valve interstitial cell stress fibers: a continuum modeling approach. *Journal of biomechanical engineering*, 139(2), 021007.

[150] Saraswathibhatla, A. & Notbohm, J. (2020). Tractions and stress fibers control cell shape and rearrangements in collective cell migration. *Physical Review X*, 10(1), 011016.

[151] Sawma, T., Shaito, A., Najm, N., Sidani, M., Orekhov, A., El-Yazbi, A. F., Iratni, R., & Eid, A. H. (2022). Role of rhoa and rho-associated kinase in phenotypic switching of vascular smooth muscle cells: Implications for vascular function. *Atherosclerosis*, 358, 12–28.

[152] Schappacher-Tilp, G., Leonard, T., Desch, G., & Herzog, W. (2015). A novel three-filament model of force generation in eccentric contraction of skeletal muscles. *PloS one*, 10(3), e0117634.

[153] Scovil, C. Y. & Ronsky, J. L. (2006). Sensitivity of a hill-based muscle model to perturbations in model parameters. *Journal of biomechanics*, 39(11), 2055–2063.

[154] Selvaraj, M., Kokate, S. B., Reggiano, G., Kogan, K., Kotila, T., Kremneva, E., DiMaio, F., Lappalainen, P., & Huiskonen, J. T. (2023). Structural basis underlying specific biochemical activities of non-muscle tropomyosin isoforms. *Cell Reports*, 42(1).

[155] Sheetz, M. P. & Spudich, J. A. (1983). Movement of myosin-coated fluorescent beads on actin cables in vitro. *Nature*, 303(5912), 31–35.

[156] Skubiszak, L. & Kowalczyk, L. (2002). Myosin molecule packing within the vertebrate skeletal muscle thick filaments. a complete bipolar model. *Acta Biochimica Polonica*, 49(4), 829–840.

[157] Soares e Silva, M., Depken, M., Stuhrmann, B., Korsten, M., MacKintosh, F. C., & Koenderink, G. H. (2011). Active multistage coarsening of actin networks driven by myosin motors. *Proceedings of the National Academy of Sciences*, 108(23), 9408–9413.

[158] Squarci, C., Bianco, P., Reconditi, M., Pertici, I., Caremani, M., Narayanan, T., Horváth, Á. I., Málnási-Csizmadia, A., Linari, M., Lombardi, V., et al. (2023). Titin activates myosin filaments in skeletal muscle by switching from an extensible spring to a mechanical rectifier. *Proceedings of the National Academy of Sciences*, 120(9), e2219346120.

[159] Squire, J. M. (1997). Architecture and function in the muscle sarcomere. *Current opinion in structural biology*, 7(2), 247–257.

[160] Stachowiak, M. R., McCall, P. M., Thoresen, T., Balcioglu, H. E., Kasiewicz, L., Gardel, M. L., & O'Shaughnessy, B. (2012). Self-organization of myosin ii in reconstituted actomyosin bundles. *Biophysical journal*, 103(6), 1265–1274.

[161] Stam, S., Alberts, J., Gardel, M. L., & Munro, E. (2015). Isoforms confer characteristic force generation and mechanosensation by myosin ii filaments. *Biophysical journal*, 108(8), 1997–2006.

[162] Sun, J., Qiao, Y.-N., Tao, T., Zhao, W., Wei, L.-S., Li, Y.-Q., Wang, W., Wang, Y., Zhou, Y.-W., Zheng, Y.-Y., et al. (2020). Distinct roles of smooth muscle and non-muscle myosin light chain-mediated smooth muscle contraction. *Frontiers in Physiology*, 11, 593966.

[163] Sweeney, H. L. & Houdusse, A. (2010). Structural and functional insights into the myosin motor mechanism. *Annual review of biophysics*, 39, 539–557.

[164] Tahir, U., Hessel, A. L., Lockwood, E. R., Tester, J. T., Han, Z., Rivera, D. J., Covey, K. L., Huck, T. G., Rice, N. A., & Nishikawa, K. C. (2018). Case study: a bio-inspired control algorithm for a robotic foot-ankle prosthesis provides adaptive control of level walking and stair ascent. *Frontiers in Robotics and AI*, 5, 36.

[165] Tanner, K., Boudreau, A., Bissell, M. J., & Kumar, S. (2010). Dissecting regional variations in stress fiber mechanics in living cells with laser nanosurgery. *Biophysical journal*, 99(9), 2775–2783.

[166] Thomas, W. E., Vogel, V., & Sokurenko, E. (2008). Biophysics of catch bonds. *Annu. Rev. Biophys.*, 37, 399–416.

[167] Thoresen, T., Lenz, M., & Gardel, M. L. (2013). Thick filament length and isoform composition determine self-organized contractile units in actomyosin bundles. *Biophysical journal*, 104(3), 655–665.

[168] Tojkander, S., Gateva, G., & Lappalainen, P. (2012). Actin stress fibers–assembly, dynamics and biological roles. *Journal of cell science*, 125(8), 1855–1864.

[169] Tojkander, S., Gateva, G., Schevzov, G., Hotulainen, P., Naumanen, P., Martin, C., Gunning, P. W., & Lappalainen, P. (2011). A molecular pathway for myosin ii recruitment to stress fibers. *Current Biology*, 21(7), 539–550.

[170] Totsukawa, G., Wu, Y., Sasaki, Y., Hartshorne, D. J., Yamakita, Y., Yamashiro, S., & Matsumura, F. (2004). Distinct roles of mlck and rock in the regulation of membrane protrusions and focal adhesion dynamics during cell migration of fibroblasts. *The Journal of cell biology*, 164(3), 427–439.

[171] Trombitás, K. & Tigyi-Sebes, A. (1984). Cross-bridge interaction, with oppositely polarized actin filaments in double-overlap zones of insect flight muscle. *Nature*, 309(5964), 168–170.

[172] Tskhovrebova, L. & Trinick, J. (2003). Titin: properties and family relationships. *Nature reviews Molecular cell biology*, 4(9), 679–689.

[173] Tyska, M., Dupuis, D., Guilford, W., Patlak, J., Waller, G., Trybus, K., Warshaw, D., & Lowey, S. (1999). Two heads of myosin are better than one for generating force and motion. *Proceedings of the National Academy of Sciences*, 96(8), 4402–4407.

[174] Underhill, P. T. & Doyle, P. S. (2004). On the coarse-graining of polymers into bead-spring chains. *Journal of non-newtonian fluid mechanics*, 122(1-3), 3–31.

[175] Vilfan, A. & Duke, T. (2003). Instabilities in the transient response of muscle. *Biophysical Journal*, 85(2), 818–827.

[176] Von der Ecken, J., Müller, M., Lehman, W., Manstein, D. J., Penczek, P. A., & Raunser, S. (2015). Structure of the f-actin–tropomyosin complex. *Nature*, 519(7541), 114–117.

[177] Wagoner, J. A. & Dill, K. A. (2016). Molecular motors: Power strokes outperform brownian ratchets. *The Journal of Physical Chemistry B*, 120(26), 6327–6336.

[178] Walcott, S., Warshaw, D. M., & Debold, E. P. (2012). Mechanical coupling between myosin molecules causes differences between ensemble and single-molecule measurements. *Biophysical journal*, 103(3), 501–510.

[179] Wang, H. & Oster, G. (2002). Ratchets, power strokes, and molecular motors. *Applied Physics A*, 75, 315–323.

[180] Wang, J. H.-C., Goldschmidt-Clermont, P., & Yin, F. C.-P. (2000). Contractility affects stress fiber remodeling and reorientation of endothelial cells subjected to cyclic mechanical stretching. *Annals of biomedical engineering*, 28, 1165–1171.

[181] Wang, L., Tsang, H. Y., Yan, Z., Tojkander, S., Ciuba, K., Kogan, K., Liu, X., & Zhao, H. (2023). Luzp1 regulates the assembly of stress fibers by promoting maturation of contractile actomyosin bundles. *bioRxiv*, (pp. 2023–09).

[182] Wang, Z., Grange, M., Wagner, T., Kho, A. L., Gautel, M., & Raunser, S. (2021). The molecular basis for sarcomere organization in vertebrate skeletal muscle. *Cell*, 184(8), 2135–2150.

[183] Weirich, K. L., Stam, S., Munro, E., & Gardel, M. L. (2021). Actin bundle architecture and mechanics regulate myosin ii force generation. *Biophysical Journal*, 120(10), 1957–1970.

[184] Weißenbruch, K., Grewe, J., Hippler, M., Fladung, M., Tremmel, M., Stricker, K., Schwarz, U. S., & Bastmeyer, M. (2021). Distinct roles of nonmuscle myosin ii isoforms for establishing tension and elasticity during cell morphodynamics. *Elife*, 10, e71888.

[185] Williams, C. D., Regnier, M., & Daniel, T. L. (2010). Axial and radial forces of cross-bridges depend on lattice spacing. *PLoS computational biology*, 6(12), e1001018.

[186] Williams, C. D., Regnier, M., & Daniel, T. L. (2012). Elastic energy storage and radial forces in the myofilament lattice depend on sarcomere length. *PLoS computational biology*, 8(11), e1002770.

[187] Williams, C. D., Salcedo, M. K., Irving, T. C., Regnier, M., & Daniel, T. L. (2013). The length–tension curve in muscle depends on lattice spacing. *Proceedings of the Royal Society B: Biological Sciences*, 280(1766), 20130697.

[188] Winters, J. M. (1990). Hill-based muscle models: a systems engineering perspective. In *Multiple muscle systems: biomechanics and movement organization* (pp. 69–93). Springer.

[189] Woll, K. A. & Van Petegem, F. (2022). Calcium-release channels: structure and function of ip3 receptors and ryanodine receptors. *Physiological Reviews*, 102(1), 209–268.

[190] Xie, P. (2020). Dynamics of atp-dependent and atp-independent steppings of myosin-v on actin: catch-bond characteristics. *Journal of the Royal Society Interface*, 17(165), 20200029.

[191] Yamamoto, K., Miura, H., Ishida, M., Mii, Y., Kinoshita, N., Takada, S., Ueno, N., Sawai, S., Kondo, Y., & Aoki, K. (2021). Optogenetic relaxation of actomyosin contractility uncovers mechanistic roles of cortical tension during cytokinesis. *Nature communications*, 12(1), 7145.

[192] Yoshigi, M., Hoffman, L. M., Jensen, C. C., Yost, H. J., & Beckerle, M. C. (2005). Mechanical force mobilizes zyxin from focal adhesions to actin filaments and regulates cytoskeletal reinforcement. *The Journal of cell biology*, 171(2), 209–215.

[193] Yu, Q., Li, J., Murrell, M. P., & Kim, T. (2018). Balance between force generation and relaxation leads to pulsed contraction of actomyosin networks. *Biophysical journal*, 115(10), 2003–2013.

[194] Zhao, Y., Ding, S., & Todoh, M. (2022). Validate the force-velocity relation of the hill's muscle model from a molecular perspective. *Frontiers in Bioengineering and Biotechnology*, 10, 1006571.